國 立 交 通 大 學

土 木 工 程 研 究 所
博 士 論 文

利用空載，地面重力與測高資料計算台灣大地起伏: 研究向上/向下延續與地形效應計算

Modeling Taiwan Geoid Using Airborne, Surface Gravity and Altimetry Data: Investigations of Downward/Upward Continuations and Terrain Modeling Techniques

研究生：蕭宇伸

指導教授：黃金維

中華民國九十六年六月

利用空載，地面重力與測高資料計算台灣大地起伏: 研究向上/向下延續與地形效應計算

Modeling Taiwan Geoid Using Airborne, Surface Gravity and Altimetry Data: Investigations of Downward/Upward Continuations and Terrain Modeling Techniques

研究生：蕭宇伸   Student: Yu-Shen Hsiao

指導教授：黃金維   Advisor: Cheinway Hwang

國立交通大學

土木工程研究所

博士論文

A Thesis

Submitted to Department of Civil Engineering

College of Engineering

National Chiao Tung University

in partial Fulfillment of the Requirements

for the Degree of Doctor

in

Civil Engineering

June 2007

Hsinchu, Taiwan, Republic of China

利用空載，地面重力與測高資料計算台灣大地起伏：研究向上/向下延續與地形效應計算

研究生：蕭宇伸　　　　　　　　　　　　　　指導教授：黃金維

國立交通大學土木工程研究所

摘要

　　本論文的內容是結合地面、船載、測高與空載重力資料計算台灣與周邊海域的大地起伏模型。空載重力資料是在平均高度5156公尺下利用LaCoste and Romberg (LCR) System II 空載/船載重力儀所測得。為了得到最佳的大地起伏模型，本文研究兩個主要的課題。第一，考慮三種計算剩餘地形效應的方法，這三種方法分別為快速傅立葉轉換、柱狀體法與高斯求積法。在柱狀體法中，將考慮二維地質密度模型的影響。第二，快速傅立葉轉換與最小二乘配置法應用於向下延續的計算。在快速傅立葉轉換計算時，高斯與維納濾波將用平滑向下延續的重力值。最小二乘配置法則分為直接與間接大地起伏計算方法。此外，本文大地起伏計算策略為去除回覆法並搭配最小二乘配置法。

　　空中重力異常與地表重力比較後發現，兩者間較大的差值分部於高山地區，其主要原因為此區域缺乏地面重力資料。在交叉點分析方面，在bias-only改正前後的交叉點差值的均方根分別為4.92 和 2.88 mgal。在重複分析比較方面，150秒的濾波寬度是平滑空載重力值的最佳濾波寬度。在剩餘地形效應的研究方面，用快速傅立葉轉換計算此效應的大地起伏模型具有最佳的精度。此外，雖然考慮地質密度變化後，大地起伏面會比僅考慮地質密度常數的大地起伏模型有著4公分的變化量，但對改善大地起伏精度卻非常有限。在向下延續分析方面，先把重力向下延續到海水面(包括利用高斯與維納濾波的快速傅立葉轉換與最小二乘配置法)，再計算大地起伏的方法，所表現出的大地起伏模型很相似。然而採用最小二乘配置法直接計算大地起伏所得到的模型與其他方法所計算的比較,在某些區域有著30公分的差值。大致上來說，結合地面與空載重力所計算得到的大地起

伏，其精度要比僅用地面重力所計算得的要佳，在部分山區可達到10公分以內的精度。

Modeling Taiwan Geoid Using Airborne, Surface Gravity and Altimetry Data: Investigations of Downward/Upward Continuations and Terrain Modeling Techniques

Student: Yu-Shen Hsiao   Advisor: Cheinway Hwang

Department of Civil Engineering
National Chiao Tung University

Abstract

This dissertation is aimed at geoid modeling over Taiwan and the surrounding seas by land-based, shipborne, altimeter, and airborne gravity data. Airborne gravity data was obtained from an airborne gravity survey over Taiwan using a LaCoste and Romberg (LCR) System II air-sea gravimeter at an average altitude of 5156 m. In order to model the best geoid, two main topics are studied. First, three computational methods of the residual terrain model (RTM) effects are considered. The three methods are the fast Fourier transform (FFT), prism, and Gaussian quadrature methods. A 2-D density model of terrain is used in the prism method. Second, the FFT and least squares collocation (LSC) methods are adopted for the computation of the downward continuation (DWC). Both Gaussian and Wiener low-pass filters are used to smooth the downward-continued data by using FFT. Direct and indirect geoid computations are studied in LSC DWC. The methodology of the geoid modeling is mainly based on the remove-compute-restore (RCR) procedure by using LSC.

The airborne gravity anomalies are compared with the surface values. Large discrepancies are found to occur over high mountains due to the sparse surface gravity data coverage. The RMS crossover differences before and after a bias-only adjustment are 4.92 and 2.88 mgal. A filter width of 150 s is the optimal width for filtering the airborne gravity data, according to a repeatability analysis. In the investigation of the RTM, the FFT method in the RTM-derived effect computation produces the best geoid accuracy. Although the density variation considered in the geoid modeling yields a 4-cm change in the geoid surface from that using a geological constant, the

improvement in the geoid accuracy is extremely small. In the DWC analysis, the methods of DWC to sea level, including FFT with the Gaussian and Wiener filters and LSC, perform similar in geoid modeling. The method of direct geoid determination by LSC provides an obviously different geoid result due to the 30-cm differences of geoid surface from the other geoid models over some areas. Generally, the accuracies of the geoid models from the surface and airborne gravity data outperform the surface-gravity-only geoid models. The improvement in geoid accuracy reaches 10 cm over some high mountainous areas.

Table of Contents

List of Tables

List of Figures

Chapter 1

Introduction

1.1 Background

Taiwan experiences a large amount of seismic activity because it is located over the junction of the Eurasia plate and the Philippine Sea plate. The uplift and subsidence of land are created due to the collision of these two plates. Most areas of Taiwan Island are subjected to northwest-southeast compression at an average rate of 8.2 cm/year (Yu et al., 1997). The subduction of the Philippine Sea plate into the Eurasia plate creates a deep trench and large negative gravity anomalies to the east of Taiwan. On the other hand, it also creates the Central Range with a high terrain and huge positive gravity anomalies on land. The maximum altitude is at the Central Range, reaching 3952 m, which corresponds to the highest peak in East Asia. In eastern Taiwan and the surrounding sea, the mountains and the seabed, which are only several km away from the coast, reach heights of approximately 2000 m and –5000 m, respectively. Due to the extremely rough terrain and bathymetry (Fig 1-1), geoid modeling over Taiwan Island and its surrounding marine areas is quite a challenge for geodesists and geophysicists.

Geoid determination with high accuracy is a primary goal for geoscientists. The importance of the geoid for geodesists is that it is a reference surface for orthometric heights. Once a reference surface is established, orthometric heights referred to the local vertical datum are obtained. In addition, it is feasible to determine the orthometric heights by using GPS. A high accuracy geoid is the key factor for obtaining orthometric heights without leveling. If we have a high quality geoid model, orthometric heights can be efficiently and economically computed using GPS-derived ellipsoidal heights. For oceanographers, the geoid is useful for the investigation of currents, tides, and sea surface topography. For geophysicists, the geoid can be used to understand the characteristics of the earth's interior sources. Besides geodetic purposes, the geoid is also applied in mapping, photogrammetry, and remote sensing. This is why most countries around the world are making efforts to compute their own precise geoid models.

The estimation of the topographic effect is important for geoid determination, especially over mountainous areas. This estimation can be used to calculate the effects

of high frequency on gravity and the geoid; these cannot be calculated using the geopotential model and local gravity data. In most investigations related to the topographic effect, it is assumed that the density of the topographic mass is constant. However, several studies in recent years have taken into consideration the influence of the density variation of the topographic mass. In addition, the chosen method and digital elevation models (DEM) used in topographic effect computations also need to be focused upon in order to obtain a more precise result in an efficient manner.

Airborne gravimetry is a method to determine the gravity field by measurements from an aircraft. Based on this method's feature, airborne gravity data are valuable for areas with sparse gravity data, such as high mountains where data are always collected along the roads in valleys. Airborne gravity data are also useful for coastal regions wherein the gravity data coverage, especially over shallow water areas, obtained from satellite altimetry and land gravimetry data is of poor quality. Therefore, airborne gravimetry is suitable for Taiwan Island where over 75% of the terrain comprises hills and high mountains and 70% of the coast is near shallow water areas. Poor gravity data coverage results in poor accuracy of geoid modeling. Airborne gravity surveys with equally spaced tracks can make data coverage denser and bring improvements in the geoid computation.

Another interesting topic in the recent years has been how to combine different kinds of gravity data to compute a precise geoid. These data include terrestrial, shipborne, airborne, and altimeter-derived gravity. The combination of different types of gravity measurements is a challenging task for geodesists due to their different resolutions and characteristics. Airborne gravity data have an unusual property in that the gravity field level is different from that of other types of data. Thus, the technique of downward continuation (DWC) is important for airborne data to press aerial gravity field to the level which we are interested in.

The objective of this thesis is to determine the most accurate geoid over Taiwan and its surrounding sea area by the use of surface, altimeter-derived and airborne gravity. Based on this objective, there are several main issues to be investigated in this dissertation: (1) Which is the best method for topographic effect computation? (2) Is the consideration of the density variation of the topographic mass necessary in topographic effect computation? Can it be ignored? (3) What is the quality of the airborne gravity data used in the geoid modeling over Taiwan? (4) What is the best DWC method that can be applied to airborne data? (5) What is the ideal geoid model

by combining all types of gravity data? All these topics are important and have been investigated in this geoid modeling study. In brief, this dissertation focuses on how to obtain the most accurate geoid over Taiwan by selecting the best (1) topographic effect computation method, (2) DWC technique, and (3) geoid determination method.

1.2 Literature Review

Geoid determination has been of interest to geodesists for more than a century. Basically, two types of methods are usually used for local geoid determination—Stokes integration and least-squares collocation (LSC). They are deterministic and stochastical methods, respectively. Stokes integration can be performed very quickly using the fast Fourier transform (FFT) on gridded data. On the contrary, LSC requires a larger computational effort. Stokes integration generally only uses one data type with uniform noise. However, LSC can accept hybrid data with individual noises. Stokes integration is usually used for the continental areas and geoid models over several regions around the world (e.g., Boziane, 1996; Denker et al., 1997; Forsberg et al., 1996; Smith and Milbert, 1999; Sideris, 1995). The application of LSC in physical geodesy has been discussed in detail by Moritz (1980). The first centimeter geoid was computed for an area around Hannover in Germany in 1987 (Denker and Wenzel, 1987) by LSC. This method was subsequently used in many countries and was met with success (e.g., Sevilla, 1997; Hwang, 1997; Tscherning et al., 2001). Compared to Stokes integration, LSC gives error estimates and error covariances that reflect the data distribution and quality. For modeling the local gravity and geoid field at present, the LSC method has been proven to be a powerful technique.

Geoid modeling using Remove-Compute-Restore (RCR) procedure by Stokes integration over Taiwan was first investigated by Tsuei (1995). In subsequent years, a number of studies based on RCR procedure by LSC were carried out, e.g. Hwang (1997, 2001, 2003, 2005), Hwang et al. (2006a, 2006b, 2007b). Most of these results show a geoid accuracy of several centimeters over the west plain but of 1~2 decimeters over high mountains.

The topographic effect in geoid determination has also been studied for many years, especially in rough terrains. The relevant investigations can be divided into two main parts: (1) the effects of the residual terrain model (RTM) and (2) Helmert's

3

second method of condensation. There are several methodologies to determine the topographic effect. An earlier research containing the complete computation of this effect can be found in Forsberg (1984). It presented the FFT and prism methods to calculate the RTM-derived effect. Sjoberg (2000) used Helmert's second method of condensation to reduce the topography. Omang and Forsberg (2000) investigated three different methods of dealing with topography in geoid modeling: the isostatic, Helmert condensation, and RTM methods. Other studies about the topographic effect in geoid modeling include Forsberg (1985), Nahavandchi and Sjoberg (2001), and Flury (2006). Furthermore, we usually assume that the density of the topographic mass is constant (2.67 g/cm^3) while computing the topographic effect, but recently, several investigations have been performed to study the impact of more realistic density variations of the topographic masses. Martinec (1998) showed that the geoid can be changed approximately to the decimeter level by considering the lateral density variation of the topographical masses. Pagiatakis et al. (1998) reported that the effect of lateral density variations on the geoid can reach nearly 10 cm in the Skeena region in Canada, where the terrain is hilly. Huang (2002) showed that the total density variation effect on the geoid heights ranges from –7.0 cm to 2.8 cm in the Canadian Rocky Mountains. It is evident that the use of the digital topographical density model will significantly improve the accuracy of the geoid. Other studies about density variations can be found in Huang et al. (2001), Hunegnaw (2001), Smith (2002), Kuhn (2003), and Sjoberg (2004).

Airborne gravity surveys have been performed for over forty years, but geodesists have been paying more attention to them recently due to the advancement of the methodology, improvement in instrumentation, and development of the precise kinematic GPS in the past decade. Due to the recent and rapid development of these techniques, 1~2 mgal and half wavelengths of 3–4 km can be achieved by airborne gravity surveys (Schwarz and Li, 1997). The first test of the airborne gravity survey was made by Thompson and LaCoste (1960). The main objective of this flight is to show that gravity measurement from a flying aircraft is feasible. The first large-scale airborne gravity experiment was performed over Greenland (Brozena, 1992). In addition, several airborne gravity surveys have also been performed in places whose terrains are similar to that of Taiwan, such as the Rocky Mountains, the Alps, and Malaysia.

Airborne gravimetry tests are often conducted in the Rocky Mountains due to the

complex topography. In 1995, an airborne gravity survey (Wei and Schwarz, 1998) was carried out over the Rocky Mountains. The gravity system includes an inertial navigation system (INS) and two GPS receivers on the aircraft. The survey lines contain four flights with the same trajectory, which has an east-west profile of 250 km. The flying altitude and speed were 5.5 km and 430 km/h, respectively. The gravity result shows that the repeatability standard deviation is about 2 mgal with a filter length of 120 s and about 3 mgal with a filter length of 90 s. The standard deviation of the difference between the airborne gravity and upward continued ground gravity is about 3 mgal for both filter lengths. In the next year, another airborne gravity survey was conducted in the Rocky Mountains again (Glennie and Schwarz, 1999). The mission was carried out over a single $100 \times 100 \text{ km}^2$ area with a line spacing of 10 km. The analyses of the crossover differences showed a root mean square (RMS) agreement at the level of 1.6 mgal.

In 1998, an airborne gravity survey was carried out over the Alps (Verdun et al., 2003). The mission consisted of 18 NS and 16 EW survey lines with a line spacing of 10 and 20 km, respectively. The gravimeter, which is a LaCoste & Romberg relative air/sea gravimeter (type SA), was mounted in a DeHavilland Twin Otter aircraft flying at a constant altitude of 5100 m and a mean ground speed of about 280 km/hr. Seven ground based GPS reference stations were used to determine the positions of the aircraft. The accuracies of the Bouguer anomaly are determined from the crossover analysis (15.34 mgal RMS before adjustment and line selection) and the ground upward continuation (UWC) (7.68 mgal RMS for a spatial resolution of 8 km).

Airborne gravimetry in Malaysia was carried out by National Land Survey and Cadastre (KMS) of Denmark. The airborne gravity survey over the entire peninsula and Brunei was conducted with a 5 km line spacing, using an An-38 aircraft. More than 600 hours were flown with LaCoste and Romberg gravimeters (models S-93 and S-99) to collect the basic airborne gravity data at a flight speed of 150–250 km/hr and an aircraft altitude of less than 4500 m, which typically corresponds to a height of 300–1000 m above the topography, depending on the weather conditions. The resulting gravity anomalies of the crossover analysis were higher than 2 mgal RMS.

Airborne gravity surveys are still conducted in many countries and regions. These areas include North Carolina (Brozena and Peters, 1988), Skagerrak (Kearsley et al., 1998), Azores Islands (Bastos et al., 1998), Antarctica (Bell et al., 1999), the

Nordic/Baltic area (Forsberg and Solheim, 2000), Greenland/Svalbard (Forsberg et al., 2003a), the Arctic sea (Childers et al., 2001 and Forsberg et al., 2003b), Lincoln Sea and Wandel Sea (Olesen et al., 2003), Baltic Sea, the Great Barrier Reef, Crete Island, and Mongolia. These missions yielded an average RMS error of 2 mgal based on the crossover comparisons and an average interior geoid accuracy of 5 cm based on reliable GPS/leveling data.

The precision of geoid modeling has improved in recent years due to the development of airborne gravimetry. Forsberg et al. (2000) showed that the routine accuracy of airborne gravimetry is at the 2 mgal level, which may translate into a geoid accuracy of 5–10 cm on a regional scale. Kearsley et al. (1998) indicated that the gravity field determined from an aircraft with flight separations of 5 to 10 km can be used to evaluate precise (2 cm) relative geoid heights over north Jutland. Schwarz and Li (1996) pointed out that a centimeter geoid can be obtained if the minimum wavelength resolved is about 14 km in flat areas and 5 km in mountainous areas. In the airborne gravimetry in Malaysia as mentioned above, the data contributed to a geoid accuracy of smaller than 5 cm. Combining the different types of gravity data for geoid determination is also an interesting topic. Novak et al. (2003) reported that the first geoid model computed using the combination of airborne and global gravity data had a difference standard deviation of 5.5 cm; this is comparable to the reference geoid computed only from the ground gravity data. The second geoid model, based on the combination of the airborne and ground gravity data, had a difference standard deviation of 4.7 cm by comparison of the same reference geoid. Jekeli and Kwon (2002), and Serpas and Jekeli (2005), used the horizontal components of airborne gravity observations and also reported a sub-decimeter precision in the determination of the relative local geoid. Other research about geoid determination using airborne gravity data include, among others, Kern et al. (2003), Novak (2003), Olesen (2003), Li (2000), Serpas (2003), Bayoud and Sideris (2003), and Olesen et al. (2002).

1.3 Outline of Thesis

In chapter 2, the main principles of geoid modeling, including the spherical harmonic function, Stokes integration, and LSC, are presented. In addition, the RCR procedure and the theorem of UWC and DWC are also described.

All data except the airborne gravity data used in geoid modeling are introduced

in chapter 3. These data include the surface gravity, altimetry data, global geopotential model (GGM), DEM, density model, and GPS/leveling points for evaluating the geoid accuracy.

Geoid modeling results using three RTM-derived effects methods are presented in chapter 4. The three methods are FFT, prism and Gaussian quadrature. Besides, the influence of the density variation of the topographic mass on the geoid is also discussed.

In chapter 5, a description of the airborne gravimetry theorem and an airborne gravity survey over Taiwan are presented. Furthermore, three methods to evaluate the accuracy of airborne gravity data are mentioned.

In chapter 6, the application of airborne gravity data is discussed. The data are processed by the DWC technique and are used for the geoid computation. A comparison between the downward-continued airborne gravity data by the FFT and LSC is analyzed and described. Two low-pass filters used in the frequency domain and two types of geoid modeling by the LSC DWC are also investigated.

A summary, conclusions, future research, and suggestions are presented in the final chapter.
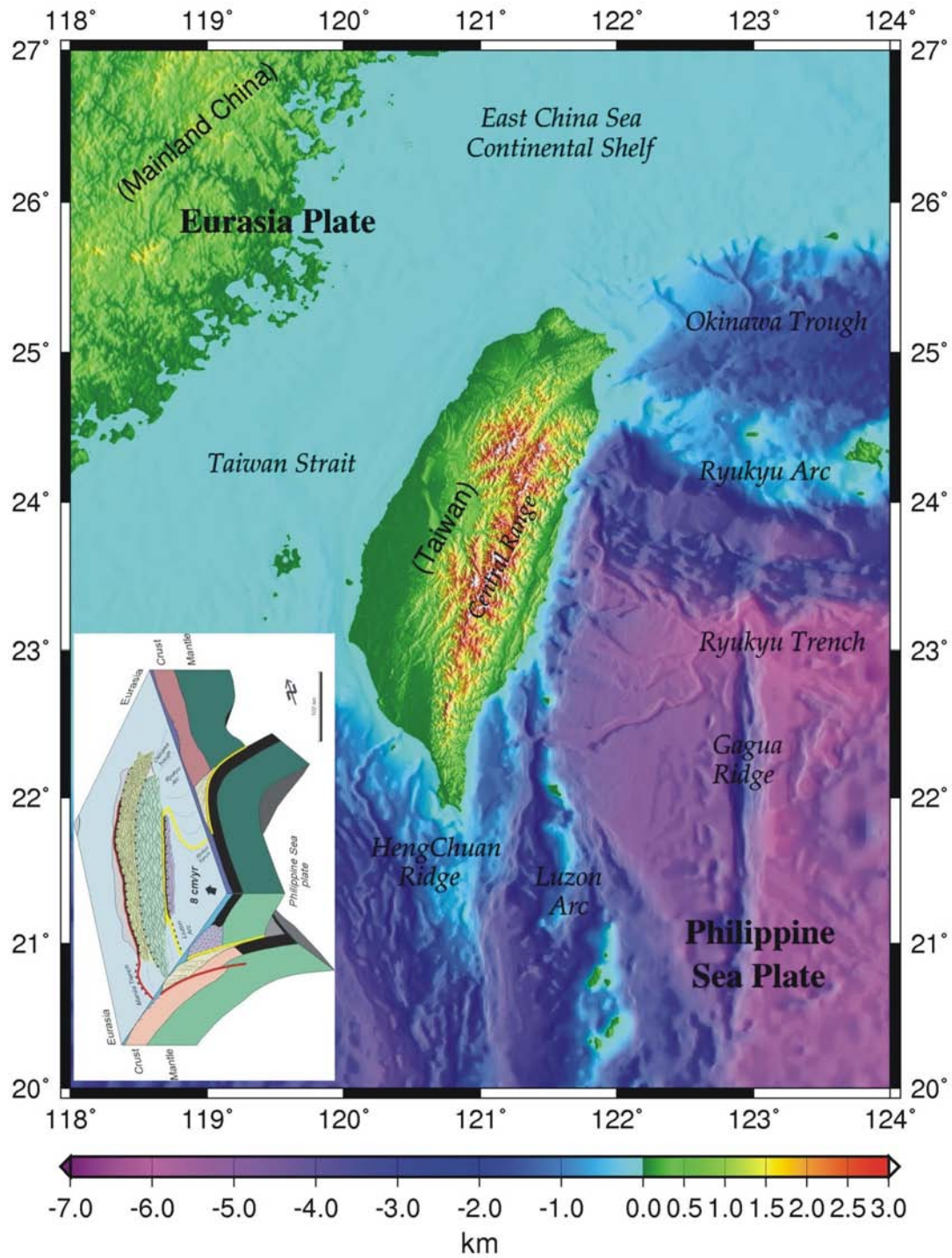
Fig. 1-1 Terrain and bathymetry around Taiwan (Hwang et al., 2007b). The inset is a tectonic map of Taiwan from Angelier et al. (1997). The Philippine Sea plate moves towards the Eurasia plate at a speed of 8.2 cm/year.

Chapter 2

Principles of Geoid Determination and Upward/Downward Continuations

2.1 Introduction

The strategy of geoid modeling used in this study is based on the remove-compute-restore (RCR) procedure, which is useful for high-resolution local gravity or geoid determinations. Geoid modeling takes into account information regarding three parts of the gravity field, namely, the long-, intermediate-, and short-wavelength parts. In this study, the long-wavelength part is determined from the global geopotential model by using a spherical harmonic function; the intermediate-wavelength part, from local gravity observations by using least squares collocation (LSC); and the short-wavelength part, from the high-resolution digital terrain model.

Upward/downward continuation (UW/DWC) is a method that can be used to transform the gravity potential on a surface into that on a higher/lower surface (Blakely, 1995). In other words, UWC and DWC are performed in order to obtain gravity functional from one level surface to another. It is important to apply both continuations to airborne gravity data in order to calculate the geoid by using gravity data at a different surface level.

2.2 Methodologies of Geoid Determination

On the global scale, the geoid can be represented in terms of a spherical harmonic expansion. On local and regional scales, a geoid model based on gravity can be obtained by using Stokes integration and LSC. The spherical harmonic representation and Stokes integration are deterministic, while LSC is stochastic.

2.2.1 Spherical Harmonic Representation of Gravity Field

According to Newton's law of gravitation, the earth gravitation at point P can be expressed as (Fig 2-1) (Torge, 1989)

$$b = G \iiint_M \frac{r' - r}{|r' - r|^3} dm \qquad (2\text{-}1)$$

where r' and r are the geocentric position vectors of the element mass dm and the attracted point P.
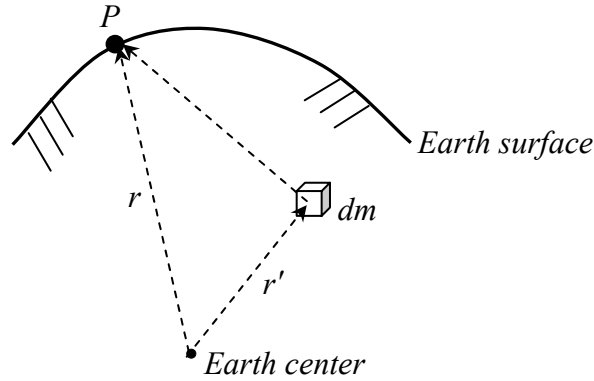
Fig. 2-1 Potential at point P due to the earth mass.

The corresponding potential V and the earth gravitation b have the relationships

$$b = grad \ V \qquad (2\text{-}2)$$

Thus, the gravitational potential of the earth can be given by

$$V_{earth} = G \iiint_M \frac{1}{|r' - r|} dm = G \iiint_M \frac{\rho}{|r' - r|} dv \qquad (2\text{-}3)$$

where ρ and dv are the earth's density and volume element, respectively. $\lim_{r \to \infty} V = 0$. V is harmonic outside the spheroid and can be determined by using a spherical harmonic function given by (Torge, 1991)

$$V = \frac{GM}{r} \left(1 + \sum_{l=2}^{\infty} \left(\frac{a}{r} \right)^n \sum_{m=0}^{n} (\overline{C}_{nm} \cos m\lambda + \overline{S}_{nm} \sin m\lambda) \overline{P}_{nm} (\cos \vartheta) \right) \qquad (2\text{-}4)$$

where a is the semimajor axis of the ellipsoidal earth model and GM is the geocentric gravitational constant with respect to the total mass. λ, ϑ, and r are spherical coordinates and $\overline{C}_{nm}$ and $\overline{S}_{nm}$ are fully normalized spherical harmonic coefficients, which are mass integrals that represent the mass distribution within the central body. $\overline{P}_{nm}$ is the associated Legendre function with degree n and order m. The gravity anomaly and geoid undulation in the spherical harmonic function can be expressed as (Heiskanen and Moritz, 1967)

$$\Delta g_{long} = \frac{GM}{R^2} \sum_{n=2}^{N} (n-1) \sum_{m=0}^{n} \left(\overline{C}_{nm} \cos m\lambda + \overline{S}_{nm} \sin m\lambda \right) \overline{P}_{nm} (\sin\phi) \tag{2-5}$$

and

$$N_{long} = R \sum_{n=2}^{N} \sum_{m=0}^{n} \left(\overline{C}_{nm} \cos m\lambda + \overline{S}_{nm} \sin m\lambda \right) \overline{P}_{nm} (\sin\phi) \tag{2-6}$$

where R is the radius of the earth. The long-wavelength features of the earth's external gravity field are determined by using satellite gravimetry and are modeled as a series of solid spherical harmonics truncated at the maximum values of n and m. The spherical harmonic function is usually used along with the spherical harmonic coefficients to determine the global long-wavelength geoid or gravity field.

2.2.2 Stokes Integration

As shown in Heiskanen and Moritz (1967), the disturbing potential, T, can be determined by Stokes integration as

$$T(\phi, \lambda) = \frac{R}{4\pi} \iint_{\sigma} S(\psi) \Delta g \, d\sigma \tag{2-7}$$

where Δg is gravity anomaly. σ represents the unit sphere and $d\sigma$ denotes the element of solid angle. $S(\psi)$ is Stokes' kernel and is expressed as

$$S(\psi) = \frac{1}{\sin(\psi/2)} - 6\sin\frac{\psi}{2} + 1 - 5\cos\psi - 3\cos\psi \ln(\sin\frac{\psi}{2} + \sin^2\frac{\psi}{2}) \tag{2-8}$$

Using Bruns' formula, we can obtain the geoid undulation as

$$N = \frac{R}{4\pi\gamma} \iint\limits_{\sigma} S(\psi)\Delta g d\sigma \qquad (2\text{-}9)$$

where γ denotes the normal gravity. In theory, Stokes integration can simply be calculated by using global gravity data coverage. However, in a geoid computation task, the RCR procedure is required in order to determine the geoid surface more accurately. Stokes integration is usually calculated rapidly in the frequency domain by using a fast Fourier transform (FFT) technique. On a sphere, a rigorous implementation of FFT can apply the spherical FFT or multi-band FFT technique (Forsberg and Sideris, 1993).

2.2.3 Least Squares Collocation

LSC can be used to determine an anomalous gravitational field by using different combinations of geodetic observations. The basic principle of LSC is given by (Moritz, 1980)

$$s = C_{sl}(C_{ll} + D)^{-1}l \qquad (2\text{-}10)$$

where s and l are sets of signals and observations, respectively. C_{ll} is the covariance matrix of l and C_{sl} is the covariance matrix between s and l. D is the matrix of the noise vector, which functions as a filter and weight in LSC computations. To estimate the error of signal s, the error covariance matrix is computed as (Moritz, 1980)

$$E_{ss} = C_{ss} - C_{sl}C_{ll}^{-1}C_{ls} \qquad (2\text{-}11)$$

where E_{ss} denotes the error covariance matrix. In the case of geoid determination by LSC, the formulae of signal and error are

$$N = \left(C_{Ng}\right)\left(C_{gg} + D_g\right)^{-1}\left(\Delta g\right) \qquad (2\text{-}12)$$

and

$$\delta n^2 = s \left(C_{NN} - \left(C_{Ng} \right) \left(C_{gg} + \frac{1}{s} D_g \right)^{-1} \left(C_{Ng} \right)^T \right) \tag{2-13}$$

where vector Δg contains gravity anomalies. C_{Ng} and C_{gg} are covariance matrices for geoid-gravity and gravity-gravity, respectively. D_g is a diagonal matrix containing error variances of gravity anomalies. In (2-13), s is a scale factor, which can be determined by

$$s = \left(\frac{\sum_{i=1}^{i=m} (\Delta g_i - \Delta \overline{g})^2}{m} - \frac{\sum_{i=1}^{i=m} \delta g_i^2}{m} \right) \Bigg/ c_{gg} \tag{2-14}$$

where $\Delta \overline{g}$ is the average gravity anomaly, δg^2 is error variance of gravity anomalies, c_{gg} is error variance of the gravity anomalies derived from a geopotential model, and m is the number of gravity data points.

The covariance function provides the covariance between two signals, between two observations, and between a signal and an observation, and it is used in LSC to predict those signals that are of interest to us. The key factor for a precision geoid model by LSC is covariance functions. Thus, it is essential to find a suitable covariance function for use in LSC computation. In this study, for up to 360 degrees, we adopt the error anomaly degree variances of a geopotential model ; for higher degrees, we adopt the Tscherning-Rapp anomaly degree variance model 4. The Tscherning-Rapp model is generated from an empirical covariance function developed by Tscherning and Rapp (1974). The Model 4 of anomaly degree variance is expressed as

$$\sigma_n^2(\Delta g, \Delta g) = \frac{A(n-1)}{(n-2)(n+B)} s^{n+2} \tag{2-15}$$

s can be expressed as

$$s = \left(\frac{R_B}{rr'}\right)^2 \qquad\qquad\qquad (2\text{-}16)$$

where n denotes the selected degree. A and B are both free parameters whose values are adopted to be 425.28 mgal^2 and 24 in this study and R_B is the radius of the Bjerhammar sphere. r and r' are the distances of points P and Q from the earth's center. We can determine the covariance between two points by using data obtained at different levels, such as airborne and surface gravity data. Eq (2-15) is used only for $n > 360$. Based on the combination of the geopotential model and the Tscherning-Rapp degree variance model 4, the covariance functions between two gravity anomalies, between two disturbing potentials, and between a gravity anomaly and a disturbing potential for points P and Q can be expressed as

$$C_{\Delta g \Delta g}(P,Q) = \sum_{n=2}^{360} \tilde{\sigma}_n(\Delta g, \Delta g) s^{n+2} P_n(\cos \Psi_{PQ}) + \sum_{n=361}^{\infty} \frac{A(n\text{-}1)}{(n\text{-}2)(n+B)} s^{n+2} P_n(\cos \Psi_{PQ}) \qquad (2\text{-}17)$$

$$C_{TT}(P,Q) = \sum_{n=2}^{360} \tilde{\sigma}_n(T_p, T_Q) s^{n+1} P_n(\cos \Psi_{PQ}) + R^2 \sum_{n=361}^{\infty} \frac{A}{(n\text{-}1)(n\text{-}2)(n+B)} s^{n+1} P_n(\cos \Psi_{PQ}) \qquad (2\text{-}18)$$

$$C_{\Delta g T}(P,Q) = \sum_{n=2}^{360} \tilde{\sigma}_n(T_p, \Delta g_Q) s^{n+1} P_n(\cos \Psi_{PQ}) + \left(\frac{R^2}{r}\right) \sum_{n=361}^{\infty} \frac{A}{(n\text{-}2)(n+B)} s^{n+1} P_n(\cos \Psi_{PQ}) \qquad (2\text{-}19)$$

$$C_{nn}(P,Q) = \frac{1}{\gamma^2} C_{TT}(P,Q) \qquad\qquad\qquad (2\text{-}20)$$

where $\tilde{\sigma}_n(\Delta g, \Delta g)$, $\tilde{\sigma}_n(T_p, T_Q)$, and $\tilde{\sigma}_n(T_p, \Delta g_Q)$ are the error variances between two gravity anomalies, between two disturbing potentials, and between a gravity anomaly and a disturbing potential, respectively; these error variances are associated with the corresponding geopotential model coefficients. P_n is the Legendre polynomial of degree n and Ψ_{PQ} is the spherical distance between P and Q. γ denotes normal gravity. More covariance functions such as those between two geoid gradients, between a geoid gradient and a gravity anomaly, and between a geoid gradient and a disturbing potential can be found in Tscherning and Rapp (1974).

The rapid developments in LSC over the past few years clearly demonstrate that LSC is being used as the primary technique for local geoid determination because it can accurately estimate the signals of interest to us by using heterogeneous data having different resolutions. Due to the multi-resolution characteristic of LSC, we select LSC for the primary geoid modeling methodology in this study.

2.3 Remove-Compute-Restore Procedure

The RCR procedure is one of the most well-known strategies used for regional geoid determination. The RCR procedure is also called the remove-restore technique. In theory, geoid determination can only be performed for gravity data having a global coverage; however, a global gravity field model may represent data far beyond the area of interest. If the RCR procedure is used, gravity field data beyond the area of interest can be removed. In areas with complex topographies, it is very important to remove and subsequently restore the potential of the topography. For these areas, terrestrial gravity values are usually available locally at accessible spots; the remove procedure makes these values more smooth and representative. For many years, because of the valuable characteristics of the RCR procedure, considerable attention has been focused on the application of the RCR procedure to geoid modeling. Furthermore, when performing geoid determination, long-wavelength and short-wavelength errors may arise if the RCR procedure is not properly applied.

The geoid and gravity field can be divided into three parts: long-wavelength (low-frequency), intermediate-wavelength (intermediate-frequency or so-called residual), and short-wavelength (high-frequency) parts. Therefore, both the height anomaly ζ and the gravity anomaly Δg can be expressed as

$$\zeta = \zeta_{long} + \zeta_{res} + \zeta_{short} \tag{2-21}$$

and

$$\Delta g = \Delta g_{long} + \Delta g_{res} + \Delta g_{short} \tag{2-22}$$

where ζ_{long} and Δg_{long} are the long-wavelength height anomaly and gravity anomaly, respectively; ζ_{short} and Δg_{short}, the short-wavelength height anomaly and gravity anomaly, respectively; and ζ_{res} and Δg_{res}, the residual height anomaly and

gravity anomaly, respectively. Fig 2-2 shows geoid undulations at three different wavelengths. In the RCR procedure, the long- and short-wavelength parts are attributed to geopotential-derived and residual terrain model (RTM)-derived effects, respectively. Local gravity observations subtracted from the two gravity effects can be used in Stokes integration or LSC to determine the intermediate-wavelength geoid. Subsequently, the geopotential-derived and RTM-derived geoid effects can be restored to obtain the final geoid.
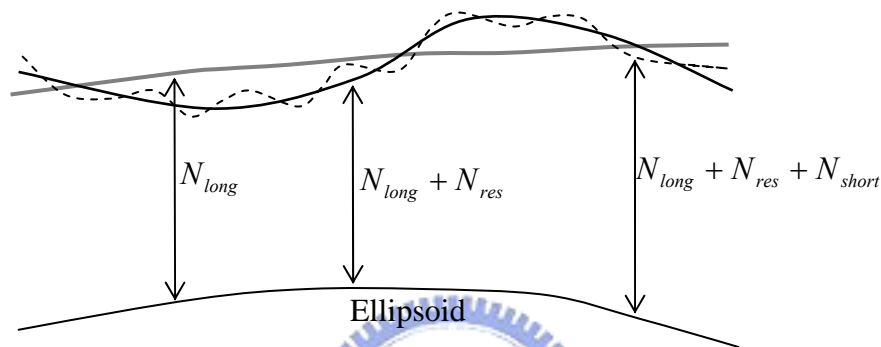
Fig. 2-2 Three different wavelengths of geoid undulation. N_{long}, N_{res}, and N_{short} denote the long-, intermediate- (residual), and short-wavelength parts of geoid undulation, respectively.

In this study, the long-wavelength gravity and geoid are based on a global geopotential model, and the intermediate geoid is obtained by local gravity data by LSC.

2.3.1 Long-Wavelength Reference Geopotential Model

The global geopotential model (GGM) is a model that can represent the earth's potential field. This model is important for regional geoid determination because it takes care of the long-wavelength part of geoid.

For geopotential-derived gravity, the higher the degree and order used for the geopotential coefficients, the smaller is the area required with local gravity data, but errors in high-degree coefficients can be a problem if not carefully modeled. The factors influencing the accuracy of the GGM include the amount and quality of local gravity and satellite tracking data and the maximum degree of the model. In addition,

the GGM usually yields an absolute geoid height error (so-called long-wavelength error) of the order of a few decimeters due to biases. However, the relative geoid height is often accurate because the biases at two computational points will largely be canceled out when differential geoid height computations are performed.

2.3.2 Residual Terrain Model

The RTM represents the residual part between the true and mean elevation surfaces (Fig 2-3). For determining the short-wavelength geoid in high mountainous regions, it may be insufficient to use only the geopotential model and local gravity observations. This is due to the signal contribution of the topography, which is particularly strong at short wavelengths for a rough terrain. The effect of the RTM can represent these short-wavelength signals appropriately.
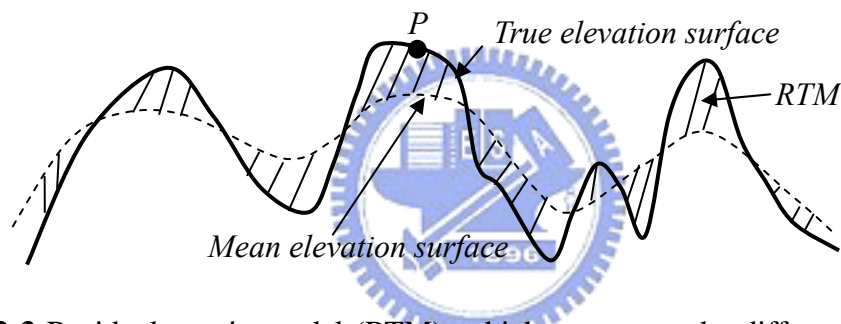
Fig. 2-3 Residual terrain model (RTM), which represents the difference between the true and mean elevation surfaces.

The RTM-derived effect can be expressed as the difference between two surface-derived effects. In a planar approximation, the potential of point P due to an RTM mass is

$$V = G \iiint_{RTM} \frac{dm}{\sqrt{(x - x_p)^2 + (y - y_p)^2 + (z - s)^2}} \tag{2-23}$$

where dm is a mass element of RTM and (x_p, y_p, z_p) and (x, y, z) are the coordinates of point P and every mass element dm, respectively. It is important to use both the true and mean elevation surfaces in geoid computation. The true elevation surface should be represented by a digital elevation model (DEM) containing detailed

information in order to take into account high-frequency signals. The mean elevation surface should be selected in such a manner that it represents the global distribution of the regionally varying signal characteristics as far as possible. The practical computational methods for the RTM-derived effects are described in chapter 4. Three such methods used for computing the effects are investigated.

2.4 Quasi-Geoid Correction

The difference between the geoid and a quasi-geoid is that the geoid corresponds to a datum of orthometric height and the quasi-geoid to that of normal height (Fig 2-4). By considering the normal gravity gradient with respect to the surface of the mean reference ellipsoid, the quasi-geoid is defined as a function of the normal height (Vanicek et al., 1999). In practice, when orthometric heights are used for determining the vertical datum, a quasi-geoid correction is applied to the fundamental formula of physical geodesy in order to accurately determine the geoid.
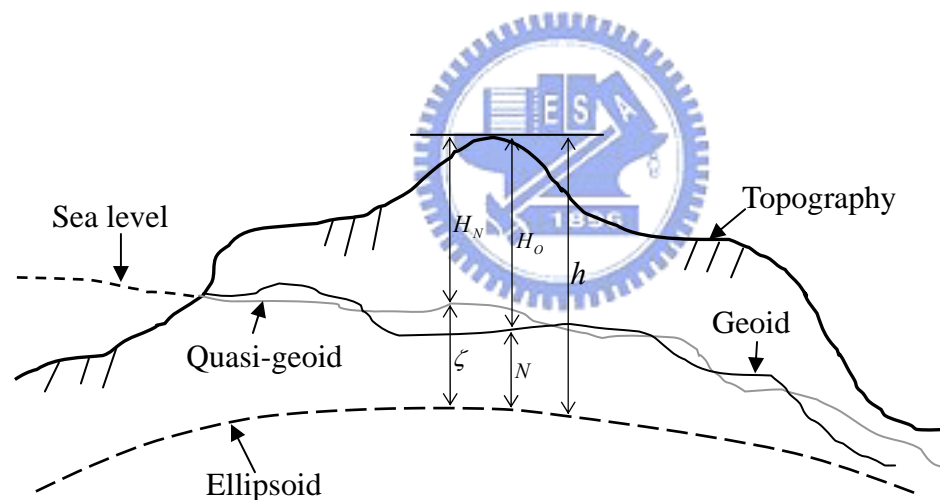
Fig. 2-4 Physical surface of the earth. h, H_O, H_N, N, and ζ denote the ellipsoid height, orthometric height, normal height, geoid undulation, and quasi-geoid undulation, respectively.

The relationship between the height anomaly ζ and the geoid undulation N is expressed as (Heiskanen and Moritz, 1967)

$$\zeta - N \approx - \frac{\Delta g_B}{\gamma} H \tag{2-24}$$

where Δg_B is the Bouguer anomaly, γ is normal gravity, and H is the topographic height. Eq (2-24) can also be written as

$$N \approx \zeta - \frac{2\pi G\rho}{\gamma} H^2 \tag{2-25}$$

where ρ is the density of the terrain mass and G is the gravitational constant. $2\pi G\rho$ is the Bouguer term. The difference between the geoid and the quasi-geoid is minute over moderate topographies, but it can reach several decimeters over high mountainous areas. Thus, the quasi-geoid correction cannot be ignored over rough terrains.

2.5 Upward and Downward Continuations

UW/DWC is employed to calculate the potential at any point above/below a planar surface having a known potential. It is important to apply UWC and DWC to airborne gravimetry for assessing the quality of airborne gravity data and for computing geoid undulation. However, the characteristics of the two continuation operations are different. UWC is a smooth operation that is characterized as a well-posed problem, whereas DWC is an unstable operation that is characterized as an ill-posed problem.

An inverse problem is expressed as the solution of an operator equation by the following expression:

$$d = A(m) \tag{2-26}$$

where m is a function obtained from a metric space of model parameters, d is an element obtained from a metric space of data sets, and A is an operator. According to the classical theory of inverse problems, there are three definitions for well-posed and ill-posed problems (Zhdanov, 2002). A well-posed problem must satisfy the following conditions.

(1) Solution m of Eq (2-26) exists.

(2) Solution m of Eq (2-26) is unique.

(3) Solution *m* depends continuously on the left-hand side of the equation, i.e., on *d*.

The problem in Eq (2-26) is ill-posed if one of the three conditions fails. The gravity potential outside the mass of earth satisfies the Laplace equation

$$\nabla g = 0 \tag{2-27}$$

The gravity potential at some level $z = 0$ is assumed as

$$U(x, y, z) = U(x, y, 0) = f(x, y) \tag{2-28}$$

where $f(x, y)$ is some known function. If the problem is to calculate the potential from $z = 0$ to any other level $z = h$, it is called an UWC of the gravity potential. In contrast to UWC, if the problem is to compute the potential from $z = h$ to $z = 0$, it is called a DWC of the gravity potential. We can write an operator equation of the relationship between the potentials at $z = h$ and $z = 0$ as

$$\begin{cases} U(x, y, 0) = A[U(x, y, h)] & \text{upward} \quad \text{continuation} \\ U(x, y, h) = A[U(x, y, 0)] & \text{downward} \quad \text{continuation} \end{cases} \tag{2-29}$$
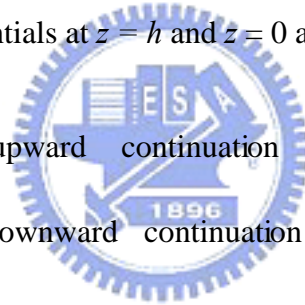
where A is an operator used for calculating the UW/DWC of the gravity potential.

UWC is usually used to assess the accuracy of airborne gravity observations. These airborne data can be compared with the surface gravity data that are upward continued to the flight altitude. DWC plays a key roll in geoid determination when using airborne gravity data. On the other hand, the estimation of downward-continued data is sensitive to noise. Therefore, some types of noise suppression operations are required to enhance the data quality.

In this study, two UW/DWC methods, FFT and LSC, are taken into consideration. Both methods have been applied to UWC and DWC for many years.

2.5.1 Continuation by Fast Fourier Transform

UW/DWC by the FFT method is based on the integral Poisson formula. If an airborne gravity survey is carried out at a constant altitude, DWC can be readily

implemented by using FFT in the frequency domain. Let the vertical component of the gravity field in the $z = 0$ and $z = h$ planes be

$$g(x, y, z)|_{z=0} = g(x, y, z = 0) \qquad\qquad (2\text{-}30)$$

and

$$g(x, y, z)|_{z=h} = g(x, y, z = h) \qquad\qquad (2\text{-}31)$$

where z is the altitude of gravity field g. For the three-dimensional condition, the relationship between $g(x, y, z = 0)$ and $g(x, y, z = h)$ can be written as (Buttkus, 2000)

$$g(x, y, z = h) = \frac{h}{2\pi} \int_{-\infty}^{\infty} \int_{-\infty}^{\infty} \frac{g(\alpha, \beta, 0)}{\left[h^2 + (x - \alpha)^2 + (y - \beta)^2 \right]^{\frac{3}{2}}} d\alpha d\beta \qquad\qquad (2\text{-}32)$$

We can use a convolution integral to represent Eq (2-32) as

$$g(x, y, z = h) = w_{upward}(x, y)|_{z=0}^{h} * g(\alpha, \beta, 0) \qquad\qquad (2\text{-}33)$$

where

$$w_{upward}(x, y)|_{z=0}^{h} = \frac{1}{2\pi} \left(\frac{h}{(h^2 + x^2 + y^2)^{\frac{3}{2}}} \right) \qquad\qquad (2\text{-}34)$$

$w_{upward}(x, y)|_{z=0}^{h}$ is the impulse response function for UWC from the $z = 0$ plane to the $z = h$ plane. On the other hand, the two-dimensional Fourier transform is given by

$$W(f_x, f_y) = \int_{-\infty}^{\infty} \int_{-\infty}^{\infty} w(x, y) e^{-i2\pi(f_x x + f_y y)} dx dy \qquad\qquad (2\text{-}35)$$

where $w(x, y)$ is a nonperiodic function of real variables x and y. $W(f_x, f_y)$ represents $w(x, y)$ in the two-dimensional wavenumber domain. f_x and f_y denote the numbers of cycles per unit distance. If $w(x, y)$ is substituted in Eq (2-34), the corresponding wavenumber response function becomes

$$W_{UWC}(f_x, \ f_y)\,|_{z=0}^{z=h} = \int_{-\infty}^{\infty}\int_{-\infty}^{\infty} \frac{he^{-i2\pi(f_x x + f_y y)}}{2\pi(h^2 + x^2 + y^2)^{3/2}} dxdy$$

$$= e^{-2\pi h\sqrt{f_x^2 + f_y^2}} \tag{2-36}$$

where $f_r = \sqrt{f_x^2 + f_y^2}$. Therefore, the UWC from the $z = 0$ plane to the $z = h$ plane can be expressed in the wavenumber domain as

$$G(f_x, \ f_y)\,|_{z=h} = e^{-2\pi h f_r} G(f_x, \ f_y)\,|_{z=0} \tag{2-37}$$

In contrast to UWC, the wavenumber response function of DWC from the $z = h$ plane to the $z = 0$ plane is given by

$$G(f_x, \ f_y)\,|_{z=0} = \frac{G(f_x, \ f_y)\,|_{z=h}}{e^{-2\pi h f_r}} = e^{2\pi h f_r} G(f_x, \ f_y)\,|_{z=h} \tag{2-38}$$

DWC by FFT is essentially a high-pass filtering operation that will amplify short-wavelength noise in data processing. Therefore, the DWC procedure used for airborne gravity is a very unstable process, and it will result in a rapid increase in noise, particularly at high flight altitudes. To reduce the noise, a filtering or smoothing technique should be applied to the FFT downward-continued method. Thus, Eq (2-38) becomes

$$G(f_x, \ f_y)\,|_{z=0} = e^{2\pi h f_r} G(f_x, \ f_y)\,|_{z=h}\ S(f_x, \ f_y) \tag{2-39}$$

where $S(f_x, \ f_y)$ is a low-pass filter in the wavenumber domain. If f_r approximates to infinity, $G(f_x, \ f_y)\,|_{z=0}$ approximates to zero such that

$$\lim_{f_r \to \infty} = e^{2\pi h f_r} G(f_x, \ f_y)\,|_{z=h}\ S(f_x, \ f_y) = 0 \tag{2-40}$$

In this study, UWC by FFT will be used to compare airborne and surface gravity

data, and DWC by FFT will be applied to geoid modeling. These investigations are described in chapter 5 and chapter 6, respectively.

2.5.2 Continuation by Least Squares Collocation

UW/DW C can also be performed by LSC in either the spectral domain or the spatial domain (Sideris, 1995). Although processing by LSC is not performed as rapidly as that by FFT, the advantage of LSC is that it provides a scheme that can combine airborne gravity data with surface gravity or other heterogeneous data. The equation for the case in which the gravity field at level h_1 UW/DWC to level h_2 can be expressed as

$$\Delta g_{h_2} = \left(C_{g_{h_1} g_{h_2}} \right) \left(C_{g_{h_1}} + D_{g_{h_1}} \right)^{-1} \left(\Delta g_{h_1} \right) \tag{2-41}$$

where $C_{g_{h_1} g_{h_2}}$ is the covariance matrix for gravity at level h_1 and level h_2 and $C_{g_{h_1}}$ is the covariance matrix for gravity at level h_1. $D_{g_{h_1}}$ is the variance of noise of the gravity data obtained at level h_1. In this study, $C_{g_{h_1} g_{h_2}}$ and $C_{g_{h_1}}$ are both determined by using the combination of GGM and the Tscherning-Rapp degree variance model 4. DWC by LSC in spatial domain will be used for investigating geoid modeling in chapter 6. Eq (2-41) is just one of the LSC downward continuation methods used in this study. Another method that involves direct use for geoid determination is also introduced in chapter 6.

Chapter 3
Data for Geoid Modeling

3.1 Introduction

The data used for geoid modeling in this study mainly include the local gravity data, GGM, and DEM. They are used in the calculation of the residual long-wavelength and short-wavelength gravity or geoid. In addition, the altimeter-derived data and a density model are also considered in geoid modeling. In this study, the airborne gravity data is the most important; it has been discussed in detail in chapter 5. To evaluate the gravimetric geoid models, 38 high-quality GPS/leveling points are employed to assess the geoid accuracy.

3.2 Surface Gravity

3.2.1 Land Gravity

Land data (Fig 3-1(a)) were collected during 1980–2003 by Academia Sinica, Base Survey Battalion and Ministry of Interior (MOI), Taiwan (Yen et al., 1990; Yen et al., 1995; Hwang, 2001; Chen, 2003), using LaCoste&Romberg gravimeters (LCR, 1997) tied to some absolute gravity stations. These data were mainly measured along roads at intervals of 2 km between two observations and on geodetic control points. The average data accuracy of Hwang (2001) and Chen (2003) are about 0.04 mgal; they are both based on the adjustments of the relative gravity networks. The total number of land data is 3641. Most land gravity measurements are performed on the west plain. There are only a few gravity points over the Central Range due to the difficulty in performing the survey. Gravity anomalies over flat regions are moderate; however, they become large over the high mountains, reaching values of approximately 200–300 mgal.

3.2.2 Shipborne Gravity

A part of the shipborne gravity data was surveyed by the National Central University (NCU) using the gravimeter R/Vl' Atalante KSS30 in 1996 (Hsu et al., 1998) and the other part was obtained from the National Geophysical Data Center data set of the National Oceanic and Atmospheric Administration (NOAA), USA. In this study, the data was only considered for the locations between 119.2–122.8 E and

21.2–25.8 N (Fig 3-1(b)). Most shipborne data are located over the Pacific Ocean and Bashi Channel. However, fewer data are located over the Taiwan Strait. The standard deviation of the crossover analysis by the NCU and the total shipborne data are 2.6 and 11.2 mgal, respectively. Some bad-quality shipborne data were removed and not subsequently used in geoid modeling. The total number of shipborne data after eliminating the outliers was 4084. There is an obvious local low near the eastern coast, reaching approximately –250 mgal, and the other shipborne data show moderate gravity anomalies.

3.3 Altimeter-Derived Gravity

Recently, altimeter-derived data has assumed more importance in marine geoid computations due to the major developments in satellites with altimetry missions and a rapid increase in the altimeter-derived data coverage. Although the altimeter-derived data usually provides lower accuracy than shipborne gravity data, it is sometimes more useful than shipborne data in geoid modeling; this is because obtaining a considerable amount of data for marine gravimetry is time-consuming and expensive.

In this study, we select the data from the KMS02 model for the geoid modeling investigations. KMS02 gravity field was modeled according to the GEOSAT mission and ERS using the DGM-E04 and JGM-3 orbit models (Anderson et al., 2003). The gravity model improved the quality and coverage of the altimetric height observations, particularly in the coastal regions. The region located between 119.2–122.8 E and 21.8–25.8 N was selected with a 2-min grid spacing (Fig 3-1(c)). Some outliers, particularly near the coast and over shallow water, were removed to enhance the geoid accuracy. As compared to shipborne gravity, the KMS02 data exhibited better coverage over the Taiwan Strait; therefore, it could compensate for the lack of shipborne gravity data and enhance the geoid accuracy over this area.

3.4 Geopotential Model

We adopted the EIGEN-GL04C coefficients for the computations of the long-wavelength geoid and gravity and of the error anomaly degree variances from 2° to 360° in the LSC. The EIGEN-GL04C coefficients were determined by GFZ Potsdam and GRGS Toulouse. These coefficients were determined from the GRACE and LAGEOS missions (from 2003 to 2005) and the $0.5° \times 0.5°$ gravimetry and

altimeter-derived data (GFZ, 2006); with regard to spherical harmonic coefficients, degree and order 360 up to a wavelength of 110 km was developed.

The EIGEN-GL04C model significantly improves the knowledge of the gravity field of the Earth. As compared to the other geopotential models (e.g., EGM96, EIGEN-CG01C, and EIGEN-CG03C), the EIGEN-GL04C model exhibits an improvement of approximately 3–10 cm in the geoidal heights obtained from the GPS/leveling points over USA, Canada, and Europe. Fig 3-2 shows the gravity anomalies and geoidal heights of EIGEN-GL04C up to degree and order 360 globally and over Taiwan. Both gravity anomalies and geoid heights over Taiwan significantly vary from 200 to –200 mgal and 12 to 28 m, respectively, because of the complex terrain. Both these parameters are higher over the Central Range and lower at the Ryukyu arc.

3.5 Digital Elevation Model

Three DEMs with different resolutions—$9'' \times 9''$, $90'' \times 90''$, and $6' \times 6'$—are used in the RTM investigation (Fig 3-3). Because bathymetry is not considered in this study, all the elevations at sea level in the three DEMs are zero. The $9'' \times 9''$ and $90'' \times 90''$ models, which are both considered to be true elevation surfaces, are applied to the inner and outer zone computations. The $6' \times 6'$ model is considered to be the mean elevation surface. The reason for the division of the RTM computation task into two zones has been described in chapter 4.

All these DEMs were sampled from a high-resolution DEM, which is formed on a $3'' \times 3''$ grid (with a horizontal resolution of approximately 80 m) using photogrammetry by the Aerial Survey Office belonging to the Forest Bureau (Hwang et al., 2003a), Taiwan. The accuracy of the $3'' \times 3''$ DEM is approximately 4 m rms determined by comparing with the hundreds of benchmarks with precise elevations.

3.6 Density Model

The density data used in this study were provided by Chiou (1997). According to the distribution of rocks over Taiwan, the density data were obtained by associating each type of rock with an average density and stored in a $5' \times 5'$ grid. The density model has been validated by reliable seismology data. Fig 3-4 shows a color map of the density over Taiwan. The densities are relatively low and are mostly below 2.0 g

cm^{-3} over the west plain. Over the high mountains, the densities are much higher, and the highest density can reach approximately 3.0 g cm^{-3}. In Fig 3-4, the average density on land is 2.35 g cm^{-3}. Therefore, the rock density over Taiwan has an obvious variation and cannot be assumed to be the global density constant—2.67 g cm^{-3}.

3.7 GPS/Leveling Points for Evaluation

The general method for the evaluation of a geoid is a comparison with external data. Geoid height differences can be compared with the differences obtained from the GPS/leveling points. According to this method, the gravimetric geoid models are compared to the available GPS/leveling benchmarks with the observed geoidal heights. An observed geoidal height is the difference between the GPS-derived ellipsoidal height (from 24-h observations and at cm-level accuracy) and the precision leveling-derived orthometric height (at mm-level accuracy). Rigorous orthometric corrections have been incorporated into these GPS/leveling routes (Hwang and Hsiao, 2003; Hwang et al., 2007a). These GPS/leveling benchmarks can be divided into four routes (Fig 3-5). The north route is located at the northern coast of Taiwan; the east route lies in a valley, and the center and south routes are situated from the hills to the mountains and plains to the mountains, respectively. Geoid variation is moderate along the north (approximately 1 m) and east routes (approximately 3 m); however, it is considerable along the center and south routes (approximately 8 m).
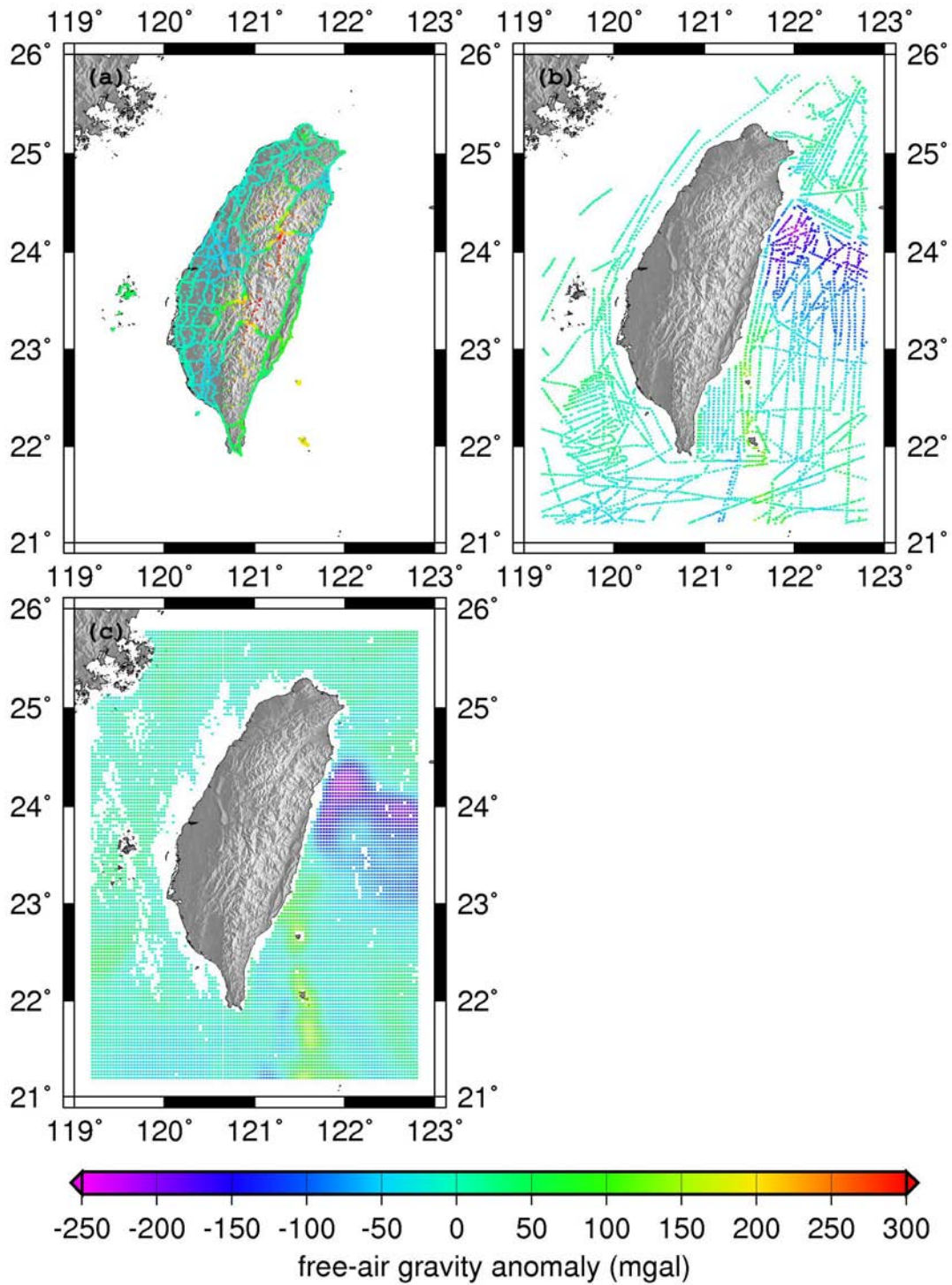
Fig. 3-1 Distributions and free-air gravity anomalies of surface and altimeter-derived gravity. (a) Land data. (b) Shipborne data. (c) Altimeter-derived data. The total number of land, shipborne, and altimeter-derived data are 3641, 4084, and 10228, respectively.
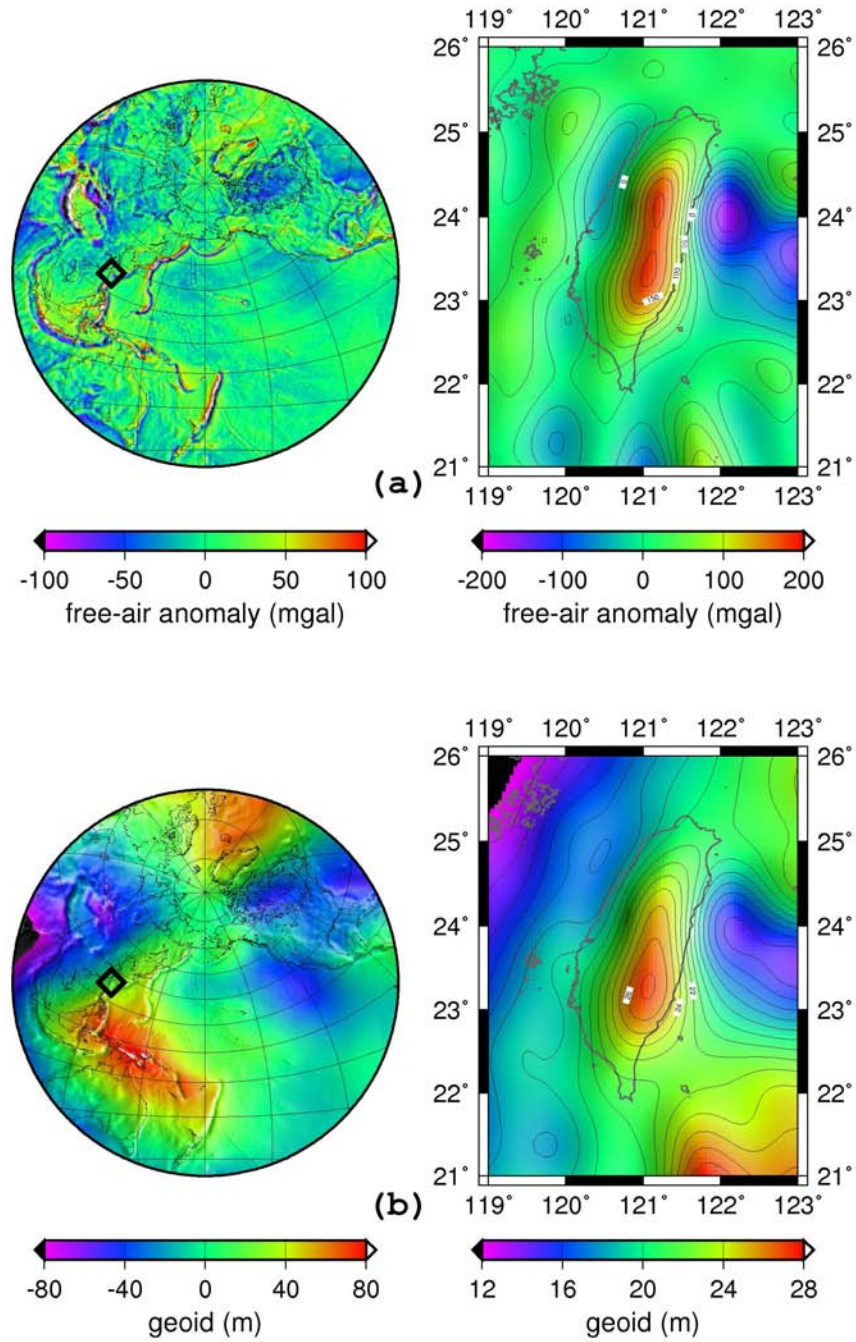
Fig. 3-2 (a) Gravity anomalies and (b) geoid heights globally and over Taiwan obtained from the EIGEN-GL04C coefficients.
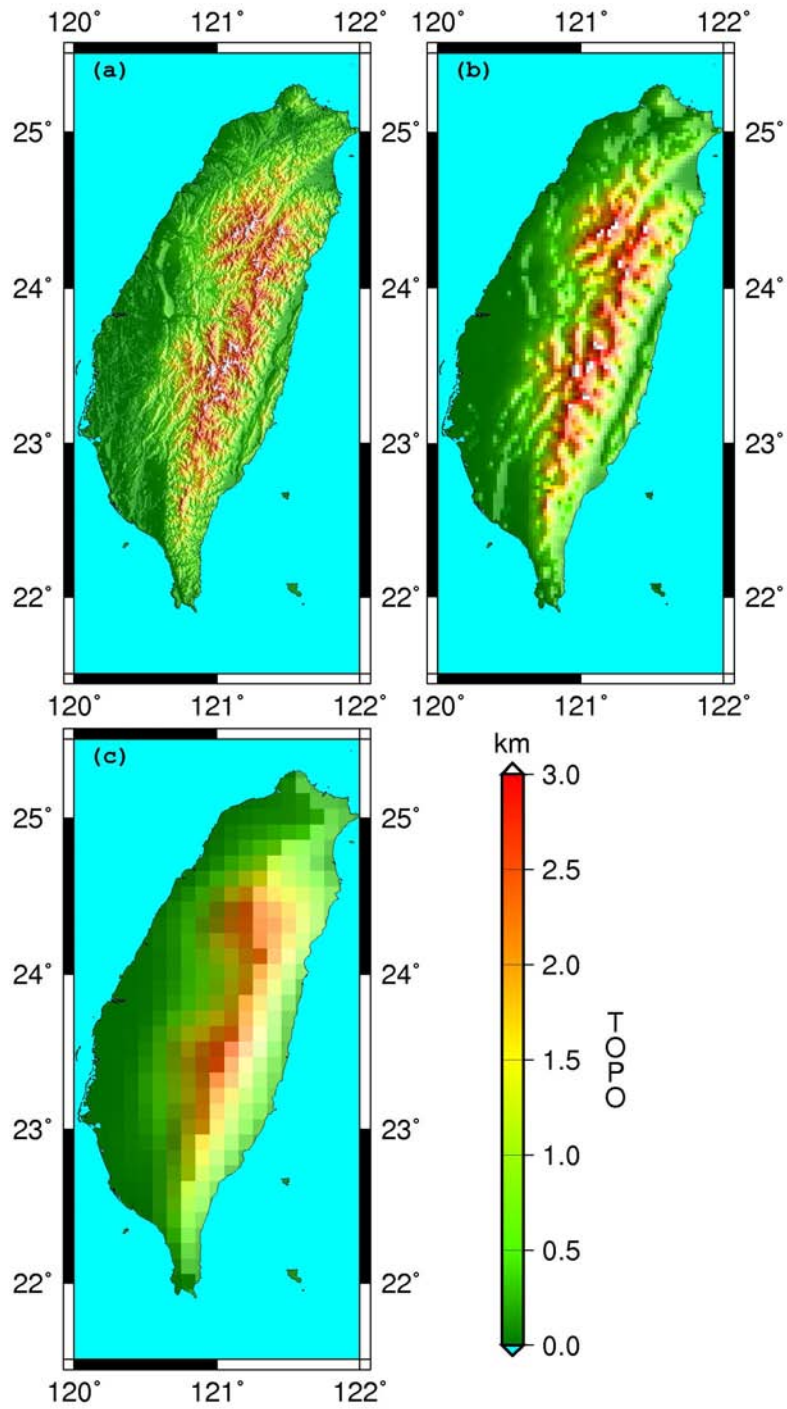
Fig. 3-3 DEMs used in the geoid modeling. The resolutions of the DEMs are (a) 9 s, (b) 90 s, and (c) 6 min. The elevations at the sea level are zero.
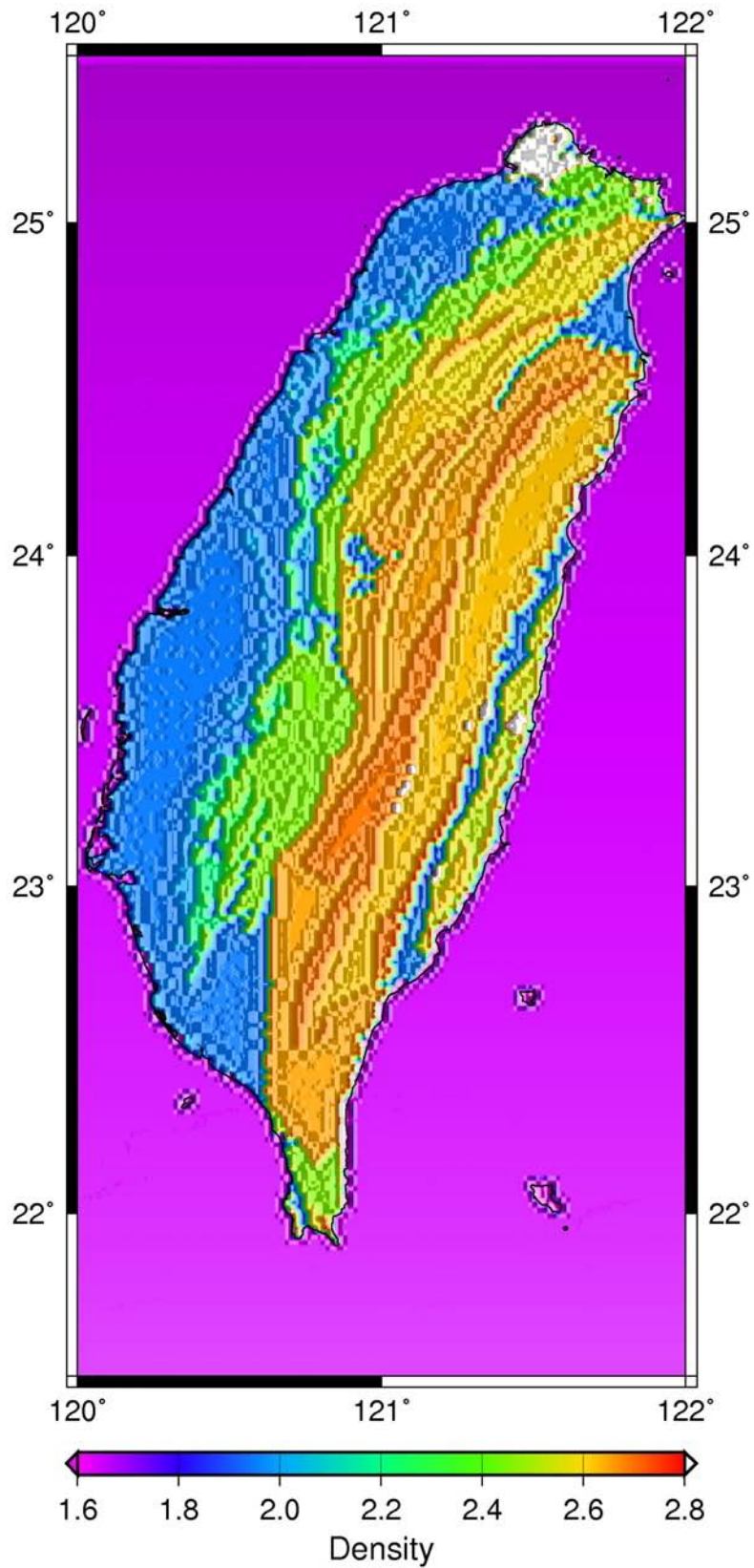
Fig. 3-4 Density model over Taiwan (unit: g/cm^3). Data are stored in a 5-min grid. The average density on land is 2.35 g/cm^3.
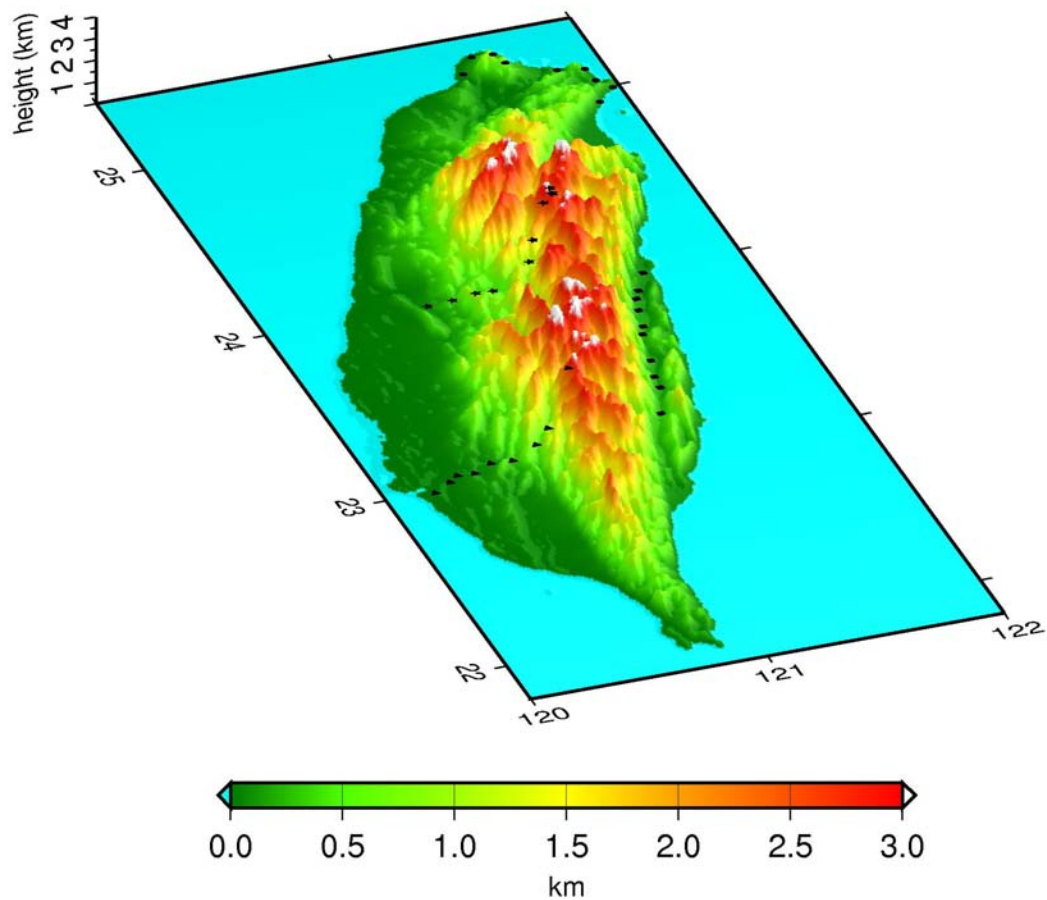
Fig. 3-5 Four leveling routes for evaluating the geoid accuracy. Circles represent the benchmarks along the north leveling route, which lies along the north coast; stars denote the center route, which is spread from the hills to the high mountains; triangles represent the south route, which is located from the plains to the high mountains; squares correspond to the east route, which lies at a valley. The colors denote the topography.

Chapter 4

RTM Effects in Geoid Modeling: Comparison of Three Methods

4.1 Introduction

We investigate three different methods—FFT, prism, and Gaussian quadrature—for the computation of RTM-derived effects in order to determine the most appropriate one for geoid modeling. Among these, the FFT method is a gridwise computation technique and the other two are pointwise computation methods. In the prism method, a density model of a topographic mass is taken into consideration.

4.2 RTM Effects by FFT

Although various methods are available for RTM-derived effects computation, the most commonly used method is the FFT technique due to its computational speed. The main characteristic of this method is that it uses gridded information and returns the RTM-derived effect values for all the points on a grid. RTM-derived effects can be considered as the difference between two Bouguer reductions of true and mean topographic surfaces. Thus, the computation in this method requires at least two DEMs representing the two surfaces. The approximate expression for the RTM-derived effect on gravity can be expressed as follows (Forsberg, 1984):

$$\Delta g_{RTM}(x_p, y_p) = 2\pi G\rho \left(h - h_{ref}\right) - c(x_p, y_p) \tag{4-1}$$

where $c(x_p, y_p)$ is the terrain correction at point P; h and h_{ref}, the elevations of the true and mean DEMs, respectively; G, the gravitational constant; and ρ, the mass density. $c(x_p, y_p)$ can be computed in frequency domain. The terrain correction term in Eq (4-1) can be expressed in the convolution form as follows (Schwarz et al., 1990):

$$c(x_p, y_p) = \frac{1}{2} G\rho \left[h^2 * f - 2h_p(h * f) + h_p^2 g\right] \tag{4-2}$$

where $f = \dfrac{1}{r^3}$, $g = \int_E \dfrac{1}{r^3} dxdy$, $r = \sqrt{x^2 + y^2}$, and E is the domain of integration in the X-Y plane. Further, h_p is the elevation of point P; E, the domain of integration in the X-Y plane; and $*$, the convolution operator. If $t_1 = h^2 * f$ and $t_2 = h * f$, they can be expressed by Fourier transform as follows:

$$F(t_1) = F(h^2 * f) = F(h^2)F(f) \tag{4-3}$$

and

$$F(t_2) = F(h * f) = F(h)F(f) \tag{4-4}$$

Subsequently, t_1 and t_2 can be obtained by inverse Fourier transform as follows:

$$t_1 = F^{-1}\big(F(h^2)F(f)\big) \tag{4-5}$$

and

$$t_2 = F^{-1}\big(F(h)F(f)\big) \tag{4-6}$$

It is necessary to introduce the equation for deriving the RTM gravitational potential at point P to model RTM-derived geoid effects. This equation can be expressed as follows:

$$
\begin{aligned}
T_{RTM} &= G\rho \iint_{x\,y} \int_{h_{ref}}^{h} \frac{dxdydz}{l} \\
&= G\rho \iint_{x\,y} \int_{h_{ref}}^{h} \frac{dxdydz}{\sqrt{(x - x_p)^2 + (y - y_p)^2 + (z - h_p)^2}}
\end{aligned}
\tag{4-7}
$$

According to Bruns formula, which is given by $N = T/\gamma$, the RTM-derived effect on geoid yields

$$N_{RTM}(x_p, y_p) = \frac{G\rho}{\gamma} \iint_{x\,y} \int_{h_{ref}}^{h} \frac{dxdydz}{\sqrt{(x - x_p)^2 + (y - y_p)^2 + (z - h_p)^2}} \tag{4-8}$$

where γ implies normal gravity. If we assume that the terrain effect on the geoid is small, the term $\dfrac{1}{l}$ becomes

$$\frac{1}{l} = \frac{1}{l_0} - \frac{1}{2}\frac{(h-h_{ref})^2}{l_0^3} + \cdots \tag{4-9}$$

where l_0 is the planar distance. On substituting Eq (4-9) in Eq (4-8), we get

$$
\begin{aligned}
N_{RTM}(x_p, y_p) &= \frac{G\rho(h-h_{ref})}{\gamma}\iint_{x\,y}\frac{dxdy}{l_0} \\
&= \frac{G\rho(h-h_{ref})}{\gamma}\iint_{x\,y}\frac{dxdy}{\sqrt{(x-x_p)^2+(y-y_p)^2}}
\end{aligned}
\tag{4-10}
$$

Eq (4-10) is a linear expression and its higher-order terms are ignored. It can be expressed in the convolution form as follows:

$$N_{RTM}(x_p, y_p) = \frac{G\rho}{\gamma}(h-h_{ref}) * g \tag{4-11}$$

where $g = \iint_{x\,y}\dfrac{dxdy}{\sqrt{(x-x_p)^2+(y-y_p)^2}}$. Eq (4-11) can be expressed by Fourier transform as

$$
\begin{aligned}
F\big(N_{RTM}(x_p, y_p)\big) &= F\left(\frac{G\rho}{\gamma}(h_{res}) * g\right) \\
&= \frac{G\rho}{\gamma}F(h_{res})F(g)
\end{aligned}
\tag{4-12}
$$

where $h_{res} = h - h_{ref}$. Subsequently, the RTM-derived geoid $N_{RTM}(x_p, y_p)$ at point P can be obtained by inverse Fourier transform as follows:

$$N_{RTM}(x_p, y_p) = \frac{G\rho}{\gamma} F^{-1}(F(h_{res}) * F(g)) \tag{4-13}$$

On comparison with other algorithms, the obvious advantage of FFT is its rapid computation, but the unavoidable edge effects and cyclic convolution should be eliminated carefully by 100% zero-padding.

4.3 RTM Effects by Prism

The prism method is a simple technique to estimate RTM-derived effects by pointwise computation. The RTM-derived effects on geoid N_{RTM} and gravity Δg_{RTM} at point P due to the residual terrain mass can be expressed as

$$N_{RTM}(x_p, y_p) = \frac{G\rho}{\gamma} \iint_x \int_y \int_{h_{ref}}^{h_p} \frac{dxdydz}{\sqrt{(x - x_p)^2 + (y - y_p)^2 + (z - h_p)^2}} \tag{4-14}$$

and

$$\Delta g_{RTM}(x_p, y_p) = G\rho \iint_x \int_y \int_{z=h_{ref}}^{z=h_p} \frac{(z - h_p)dxdydz}{[(x - x_p)^2 + (y - y_p)^2 + (z - h_p)^2]^{3/2}} \tag{4-15}$$

These effects can be decomposed into a combination of many prisms. We can calculate the effect at point $P(x_p, y_p, h_p)$ as the sum of the mass of each prism (Fig 4-1) and add all the prism-derived effects within a selected zone. Thus, the RTM-derived gravity or geoid effects can be obtained. The equations for calculating these two effects by the prism method can be expressed as follows:

$$N_{RTM}(x_p, y_p) = G\rho \sum_{i=1}^{n} \frac{\Delta x \Delta y \Delta z}{\sqrt{(x_i - x_p)^2 + (y_i - y_p)^2 + (z_i - h_p)^2}} = G\rho \sum_{i=1}^{n} \frac{\Delta x \Delta y \Delta z}{l_i} \tag{4-16}$$

and

$$\Delta g_{RTM}(x_p, y_p) = G\rho \sum_{i=1}^{n} \frac{(z - h_p)\Delta x \Delta y \Delta z}{[(x_i - x_p)^2 + (y_i - y_p)^2 + (z_i - h_p)^2]^{3/2}} = G\rho \sum_{i=1}^{n} \frac{\Delta x \Delta y \Delta z}{l_i^3} \tag{4-17}$$

where Δx, Δy, and Δz are the lengths of each prism in the x, y, and z directions, respectively. Therefore, Δx and Δy can be considered as the grid sizes of the used

true DEM and Δz, its residual elevation. Residual elevation is the difference between the mean and true elevations. The total number of prisms selected is n. In this study, in addition to the case where ρ is constant, we also consider the case where ρ is variable. Subsequently, Eq (4-16) and (4-17) become

$$N_{RTM}\left(x_p, y_p\right) = G\sum_{i=1}^{n} \frac{\Delta x \Delta y \Delta z \rho(x_i, y_i)}{\sqrt{(x_i - x_p)^2 + (y_i - y_p)^2 + (z_i - h_p)^2}} = G\sum_{i=1}^{n} \frac{\Delta x \Delta y \Delta z \rho(x_i, y_i)}{l_i} \qquad (4\text{-}18)$$

and

$$\Delta g_{RTM}\left(x_p, y_p\right) = G\sum_{i=1}^{n} \frac{(z - h_p)\Delta x \Delta y \Delta z \rho(x_i, y_i)}{\left[(x - x_p)^2 + (y - y_p)^2 + (z - h_p)^2\right]^{3/2}} = G\sum_{i=1}^{n} \frac{\Delta x \Delta y \Delta z \rho(x_i, y_i)}{l^3} \quad (4\text{-}19)$$

Because the prism method is a pointwise computation technique, it requires a considerable amount of time to complete the computational task. To reduce the time-consuming calculation, the most efficient strategy is to split the computational area into two parts—an inner zone with a fine elevation grid and an outer zone with a coarse elevation grid. Fig 4-2 shows the decomposed prisms of the inner and outer zones. The inner zone comprises thinner prisms from the detailed DEM and outer zone comprises thicker ones from the coarser DEM. Theoretically, the prism method is considered the most accurate, but it may be not suitable for the computation of high-resolution output due to its inefficiency.
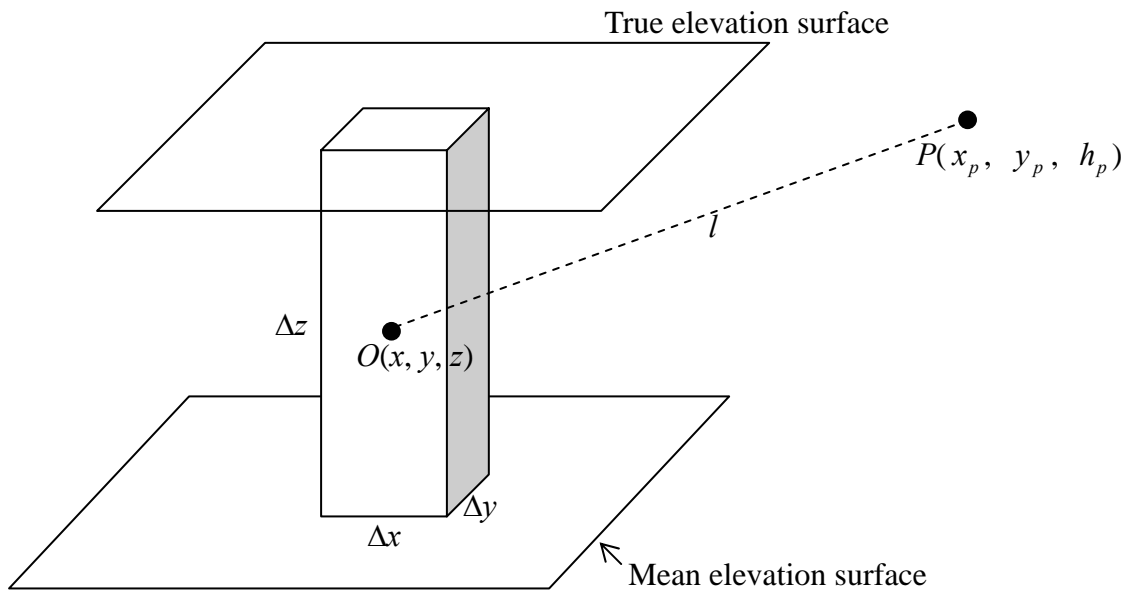
Fig. 4-1 Geometry of the RTM-derived effects in the prism method. This method calculates the potential at point *P* due to the mass of a prism.
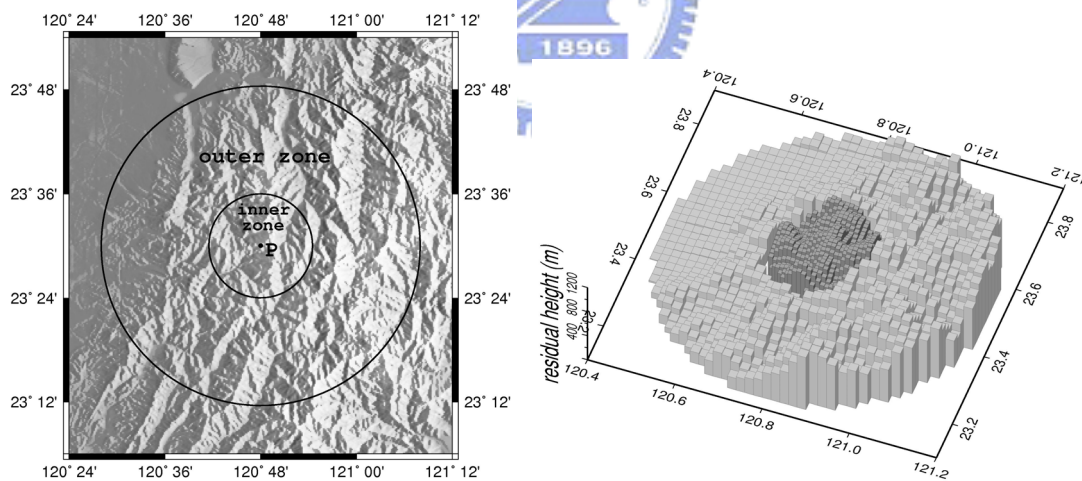
Fig. 4-2 Computational inner and outer zones at point *P*. The black thin and the grey thick prisms shown on the right hand side in the above figure belong to the inner and outer zones, respectively. The residual height denotes the difference between the elevations obtained from the true and mean DEMs.

4.4 RTM Effects by Gaussian Quadrature

The Gaussian quadrature method is a useful technique to obtain the integration of a function over a domain. The Gaussian quadrature theorem is based on a weighted sum of the function values at specified points within the integration domain. This method also belongs to pointwise computation methods. It was successfully employed by Hwang et al. (2003b) in the study of terrain correction.
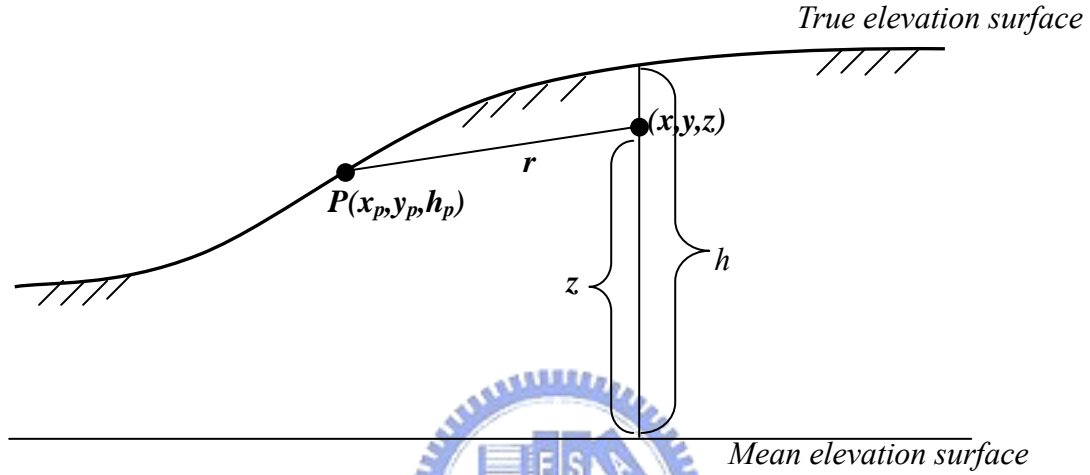
Fig. 4-3 Geometry depicting an RTM-derived effect in the Gaussian quadrature.

According to Eq (4-7), the RTM-derived effects of gravity Δg_{RTM} and geoid N_{RTM} due to the topographic mass above and below a point at $P(x_p, y_p, h_p)$ (Fig 4-3) can be derived as follows:

$$\Delta g_{RTM}(x_p, y_p) = G\rho \iint_x \int_y \int_{z=h_{ref}}^{z=h_p} \frac{(z-h_p)dxdydz}{[(x-x_p)^2 + (y-y_p)^2 + (z-h_p)^2]^{3/2}}$$

$$= G\rho \iint_x \int_y \left[\frac{1}{\sqrt{(x-x_p)^2 + (y-y_p)^2 + ((h-h_{ref}) - (h_p - h_{ref}))^2}} \right.$$

$$\left. - \frac{1}{\sqrt{(x-x_p)^2 + (y-y_p)^2 + (h_p - h_{ref})^2}} \right] dxdy$$

$$= G\rho \iint_x \int_y f_{\Delta g}(x, y) dxdy \tag{4-20}$$

and

$$N_{RTM}(x_p, y_p) = \frac{G\rho}{\gamma} \iint_{x}\iint_{y}\int_{h_{ref}}^{h_p} \frac{dxdydz}{\sqrt{(x-x_p)^2+(y-y_p)^2+(z-h_p)^2}}$$

$$= \frac{G\rho(h-h_{ref})}{\gamma} \iint_{x}\iint_{y} \frac{dxdy}{\sqrt{(x-x_p)^2+(y-y_p)^2}}$$

$$= \frac{G\rho(h-h_{ref})}{\gamma} \iint_{x}\iint_{y} f_n(x,y)dxdy \qquad (4\text{-}21)$$

The RTM-derived geoid is only considered as a linear effect term which is the same as FFT. For a given area bounded by X_1 (west), X_2 (east), Y_1 (south), and Y_2 (north), Eq (4-20) and (4-21) can be numerically integrated as follows (Hwang et al., 2003b):

$$\Delta g_{RTM}(x_p, y_p) = G\rho \int_{X_1}^{X_2}\int_{Y_1}^{Y_2} f_{\Delta g}(x,y)dxdy \approx G\rho \sum_{j=1}^{M} w_j^y c_{\Delta g}(y_j) \qquad (4\text{-}22)$$

and

$$N_{RTM}(x_p, y_p) = \frac{G\rho(h-h_{ref})}{\gamma} \iint_{x}\iint_{y} f_n(x,y)dxdy \approx \frac{G\rho(h-h_{ref})}{\gamma} \sum_{j=1}^{M} w_j^y c_n(y_j) \qquad (4\text{-}23)$$

where

$$c_{\Delta g}(y) = \int_{X_1}^{X_2} f(x,y)dx \approx \sum_{i=1}^{N} w_i^x f_{\Delta g}(x_i,y) \qquad (4\text{-}24)$$

and

$$c_n(y) = \int_{X_1}^{X_2} f(x,y)dx \approx \sum_{i=1}^{N} w_i^x f_n(x_i,y) \qquad (4\text{-}25)$$

where w_i^x and w_j^y are the weighting coefficients; x_i and y_j, the nodal coordinates; and M and N, the numbers of the weighting coefficients and nodes along the x and y axes over the domains $[X_1, X_2]$ and $[Y_1, Y_2]$, respectively (Press et al., 1989). To obtain the highest possible precision, M and N should be the numbers of the given grids along the x and y directions. The values of the function $c(y)$ at nodes x_i and y_j were interpolated using the Newton-Gregory forward polynomial (Gerald and Wheatley, 1994) from the evenly spaced function values on a given grid. For the interpolations required in Eq (4-24) and (4-25), we experimented with various

polynomial degrees and found that the use of degrees higher than six yields no further improvement in the interpolation accuracy. This computation of one-dimensional case was proven to be successful by Press et al. (1989). However, Hwang et al. (2003b) have reported the successful usage of the required two-dimensional Gaussian quadrature.

The main advantage of using the Gaussian quadrature method is the very high-order accuracy it provides with fewer points. This is useful in the cases wherein a function requires a long time to compute by the pointwise method. However, it is also a time-consuming task. Therefore, the Gaussian quadrature method also requires the segregation of the computational area into inner and outer zones to make the computation more efficient. Practical tests reveal that the computation time required by the Gaussian quadrature method is more than that required by the FFT method but less than that required by the prism technique.

4.5 Design of Experiments

The primary objective of this study is to determine the most suitable method for computing RTM-derived effects in geoid modeling. The local gravity data used in this study include land and shipborne data. The altimeter-derived data are not considered. In order to compare the three methods stated above, three geoid models whose RTM-derived effects are created by these methods are compared to the GPS/leveling points to assess their accuracies.

The geoid modeling procedure employed in this study, which is also based on the RCR procedure, is shown in Fig 4-4. In this figure, while carrying out the remove and restore steps during the computation of short-wavelength gravity and geoid, the three methods are taken into account individually. The process of geoid modeling is divided into four cases. The only discrepancy between these cases is that their RTM-derived effects are delivered by the FFT method (case 1), prism method with a constant ρ (case 2), prism method with a variable ρ (case 3), and Gaussian quadrature method (case 4).

The selected radii of the inner and outer zones and the sizes of the output grids of the RTM-derived effects computation are summarized in Table 4-1. Because the FFT method is a rapid computational technique, it does not require the usage of an outer zone in practical calculation. On the other hand, since cases 2~4 are based on the

41

prism and Gaussian quadrature methods, they require inner and outer zones to reduce the time required for computation. Further, in order to make the computations more efficient, the resolutions of the output grids in cases 2~4 have to be stored in coarser grids the resolution of which is set to 1 min in this study. With regard to the radii chosen for the inner and outer zones, the gravity effect will decay more rapidly than the geoid effect with the increase in the distance between the RTM mass and point *P*. Thus, the RTM-derived geoid computation requires longer inner and outer zones' radii than the RTM-derived gravity computation. In cases 2~4, the radii of the inner and outer zones for the gravity computation are 15 and 100 km, respectively, and for geoid computation, 30 and 300 km, respectively. In case 1, the radii of the inner zone for the gravity and geoid computations are 50 and 100 km, respectively.

Table 4-1 Radii of the inner and outer computational zones for the RTM-derived effects and the resolutions of the output grids in the four case models

Case	Effect	Radius of the inner zone	Radius of the outer zone	Output grid resolution
Case 1	RTM gravity	50 km	-	9 s
	RTM geoid	100 km	-	
Case 2	RTM gravity	15 km	100 km	1 min
	RTM geoid	30 km	300 km	
Case 3	RTM gravity	15 km	100 km	1 min
	RTM geoid	30 km	300 km	
Case 4	RTM gravity	15 km	100 km	1 min
	RTM geoid	30 km	300 km	

During computation, the grid sizes of the long-, residual-, and short-wavelength geoid parts are varied taking into account the different resolutions of the GGM, local gravity data, and DEM. The long- and residual-wavelength geoid effects are stored in the 3-min and 1-min grids, respectively. In order to make the grid sizes of the different wavelength geoid effects the same, we employ the GMT package (Wessel and Smith, 1995) to sample all the grids and add individual geoid effects to obtain the final geoid models. The grids sizes of the geoid models obtained in the four cases stated above are equivalent to their RTM geoid models. Therefore, the grids sizes of these four geoid models (cases 1~4) are 9 s, 1 min, 1 min, and 1 min, respectively.
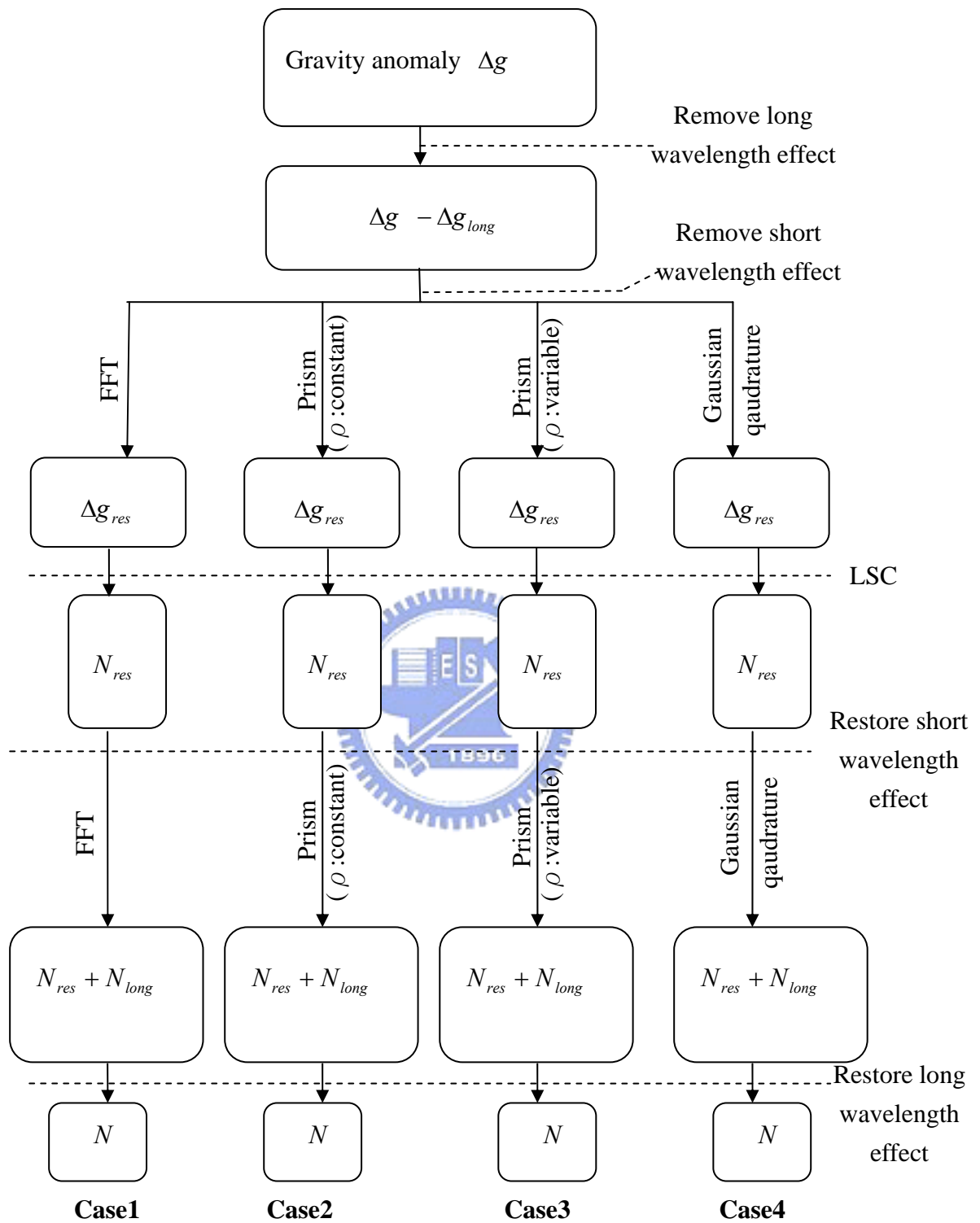
Fig. 4-4 Flowchart for the geoid modeling procedure. The only discrepancy between the four cases is with regard to the method used for the computation of RTM-derived effects.

4.6 Results

4.6.1 Results from RTM-Derived Gravity and Geoid

The RTM-derived gravity anomalies for the four cases are shown in Fig 4-5. The gravity anomaly points consist of land and shipborne gravity data. In this figure, greater gravity anomalies are observed over high mountainous areas with maximum values reaching over ±100 mGal. The anomalies on the western plane and at the sea are very small. Table 4-2 lists the statistics of the results of the four cases. The anomalies in case 1 (FFT) are relatively larger than in the other cases. On the other hand, the anomalies in case 4 (Gaussian quadrature) are slightly smaller than in the other cases. In a few areas with high mountains, the difference between the values calculated by the different methods at the same point is significant, reaching ±30 mgal, but most differences are minor. The average difference between case 2 (constant ρ) and case 3 (variable ρ) is 2 mgal. This implies that the influence of density variation on RTM-derived gravity computation is unremarkable. The standard derivations in cases 1~4 are 25.2, 25.1, 22.9, and 20.9 mgal, respectively.

Table 4-2 Statistics for RTM-derived gravity anomalies (mgal)

Case	Max	Min	Mean	Std. dev.
Case 1	114.1	–165.8	–8.7	25.2
Case 2	115.2	–148.5	–6.7	25.1
Case 3	116.1	–145.7	–5.2	22.9
Case 4	134.5	–143.7	–5.2	20.9

The RTM-derived geoid effects for the four cases are shown in Fig 4-6. The values are computed on regular grids the sizes of which are 9 s for case 1 and 1 min for the other cases. Some high values can reach over 1 m over high mountains, but most values in mild areas are very small. The statistics of the results obtained in the four cases are listed in Table 4-3. In comparison to the effects on gravity anomaly, the geoid heights obtained in case 1 and case 4 are relatively smaller and bigger, respectively, than those obtained in the other cases. The differences between the RTM-derived geoid effects obtained in the four cases at the same computation point

can reach ±10 cm over some rough terrain.

The average difference between case 2 (constant ρ) and case 3 (variable ρ) is about 7 cm. This clearly reveals that the influence of density variation is much stronger on RTM-derived geoid than on RTM-derived gravity. The standard derivations obtained in cases 1~4 for RTM-derived geoid are 0.103, 0.172, 0.166, and 0.184 m, respectively.

Table 4-3 Statistics for RTM-derived geoids (m)

Case	Max	Min	Mean	Std. dev.
Case 1	0.915	−0.306	0.000	0.103
Case 2	0.949	−0.325	0.017	0.172
Case 3	1.035	−0.286	0.024	0.166
Case 4	1.105	−3.650	0.013	0.184

4.6.2 Results of Geoid Modeling

In the residual geoid computation by LSC, the covariances of gravity-gravity anomaly, geoid-gravity anomaly, and geoid-geoid anomaly based on the combination of the EIGEN-GL04C model and Tscherning-Rapp degree variance model 4 are shown in Fig 4-7. The covariances containing shorter spherical distances have higher values. The patterns of the covariance values tends to be mild when the spherical distance exceeds 0.4º. In addition, the variations in the quality of the gravity data must be taken into account in order to determine the noise for different data types. We assign 0.1 and 1.0 mgal data noise to land and shipborne gravity anomalies, respectively. These values are empirical and yield the best results.

The residual gravity anomalies obtained by subtracting the EIGEN-GL04C- and RTM-derived effects from the original gravity anomalies are shown in Fig 4-8. The residual geoid effects obtained by LSC are shown in Fig 4-9. In these two figures, four distinct local low can be observed over the northern, central, and southern regions on land and the eastern region at sea. The minimum value of the residual gravity anomalies and geoids can reach over –150 mGal and –1.5 m, respectively. On the other hand, in the case where higher RTM-derived gravity anomalies are obtained,

smaller residual gravity anomalies are observed. The same result is obtained for the RTM-derived and residual geoids in the four cases considered in this study.

After restoring long and residual wavelength parts of the geoid and considering quasi-geoid correction, we can obtain the final geoid models for the four cases (Fig 4-10). Fig 4-10(a) obviously contains more detailed signals (or noises) over the Central Range due to the higher-resolution grids (9 s). Fig 4-11 shows the differences between the case 1 geoid model and the others. In most areas, the differences are less than ±0.1 m, but there exists a large difference area over the east coast, especially in Fig 4-11(c), reaching 0.5 m. Other large differences occur in the Central Range, which contains complex geoid variations.

Table 4-4 lists the statistics of the differences between the observed and modeled geoidal heights at the four leveling routes. The standard deviations of these differences in the four cases on the north and east routes are all within 8 cm. Most standard deviations on the center and south routes where the current land gravity data are sparsely distributed and the geoid variation is large are over 10 cm. However, we can conclude that case 1 presents the best accuracy as compared to the other cases as it offers the smallest standard deviation, especially in the center route; the standard deviation of 0.144 m in this case is 3~4 cm better than that in the other cases. A comparison of the mean values of case 2 and case 3 listed in Table 4-4 reveals that the maximum difference between the geoid surfaces obtained in these two cases is 4 cm. However, their standard deviations are within 1 cm. This implies that the density variation considered in geoid modeling results in only a very limited improvement in the accuracy of the geoid over the Taiwan Island.

The FFT method is thus more suitable for geoid modeling over Taiwan due to its computational speed and the accuracy of the results obtained in this study, which was the best of all the three methods considered. In the subsequent investigations on geoid modeling, the RTM-derived effects are all delivered by the FFT method.

Table 4-4 Statistics regarding the differences (m) between the observed and modeled geoidal heights at four leveling routes

Method	Leveling route	Max	Min	Mean	Std. dev.
Case 1	North	–0.034	–0.205	–0.130	0.062
	East	–0.186	–0.399	–0.312	0.068
	Center	–0.195	–0.577	–0.350	0.144
	South	–0.330	–0.476	–0.379	0.046
Case 2	North	–0.046	–0.265	–0.154	0.071
	East	–0.213	–0.454	–0.321	0.080
	Center	–0.208	–0.775	–0.435	0.176
	South	–0.235	–0.524	–0.399	0.139
Case 3	North	–0.027	–0.210	–0.138	0.067
	East	–0.294	–0.529	–0.365	0.082
	Center	–0.200	–0.799	–0.444	0.180
	South	–0.227	–0.539	–0.381	0.149
Case 4	North	–0.140	–0.351	–0.249	0.070
	East	–0.292	–0.576	–0.433	0.079
	Center	–0.308	–0.884	–0.543	0.195
	South	–0.233	–0.496	–0.377	0.141

Fig. 4-5 RTM-derived gravity anomalies. (a) FFT method (case 1), (b) prism method: constant density (case 2), (c) prism method: variable density (case3), and (d) Gaussian quadrature method (case 4).
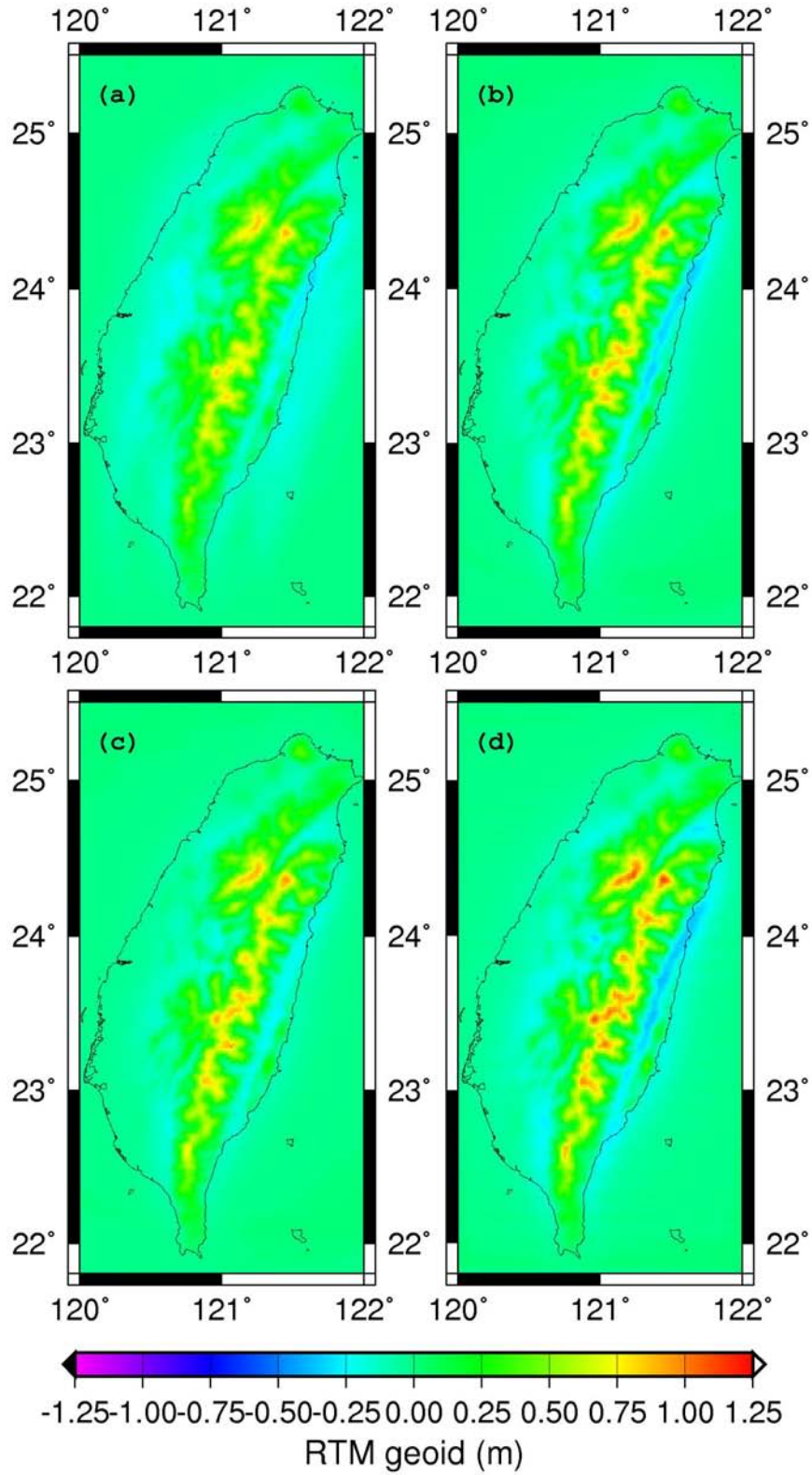
Fig. 4-6 RTM-derived geoids. (a) FFT method (case 1), (b) prism method: constant density (case 2), (c) prism method: variable density (case 3), and (d) Gaussian quadrature method (case 4).

Fig. 4-7 Covariances for (a) surface gravity-surface gravity covariance matrix, (b) geoid-surface gravity covariance matrix, and (c) geoid-geoid covariance matrix.

Fig. 4-8 Residual gravity anomalies. (a) FFT method (case 1), (b) prism method: constant density (case 2), (c) prism method: variable density (case 3), and (d) Gaussian quadrature method (case 4).

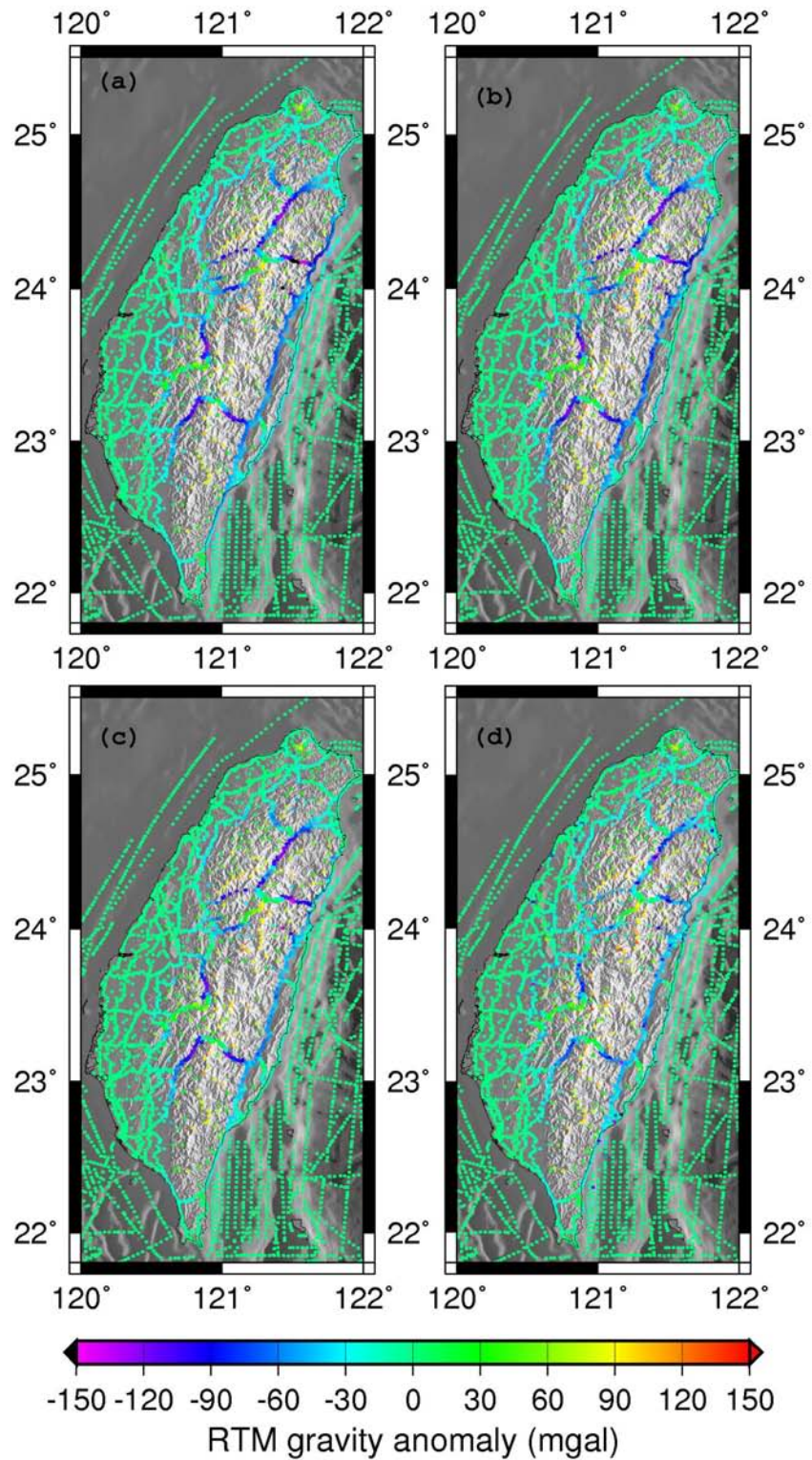**Fig. 4-9** Residual geoids. (a) FFT method (case 1), (b) prism method: constant density (case 2), (c) prism method: variable density (case 3), and (d) Gaussian quadrature method (case 4).
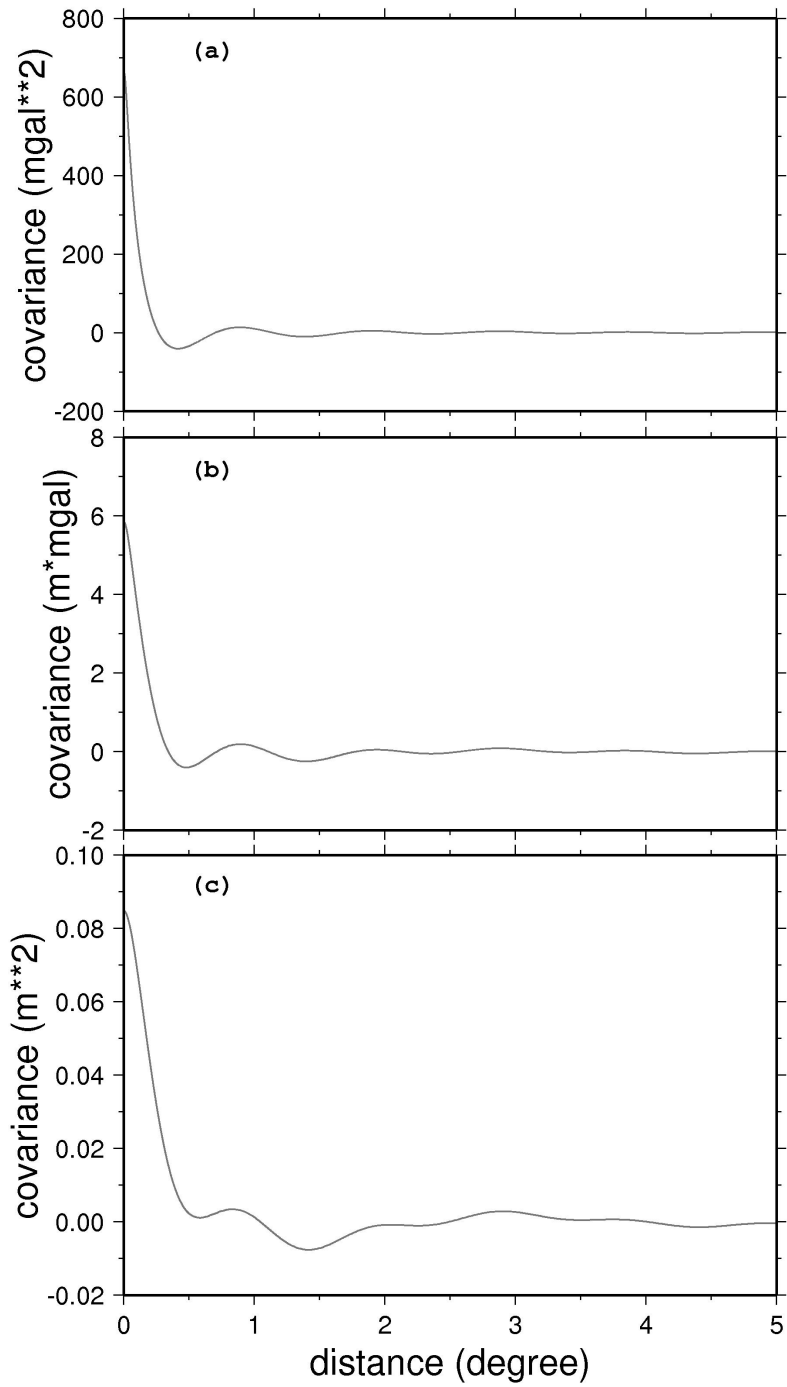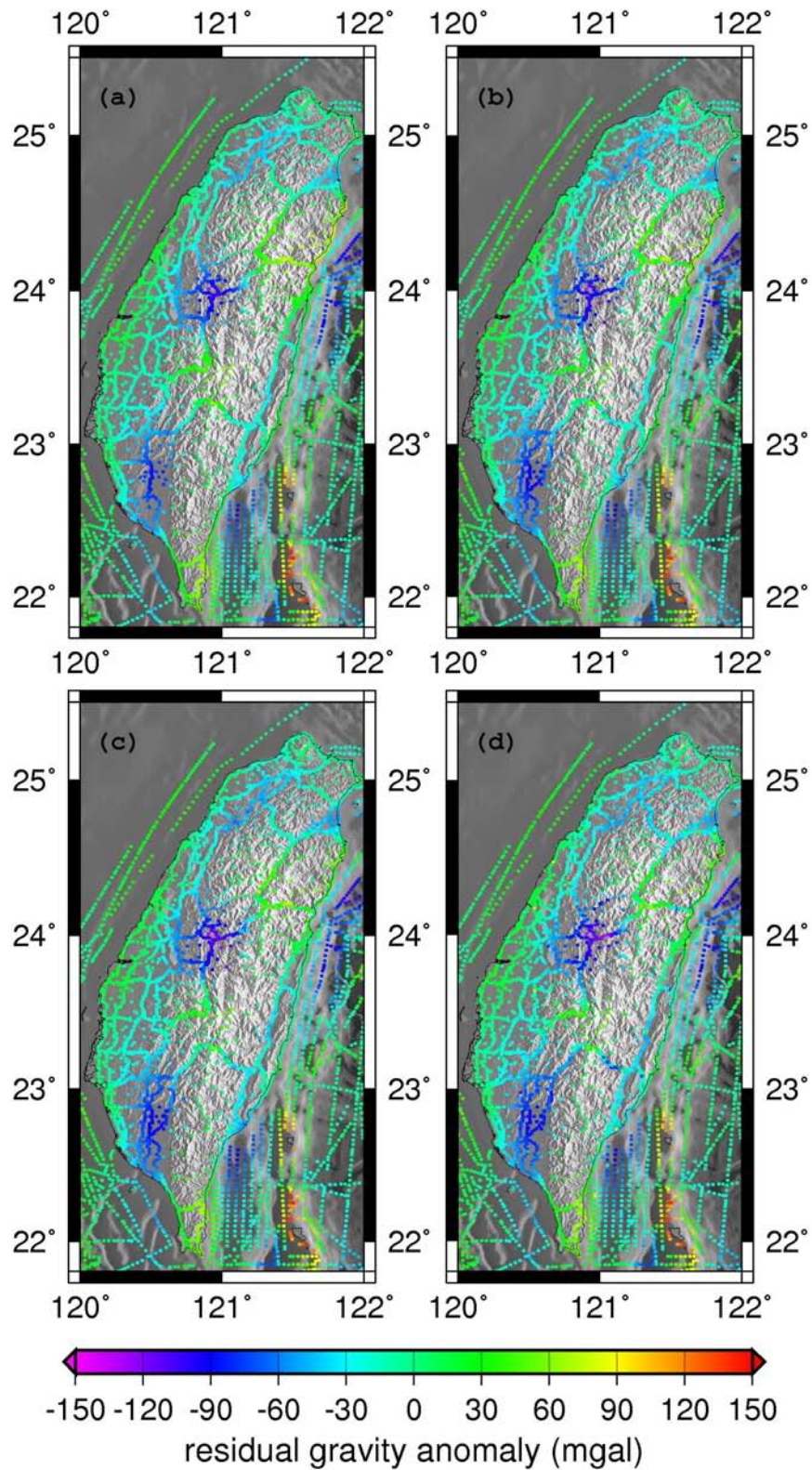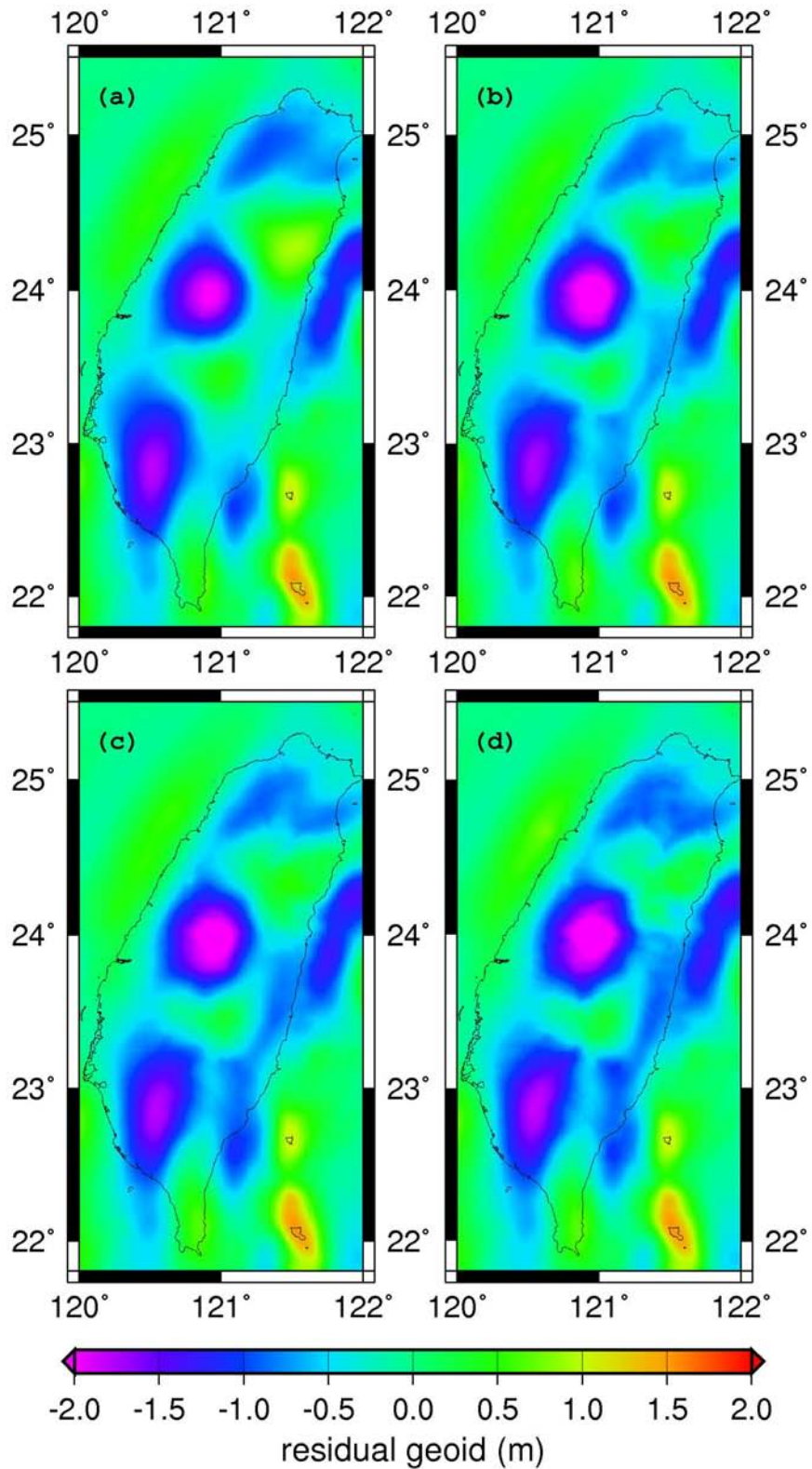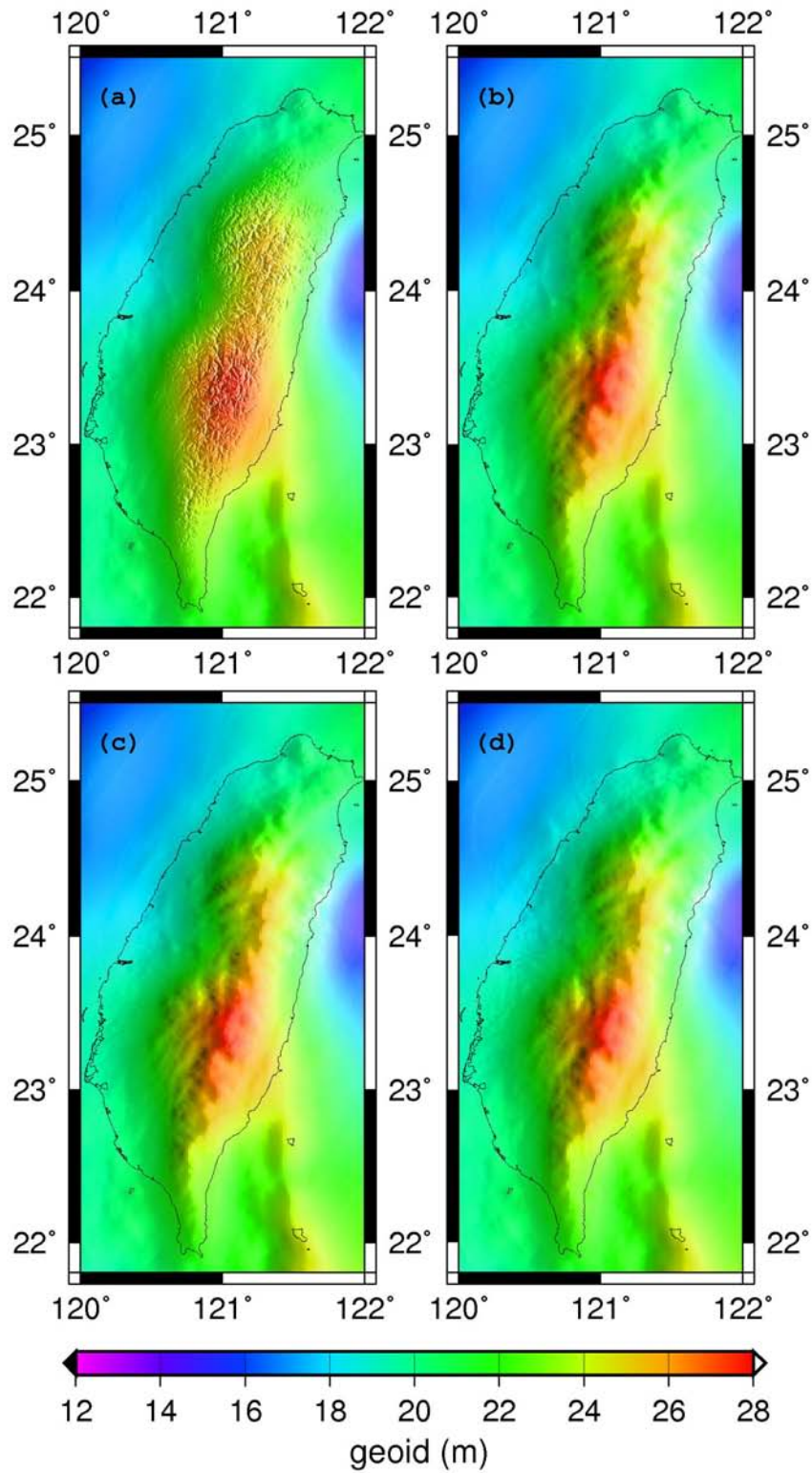
Fig. 4-10 Geoid models obtained in (a) case 1, (b) case 2, (c) case 3, and (d) case 4.
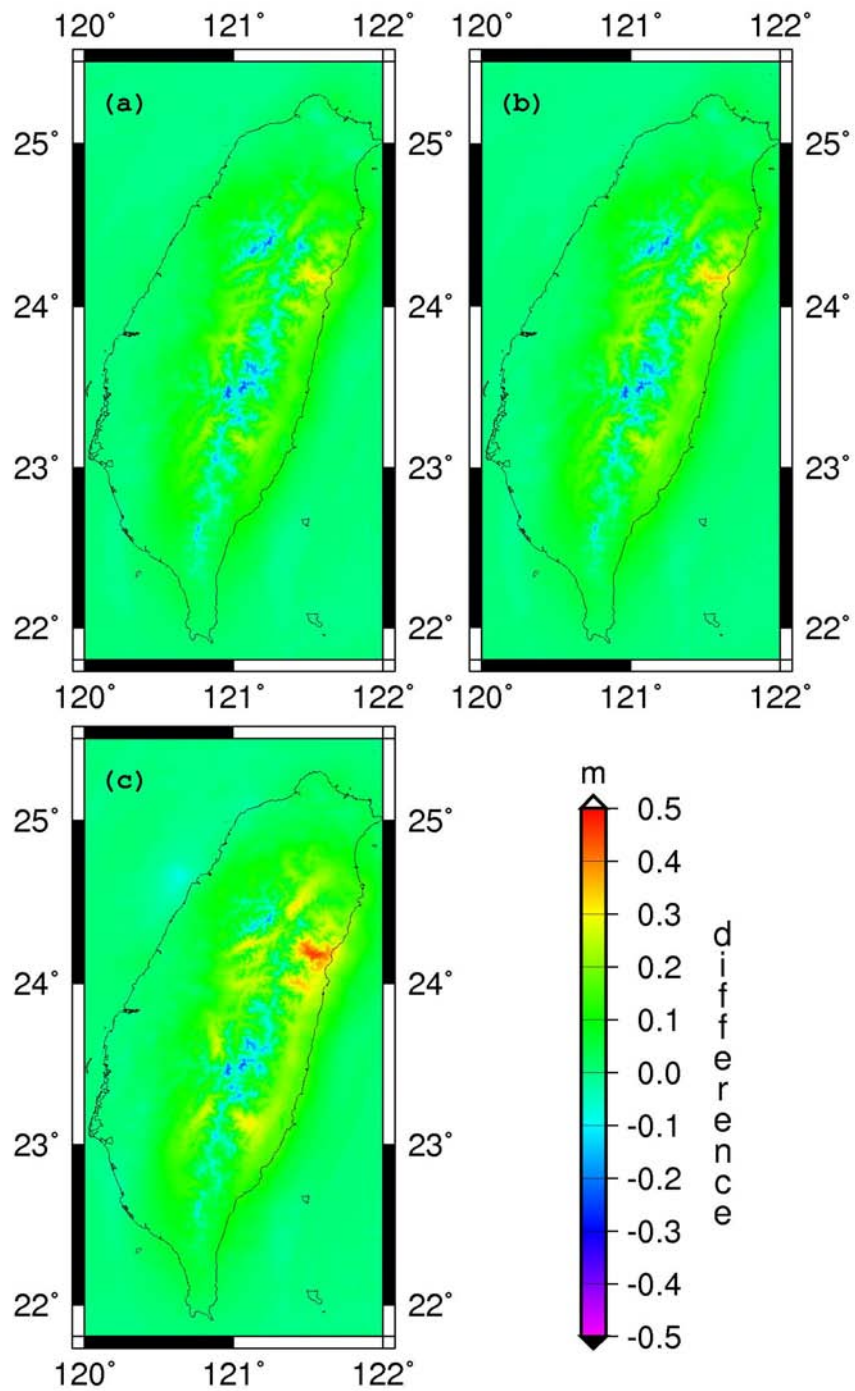
Fig. 4-11 Geoid differences between the geoid models of (a) case 1 and case 2, (b) case 1 and case 3, and (c) case 1 and case 4.

Chapter 5

Airborne Gravity Data of Taiwan

5.1 Introduction

Airborne gravimetry can be used over regions with sparse gravity data coverage. As mentioned in chapter 1, Taiwan's terrain is complex, and it would be difficult to conduct a land gravity survey over its mountainous regions. In order to bridge the gaps in the existing ground gravity coverage (mainly in inaccessible areas), the Ministry of the Interior (MOI) of Taiwan sponsored an airborne gravity survey over the period from May 2004 to May 2005. The entire project including the survey work and software development was carried out by National Chiao Tung University, Taiwan, and National Survey and Cadastre (KMS), Denmark. The survey area covers the entire Taiwan Island and its surrounding seas.

5.2 Data Reduction in Airborne Gravity

5.2.1 Gravity Reduction

Airborne gravimetry can be classified into two types—scalar and vector types. The scalar-type gravimetry employs a relative gravimeter and can be implemented in airborne and oceanic surveys. However, the vector-type component measurements employ the accelerometer of inertial measurement units (IMU), whose accuracy is generally lesser than that of the scalar-type but suitable for gravity measurements of 3D gravity components. The basic equation for a vector-type gravimetry is expressed as follows (Schwarz and Li, 1996):

$$\mathbf{g} = \dot{\mathbf{v}} - (2\mathbf{\Omega} + \mathbf{P})\mathbf{v} - \mathbf{f} \qquad (5\text{-}1)$$

where $\mathbf{g}$ represents the vector of gravity, and $\mathbf{v}$ and $\dot{\mathbf{v}}$ represent the vectors of velocity and acceleration, respectively, of the aircraft. $\mathbf{f}$ represents the specific force sensed by an IMU. $\mathbf{\Omega}$ and $\mathbf{P}$ are both skew-symmetric matrices, which are expressed as (Olesen, 2003)

$$\Omega = \begin{bmatrix} 0 & -\omega\sin\varphi & \omega\cos\varphi \\ \omega\sin\varphi & 0 & 0 \\ \omega\cos\varphi & 0 & 0 \end{bmatrix} \tag{5-2}$$

$$P = \begin{bmatrix} 0 & -\dot{\lambda}\sin\varphi & \dot{\lambda}\cos\varphi \\ \dot{\lambda}\sin\varphi & 0 & 0 \\ \dot{\lambda}\cos\varphi & 0 & 0 \end{bmatrix} \tag{5-3}$$

where ω represents the angular velocity of the earth's rotation in an inertial frame, and $\dot{\lambda}$, the angular velocity along the east–west direction of an aircraft in an Earth-fixed Cartesian frame. The term $(2\Omega + P)\mathbf{v}$ is the *Etövös* effect (Harlan, 1968), which is attributed to the difference between the angular velocity of an aircraft and that of stationary objects. Thus, the gravitational attraction exerted on the aircraft slightly increases or decreases when the aircraft moves along the east or west direction. Eq (5-1) can be separated into three components; these components are expressed as

$$g_e = \dot{v}_e - f_e + \left[2w\cos\phi + \frac{v_e}{R_N + h}\right]\cdot\left[v_u + v_n\tan\phi\right] \tag{5-4}$$

$$g_n = \dot{v}_n - f_n + \left[2w\cos\phi + \frac{v_e}{R_N + h}\right]\cdot\tan\phi\cdot v_e + \frac{v_n v_u}{R_M + h} \tag{5-5}$$

$$g_u = \dot{v}_u - f_u - \left[2w\cos\phi + \frac{v_e}{R_N}\right]v_e - \frac{v_n^2}{R_M} \tag{5-6}$$

where g_e, g_n, and g_u represent the components of gravity along the east–west, north–south, and vertical directions of the aircraft. $\dot{v}_e$, $\dot{v}_n$, and $\dot{v}_u$ represent the accelerations along the east–west, north–south, and vertical directions of the aircraft. f_e, f_n, and f_u are specific force components as observed by a gravimeter. v_e and v_n represent the velocities along the east–west and north–south directions,

respectively, of the aircraft. R_N *and* R_M represent the radii of curvatures along the meridian and prime vertical, respectively. ϕ and *h* represent the latitude and flight height of the aircraft.

Because the airborne gravimeter is placed in a strap-down system, the navigation frame is not the same as the frame of the gravimeter sensors. The sensor frame should be converted into the navigation frame. This means that we need to consider the small difference between the horizontal accelerations recorded by the gravimeter and the GPS measurements. Thus, the rotation of specific forces in Eq (5-1) into the local coordinate frame results in (Olesen, 2003)

$$\mathbf{g} = \dot{\mathbf{v}} - (2\mathbf{\Omega} + \mathbf{P})\mathbf{v} - \mathbf{Rf} \tag{5-7}$$

where R represents the rotation matrix that converts the sensor frame into a navigation frame. This transformation yields

$$\mathbf{R} = \begin{bmatrix} \cos\gamma\sin\beta & \cos\gamma\sin\beta\sin\alpha + \sin\gamma\cos\alpha & -\cos\gamma\sin\beta\cos\alpha + \sin\gamma\sin\alpha \\ -\sin\alpha\cos\beta & -\sin\gamma\sin\beta\sin\alpha + \cos\gamma\cos\alpha & \sin\gamma\sin\beta\cos\alpha + \cos\gamma\sin\alpha \\ \sin\beta & -\cos\beta\sin\alpha & \cos\beta\sin\alpha \end{bmatrix} \tag{5-8}$$

where α, β, and γ represent the three components of the tilt angles of the gravimeter platform. α, β, and γ can be expressed as

$$\begin{cases} \alpha = c(f_x - q_x) \\ \beta = c(f_y - q_y) \\ \gamma = c(f_z - q_z) \end{cases} \tag{5-9}$$

where f_x, f_y, f_z and q_x, q_y, q_z represent the three components produced by the gravimetry sensor and navigation system. *c* represents the conversion factor between f and q. If this correction is considered, Eq (5-6) becomes

$$g_u = \{\dot{v}_u - f_z - \left(\left[2w\cos\phi + \frac{v_e}{R_N}\right]v_e - \frac{v_n^2}{R_M}\right)$$

$$+ \left(\sin \beta \cdot f_x - \cos \beta \sin \alpha \cdot f_y - (1 - \cos \beta \cos \alpha) \cdot f_z \right) \} \qquad \text{(5-10)}$$

The terms $\left(\left[2w \cos \phi + \dfrac{v_e}{R_N} \right] v_e - \dfrac{v_n^2}{R_M} \right)$ and $\left(\sin \beta \cdot f_x - \cos \beta \sin \alpha \cdot f_y - (1 - \cos \beta \cos \alpha) \cdot f_z \right)$

represent the *Etövös* effect and tilt correction of the vertical components, respectively.

5.2.2 Aircraft Positioning

The position, velocity, and acceleration of the aircraft play an important role in airborne gravity surveys (Schwarz and Li, 1997, and Kennedy, 2002). The GPS positioning for airborne gravity used in this survey not only provides a precise flight trajectory position of the aircraft but, more importantly, precisely estimates the first and second derivatives with respect to time for computing the velocity and acceleration required for airborne gravimetry data processing. It is possible to achieve an accuracy of the order of centimeters for the aircraft position (Goad and Yang, 1997). Highly accurate velocities and accelerations can be obtained based on these positions by the use of a precise numerical technique. In this study, the trajectories of the aircraft are determined by using Bernese 5.0 (Beutler et al., 2004) with the IGS precise ephemeris of the GPS.

In the kinematic positioning using Bernese, a number of parameters included in the double-differenced phase observations were estimated together with the aircraft position. These parameters are grouped into two subsets in normal equations (Hwang et al., 2007b):

$$\begin{bmatrix} \mathbf{N_{11}} & \mathbf{N_{12}} \\ \mathbf{N_{21}} & \mathbf{N_{22}} \end{bmatrix} \begin{bmatrix} \mathbf{X_1} \\ \mathbf{X_2} \end{bmatrix} = \begin{bmatrix} \mathbf{C_1} \\ \mathbf{C_2} \end{bmatrix} \qquad \text{(5-11)}$$

where $\mathbf{N_{11}}, \mathbf{N_{12}}, \mathbf{N_{21}}, \mathbf{N_{22}}, \mathbf{C_1}$, and $\mathbf{C_2}$ are the submatrices of the normal equations; subset x_1 contains the ground station coordinates, tropospheric parameters, and phase ambiguities, while subset x_2 contains the epoch-by-epoch kinematic positions of the aircraft. Subset x_2 can be inverted as follows:

$$\mathbf{x}_2 = \mathbf{N}_{22}^{-1}(\mathbf{c}_2 - \mathbf{N}_{21}\mathbf{x}_1) \tag{5-12}$$

We substitute $\mathbf{x}_2$ in Eq (5-11). This yields a new normal equation for $\mathbf{x}_1$

$$(\mathbf{N}_{11} - \mathbf{N}_{12}\mathbf{N}_{22}^{-1}\mathbf{N}_{21})^{-1}\mathbf{x}_1 = (\mathbf{c}_1 - \mathbf{N}_{12}\mathbf{N}_{22}^{-1}\mathbf{c}_2) \tag{5-13}$$

Then, subset $\mathbf{x}_1$ can be solved as

$$\mathbf{x}_1 = (\mathbf{N}_{11} - \mathbf{N}_{12}\mathbf{N}_{22}^{-1}\mathbf{N}_{21})^{-1}(\mathbf{c}_1 - \mathbf{N}_{12}\mathbf{N}_{22}^{-1}\mathbf{c}_2) \tag{5-14}$$

To obtain this solution, the standard stochastic model of the GPS-phase observables was used (Seeber, 2003). In this case, the double-differenced phase observables between the aircraft and the eight tracking stations are selected and used to obtain the final coordinates. The initial values of the kinematic positions (parameter subset $\mathbf{x}_2$) are required for the linearization of the nonlinear GPS observation equations.

5.3 A Taiwan Airborne Gravity Survey

5.3.1 Survey Campaign

The survey lines are shown in Fig 5-1(a). These lines consist of 64 north–south, 22 east–west, 10 northeast–southwest, and 6 northwest–southeast oriented lines with a spacing of 4.5 km, 20 km, 5 km, and 30 km, respectively. The west–east and northwest–southeast lines are mainly used for crossover analyses. The survey area covers the whole of Taiwan Island and its offshore regions. The survey area is approximately 75,000 km^2 and the total distance covered by the survey lines is approximately 53,000 km.

A scalar-type gravimeter called LaCoste and Romberg (LCR) Air-Sea Gravity System II (serial number: S-133) (Fig 5-1(b)) mounted on a laser gyro-stabilized platform is used to record the airborne gravity data at 1 Hz. This gravimeter has a resolution of 0.01 mgal and an accuracy of 1 mgal, as seen from the shipborne test (LCR, 2003). It uses spring tension and beam velocity measurements to obtain the relative gravity variations. Additional information on the Air-Sea Gravity System II gravimeter is summarized in Table 5-1. The gravimeter is placed in a medium-size

aircraft, Beechcraft-200 (Fig 5-1(c)), flying at an average altitude of 5156 m (The spatial resolution is approximately 6 km (Torge, 1989)) at a mean ground speed of approximately 306 km/h. Both the airborne gravimeter and aircraft belong to the Ministry of the Interior, Taiwan.

The King-Air Beechcraft-200 is equipped with a Trimble 5700 GPS receiver (Fig 5-1(d)) that samples data at 2 Hz. For the kinematic positioning of the aircraft, eight ground-based GPS reference stations (Fig 5-1(a)) around Taiwan are used to determine the kinematic solutions. The eight stations are YMSM, SNAM, KDNM, PKGM, TMAM, FLNM, KMNM, and MZUM. The sampling rate of these reference stations is 2 Hz except that of SNAM station, which is 1 Hz. CCK, shown in Fig 5-1(a), is the Taichung airport, where aircraft take off and landing occurred.

The reference gravity value can be determined by a land gravimeter based on the absolute gravity reference points at the Taichung FG5 (Micro-g, 1999) absolute gravity station. The gravity value at the aircraft parking spot was recorded using a Graviton-EG gravimeter (LCR, 2002). The standard error of this gravity value is 0.04 mGal based on the relative gravity network adjustment. A number of gravity base readings of the airborne gravity system need to be obtained during the field survey period to obtain a smooth drift of the airborne gravimeter.

The airborne gravity survey was carried out from May 2004 to May 2005. The survey took 43 days, including 3 days of re-flights where bad data were found. The number of flight hours exceeds 200.

Table 5-1 Overview of the L & R Air-Sea Gravity System II

Resolution	0.01 mGal
Accuracy	<1.00 mGal
Size	$71 \times 56 \times 84$ cm
Weight	116 kg
Power supply	240 W (avg), 450 W (max)
Sampling rate	1 Hz
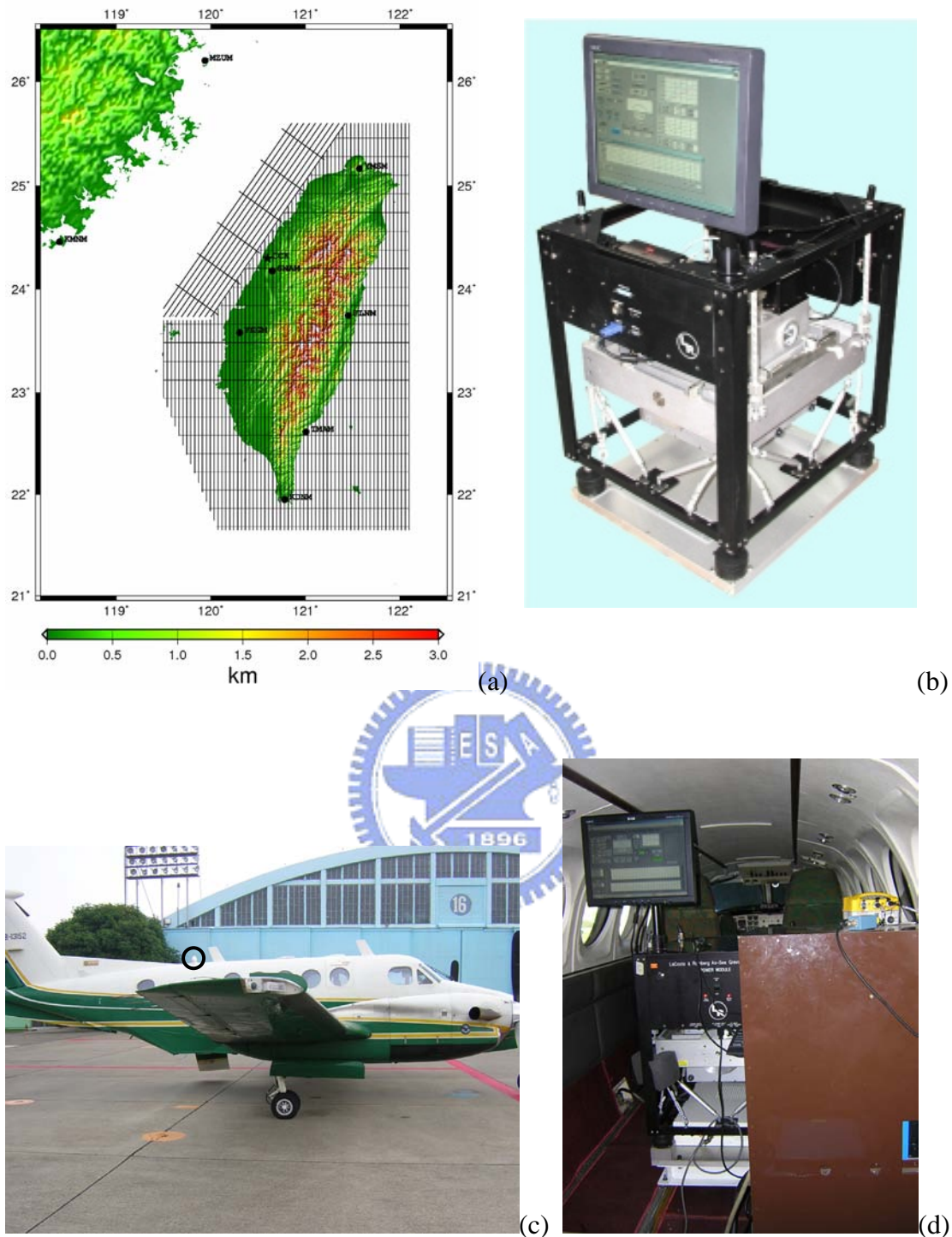
Fig. 5-1 (a) Airborne gravity survey lines and GPS tracking stations (solid circles) for precise aircraft positioning. The star represents the Taichung (CCK) airport, where the King-Air Beechcraft-200 is based. (b) The L&R Air-Sea Gravity System II gravimeter and (c) the King-Air Beechcraft-200 aircraft; the circle denotes the antenna. (d) Inside of the King-Air Beechcraft-200; the L&R Air-Sea Gravity System II and Trimble 5700 are mounted inside the aircraft.

5.3.2 Data Processing

Kinematic GPS solutions are obtained by using the combination of eight different GPS based stations and processed using Bernese 5.0 (Beutler et al., 2004) and the IGS precise ephemeris (http://igscb.jpl.nasa.gov/). In order to determine the velocity and acceleration of the aircraft, we use the program DERIV of the International Mathematical and Statistical Library (IMSL) to perform the numerical differentiations. DERIV first computes the spline interpolants to the input functions (i.e., coordinate components x, y, and z) and then differentiates the spline interpolants to obtain their derivatives (Hwang et al., 2006b). Following the GPS procedure, two data processing techniques have to be considered: correction for time shift and filtering of raw gravity observations.

The time systems of the raw GPS and the gravimeter observations are inconsistent. The gravimeter time associated with a gravity reading is obtained from the clock of the computer attached to the gravimeter. Therefore, the gravimeter is not synchronous with the GPS clock and requires correction. In order to synchronize the two time systems, the time series of the raw gravity reading and vertical aircraft acceleration can be used (Olesen, 2003). Because gravity signals are much smaller than the vertical accelerations of the aircraft in common weather conditions, most raw readings recorded by the gravimeter are those of the vertical accelerations of the aircraft. Thus, the patterns of the raw gravity readings of the gravimeter and vertical acceleration readings of the GPS receiver are very similar. According to this characteristic, the shift between these two time series can be determined using a correlation analysis (Hwang et al., 2006b).

It is necessary to use an along track filter for raw airborne gravity data containing considerable noise due to turbulence. We use a Gaussian filter with a filter width of 150 s to eliminate high-frequency signals. The chosen filter width is a trade-off between noise reduction and gravity signal preservation and is proved to be the optimum width in the latter part of this study.

A description of the software that fulfils many of the requirements summarized above can be found in Shih (2004), Hwang (2005), and Hwang et al. (2006b and 2007b). The procedure for the airborne data processing is summarized in Fig 5-2.
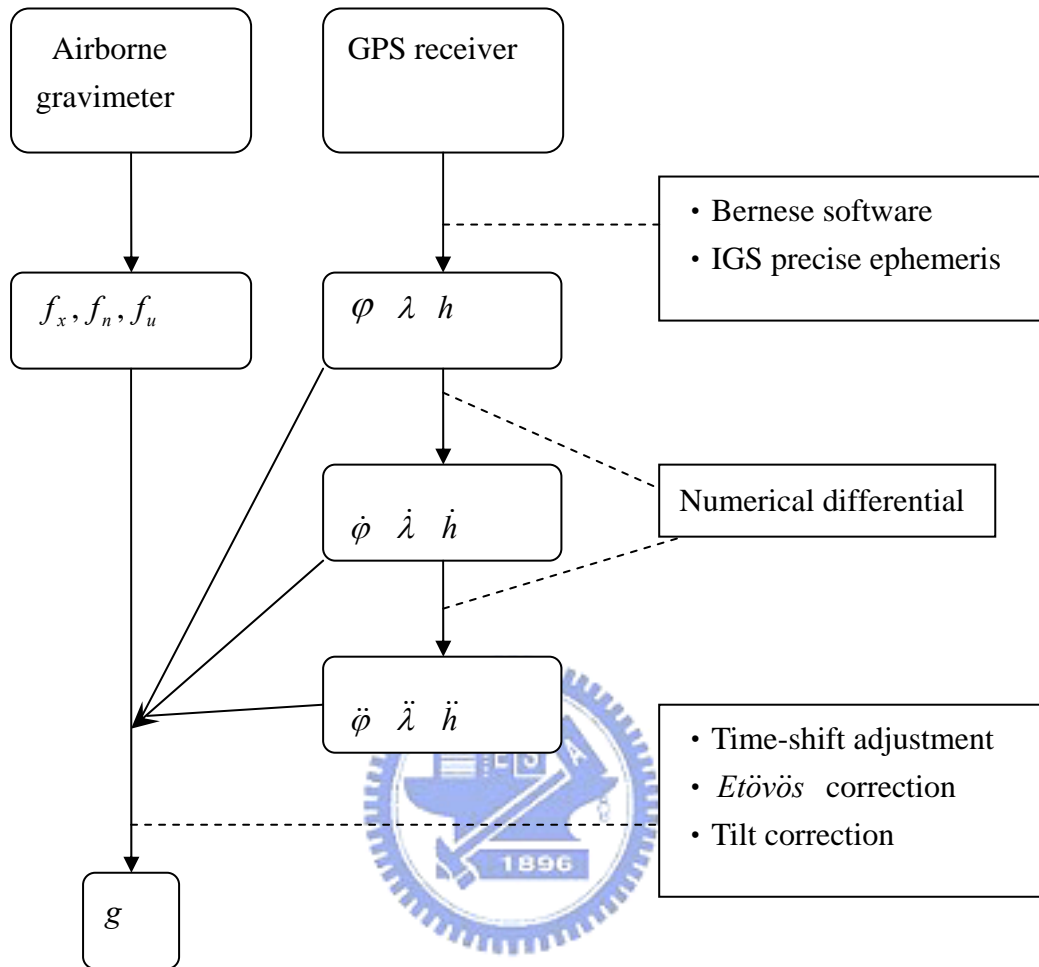
Fig. 5-2 Flow chart of the airborne gravity data process implemented by NCTU. f_x, f_n, and f_u are the three components of the gravimeter measurements. φ, λ, and h represent the latitude, longitude, and ellipsoidal height. $\dot{\varphi}$, $\dot{\lambda}$, $\dot{h}$, and $\ddot{\varphi}$, $\ddot{\lambda}$, $\ddot{h}$ represent the three components of the velocities and accelerations of the aircraft, respectively. g is the output gravity at the flight altitude.

5.4 Results of the Airborne Gravity Survey

Fig 5-3 shows the free-air gravity anomalies at 5156 m using a Gaussian filter with a width of 150 s. The free-air gravity anomalies vary at an altitude of 5156 m over Taiwan and around the sea ranges from approximately –200 mGal over the east trench to 300 mGal over the high mountains (Fig 5-3). The values in the range of ±50 mGal nearly vary over the mild areas. Compared to the surface free-air gravity anomalies (Fig 3-1), the airborne gravity anomalies are much smoother.

5.5 Accuracy Assessment

The quality of the airborne gravity data can be evaluated by using three methods: repeatability analysis, crossover analysis, and comparison with surface gravity data. Repeatability and crossover analyses are used to evaluate the internal accuracy of the airborne data. External accuracy of airborne gravity can be obtained by comparison with surface gravity.

5.5.1 Repeatability Analysis

Repeatability analysis is a basic method to quantify the accuracy of airborne gravity measurements based on the gravity difference between two repeatable flight lines. Parts of Lines 26 and 55 (Fig 5-3) were flown over twice for repeatability analysis. The repeatability standard deviation is chosen as an index of the measurement precision and is calculated as the standard deviation of the differences at all repeat measurement points. Fig 5-4 shows the difference of the standard deviations of repeat lines 26 and 55 on different filter widths. For both the lines, the standard deviation decreases with increasing filter width but becomes flat beyond a certain filter width. At filter widths smaller than 75 s, the standard deviations of Line 26 are higher than those of Line 55; moreover, beyond 75 s, the standard deviation of Line 55 surpasses that of Line 26. The most important factor that the repeat flights of Line 55 lead to the larger repeatability standard deviation is on the GPS positioning. In the first flight over Line 55, some of the estimated aircraft coordinates appear to be erroneous due to changes in the number of visible GPS satellites and disturbances from unknown sources. The iterative Gaussian filter cannot eliminate these errors. As shown in Fig 5-4, at a filter width of 150 s, the repeatability standard deviation of Line 26 is approximately 3 mgal, and it does not decrease significantly as the filter

width increases. Since an increase in the filter width will eliminate detailed gravity information, it appears that a filter width of 150 s is a trade-off between noise reduction and gravity signal preservation.

5.5.2 Crossover Analysis

Crossover analysis can be used to assess the quality of an airborne gravity survey based on the differences of all the intersecting points. One method of crossover analysis is based on quality weighting assignments using a variance criterion (Mittal, 1984, and Wessel, 1989). However, our approach is to solve the bias and drift at each survey line and corrupt the observed gravity values. The basic expression for crossover analysis is

$$\overline{g}_r^q = g_r^q + a^q + b^q t_r^q + e_r^q \tag{5-15}$$

where $\overline{g}_r^q$ represents the observed gravity value at point r along survey line q and $\overline{g}_r^q$ is corrupted by a bias, a drift, and a random error. a^q and b^q represent the bias and the drift, respectively, pertaining to survey line q. e_r^q is the random error and t_r^q is the time at point r relative to the beginning time of line q. g_r^q is the true gravity value. At all intersecting points, the observation equations are given by

$$v_p^{kl} + x_p^{kl} = a^k + b^k t_p^k - a^l - b^l t_p^l \quad, \quad k = 1, \cdots i, l = 1, \cdots m, p = 1, \cdots n \tag{5-16}$$

where x_p^{kl} represents the differenced gravity value at crossover point p pertaining to lines k and l; x_p^{kl} is the residual; $i + m$ and n are the number of survey lines and crossover points, respectively. Eq (5-16) can be expressed by a matrix representation, such that

$$V + L = AX \tag{5-17}$$

where V, L, and X are the vectors containing residuals, observations, and parameters (bias and drift), and A is the design matrix. In order to avoid the rank defect, at least one survey line must be fixed. This line should contain the most stable weather

condition of the flight and GPS positioning result.

Fig 5-5 shows the crossover differences (total 736) and a histogram of these values. Most differences are within ±7 mGal, except for a fewer large ones due to inaccurate GPS data and turbulences. If the large differences exceed 15 mgal, they are considered as outliers and not used for the subsequent analyses. The distribution of crossover differences approximately follows a normal distribution, suggesting that these differences are largely due to random noises. Before and after the bias and drift correction on each flight line, the standard deviations of the differences are 4.92 and 2.88 mgal, respectively. The data quality obtained by crossover analysis is consistent with those of other airborne gravity campaigns conducted in other parts of the world.

5.5.3 Comparison with Surface Gravity Data

In order to assess the external accuracy of the airborne gravity data, surface gravity (land and shipborne gravity) must continue upward to the flight altitude and must be compared with airborne gravity measurements. According to Eq (2-37), the UWC of the gravity field from plane z = 0 to z = 5156 in the wave-number domain is formulated by

$$G_{5156}(f_x, \ f_y) = e^{-2\pi h f_r} G_0(f_x, \ f_y) \tag{5-18}$$
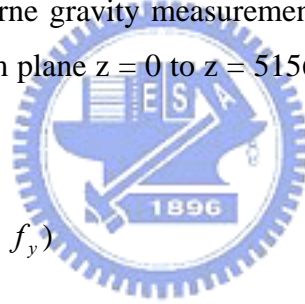
where $G_{5156}(f_x, \ f_y)$ and $G_0(f_x, \ f_y)$ denote the gravity fields at elevations of 5156 m and 0 m, respectively. h equals 5156 m. Because Eq (5-18) is based on the FFT technique, the surface gravity observations need to be interpolated into regular grids before comparison. This method of interpolation is based on LSC due to the unequal data qualities of land and shipborne data.

In the FFT process of DWC and UWC, 100% zero-padding must be considered to eliminate cyclic convolution errors and edge effects. Fig 5-6 shows 100% zero-padding grids used in DWC and UWC. All grids in Fig 5-6, except gravity grids, are set to 0. The spectrum of UWC obtained in this study is shown in Fig 5-7. The spectrum response decreases rapidly as the spectrum frequency rapidly increases. In order to reduce the topographic effect, we use Bouguer anomalies as the gravity field for FFT UWC. The Bouguer correction applied to the airborne data was calculated by Gaussian quadrature (Hwang et al., 2007b) with 15 km and 100 km inner-zone and

outer-zone radii. Fig 5-8(a) shows the airborne gravimetry-derived Bouguer anomalies at an elevation of 5156 m. In comparison to airborne free-air anomalies (Fig 5-3), the values over mountains or plains are both small but are almost the same at sea. Figs 5-8(b) and (c) show the surface Bouguer anomalies gridded from the surface gravity data by LSC and its upward-continued Bouguer anomalies implemented by FFT. The surface data used in Fig 5-8(b) are those of land and shipborne gravity (Figs 3-1(a) and (b)). On comparing Figs 5-8(c) and (b), the upward-continued field at 5156 m becomes much smoother than that at 0 m. Fig 5-8(d) shows the differences between the surface-upward-continued (Fig 5-8(c)) and airborne (Fig 5-8(a)) Bouguer anomalies, both at the locations of the airborne data. Most of the differences in Fig 5-8(d) are very small; however, some large differences, reaching approximately 50 mgal, occur over high mountains. The standard deviation of the differences is 11.2 mgal. These large differences can be attributed to (1) errors in airborne gravity measurements, (2) data density and quality of surface gravity data, (3) large gravity gradients at areas with rough gravity fields, and (4) possible computation error in UWC. It is observed that the gravity fields over the Central Range (low surface data density) and the ocean trench to the east of Taiwan (high surface data density) are equally rough; however, large differences are observed only over the Central Range. This indicates that the differences in Fig 5-8(d) are largely due to surface data density rather than the errors in the airborne gravity measurements.

In order to compute a precise geoid model, airborne data can be used in combination with land, shipborne, and altimetry data. This study is described in chapter 6.
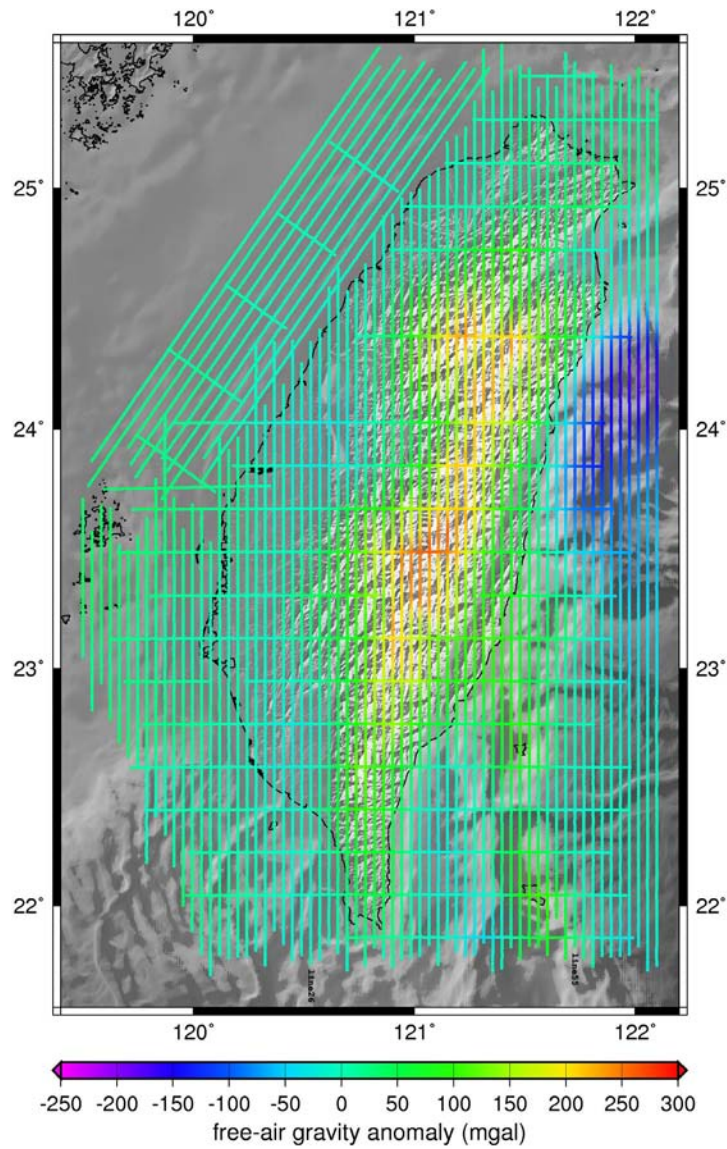
Fig. 5-3 Gravity anomalies at the average flight altitude of 5156 m.
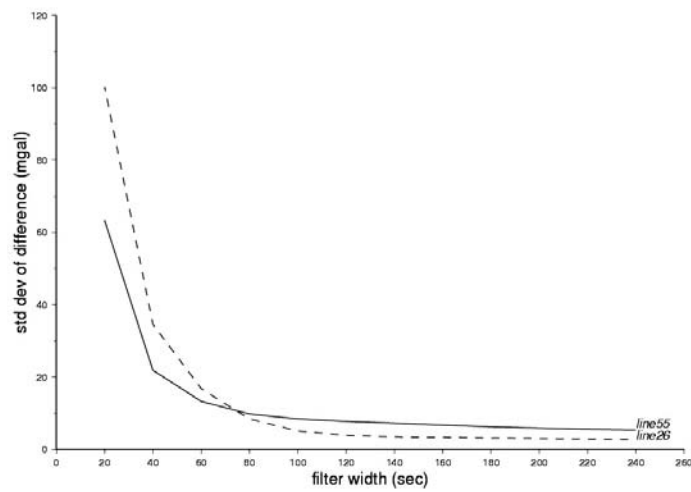
Fig. 5-4 Standard deviation of the differences in the gravity anomalies obtained from two repeat flights (Hwang et al., 2007b).
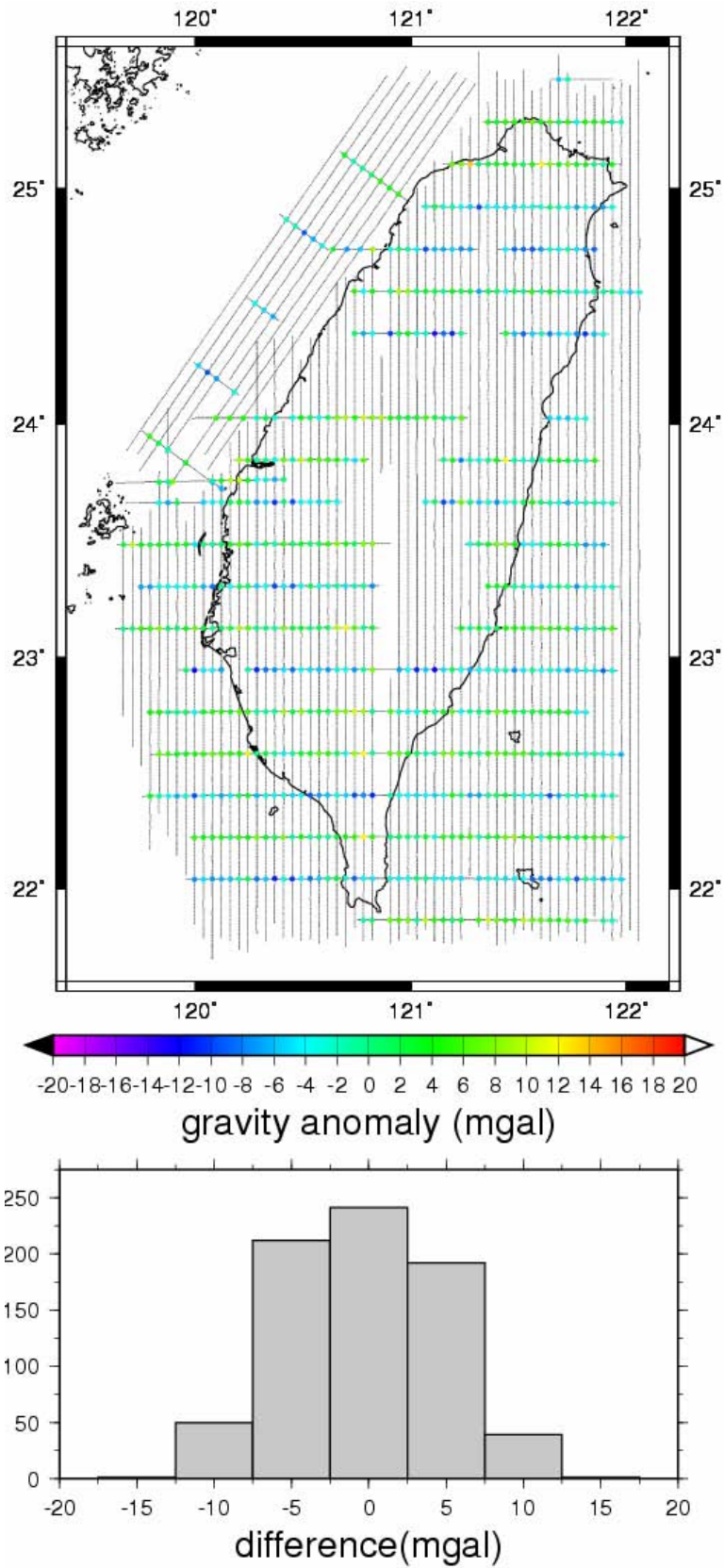
Fig. 5-5 Distribution and histogram of the crossover differences of gravity anomalies (Hwang et al., 2007b).
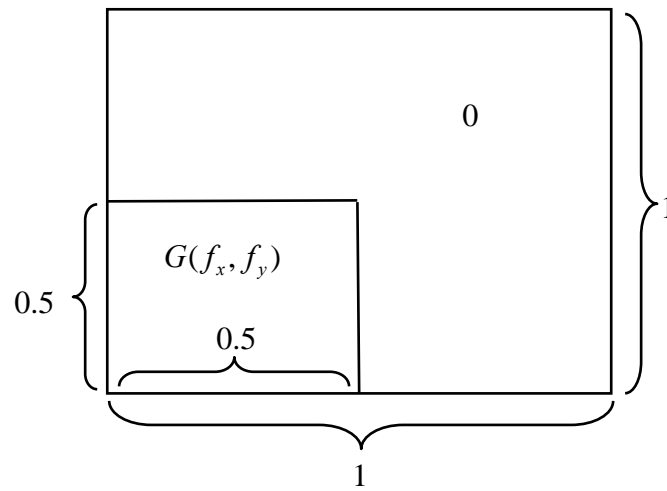
Fig. 5-6 Zero-padding (100%) of the used gravity field $G(f_x, f_y)$ in UWC and DWC.
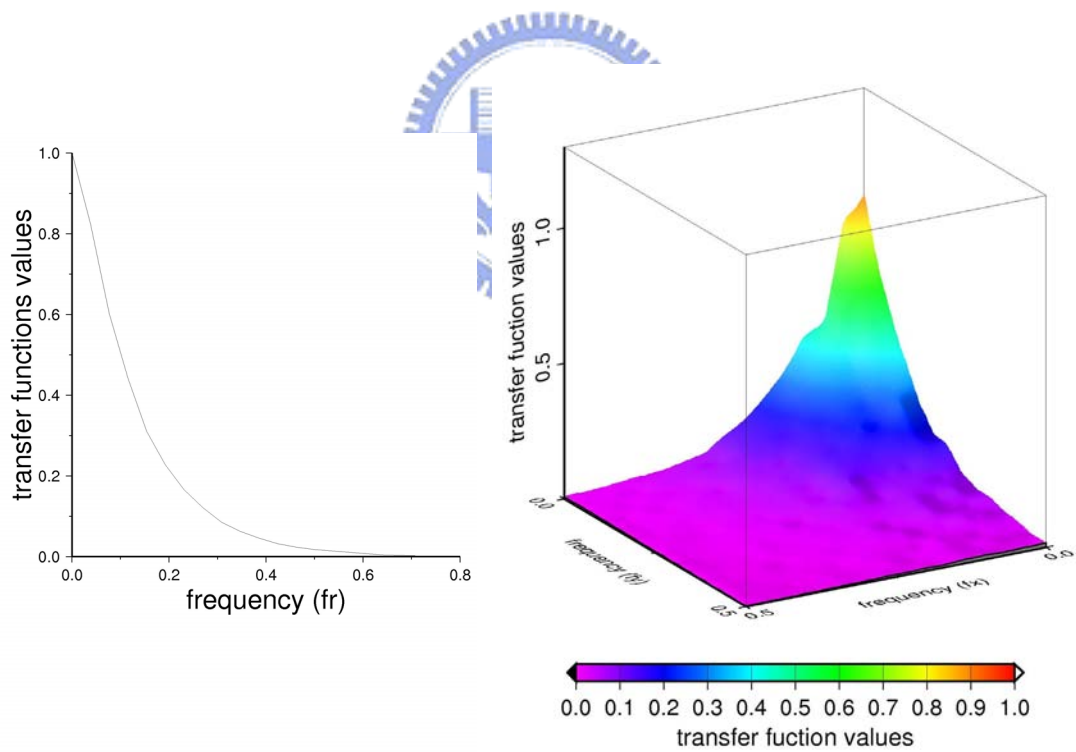
Fig. 5-7 The 1D (left) and 2D transfer functions of UWC; $f_r = \sqrt{f_x^2 + f_y^2}$. The unit of frequency along the x and y directions is the same as that shown in Fig 5-6.
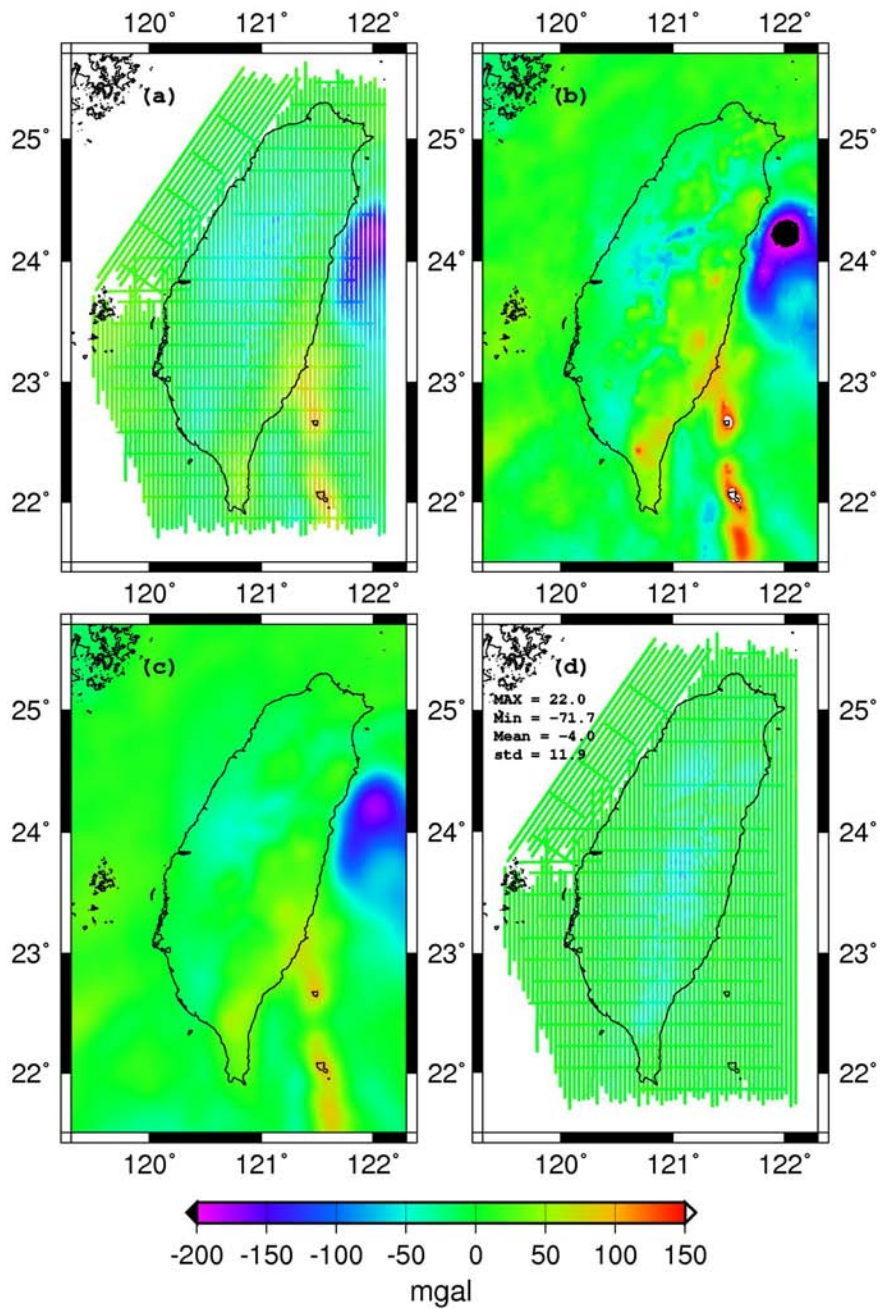
Fig. 5-8 (a) Bouguer anomalies at an altitude of 5156 m, (b) Bouguer anomalies of surface gravity data on the grid (from land and shipborne data), (c) Surface-upward-continued Bouguer anomalies (at 5156 m), (d) differences between surface (upward-continued) and airborne Bouguer anomalies.

71

Chapter 6

Geoid Modeling Using Combined Airborne and Surface Gravity Data

6.1 Introduction

In this study, airborne gravity anomalies, combined with land, shipborne, and altimeter-derived gravity anomalies, are used for the determination of the gravimetric geoid. The strategy is also based on the RCR procedure by LSC. Two different methods that use airborne gravity data for geoid determination are introduced. The first method involves first performing the DWC to sea level, and then merging it with the surface gravity to compute the geoid. The DWC of this method can be performed by FFT or LSC. The second method is direct use for geoid modeling, whose DWC can be performed only by LSC.

6.2 Continuation to Sea Level and Merging with Surface Gravity

The airborne gravity data would first be downward continued to sea level. Then, all the gravity data, including land, shipborne, altimeter-derived, and downward-continued airborne data, would be used to compute the residual geoid. As mentioned in chapter 2, FFT is an efficient technique to perform the DWC. UWC using FFT has been previously performed for a comparison of airborne and surface gravity data. According to the principle of DWC by FFT (Eq (2-39)), a low-pass filter must be used to eliminate noise. In this study, we adopt two common low-pass filters—Gaussian and Wiener filters—to smooth the downward-continued gravity signals. LSC is also used in this DWC.

6.2.1 DWC by FFT with Gaussian Filter

The Gaussian filter has a number of desirable properties that make it the most commonly used smoothing filter. For example, the Gaussian filter is the only low-pass filter that has good localization properties in both the spatial and frequency domains. Second, the Gaussian filter is decomposable and rotationally invariant. Moreover, the Gaussian filter is closely related to the technique of multi-resolution or multi-scale processing because it can be employed to create input data with varying resolutions

from coarse to fine. The transfer function corresponding to Gaussian smoothing (for equally spaced and weighted measurements) is formulated as (Attila, 1984)

$$S_{Gau} = e^{k^2 f_r^2}$$
(6-1)

where k is the semi-bandwidth of the Gaussian function. The degree of smoothing is determined by k. When k increases, the degree of smoothing increases. Thus, the smoothed downward-continued gravity using the Gaussian filter is expressed as

$$g_{down}(f_r) = g(f_r)e^{2\pi h f_r - (k f_r)^2}$$
(6-2)

where $g(f_r)$ is the original gravity field, and $g_{down}(f_r)$ is the new field after DWC.

6.2.2 DWC by FFT with Wiener Filter

The characteristic of the Wiener filter is that it converts a specified input into a specified output such that the sum of the squares of the differences between the desired output and actual output is minimum (Gunn, 1972). The theory of the Wiener filter was originally developed by Wiener (1949). The Wiener filter is often used to reduce the noise in input data and is applied to DWC and other techniques used in geophysical research. In the frequency domain, the Wiener filter can be expressed as (Forsberg and Skourup, 2005)

$$S_{Wei} = \frac{1}{1 + (k f_r)^4}$$
(6-3)

where parameter k also determines the degree of smoothing of the Wiener filter. Therefore, the smoothed downward-continued gravity using the Wiener filter is given by

$$g_{down}(f_r) = g(f_r)\frac{e^{2\pi h f_r}}{1 + (k f_r)^4}$$
(6-4)

No matter which filter is used, Gaussian or Wiener, parameter k affects the result of the downward-continued data. Thus, the choice of k values must be considered rigorously and should represent an appropriate compromise between noise reduction and signal detail.

6.2.3 DWC by LSC

In this subsection, airborne gravity anomalies are first downward continued to the sea level by LSC. Second, the downward-continued gravity anomalies are merged with other surface gravity anomalies for geoid modeling by LSC again. This method may be categorized as indirect use for geoid determination by LSC. The residual gravity anomalies of the downward-continued airborne data can be represented as

$$\Delta g_{res}^{air-down} = \left(C_{\Delta g^{sur}\Delta g^{air}} \right) \left(C_{\Delta g^{air}} + D_{\Delta g^{air}} \right)^{-1} \left(\Delta g_{res}^{air} \right) \tag{6-5}$$

where $\Delta g_{res}^{air-down}$ represents the downward-continued residual anomalies; Δg_{res}^{air}, the input airborne residual anomalies; $C_{\Delta g^{sur}\Delta g^{air}}$ and $C_{\Delta g^{air}}$, the covariance matrices for surface gravity anomaly–airborne gravity anomaly and airborne gravity anomaly–airborne gravity anomaly, respectively; and $D_{g^{air}}$, the variance of the noise of the input air gravity data. Then, the downward-continued data and surface gravity data can be combined for geoid modeling by Eq (2-12).

6.3 Direct Use for Geoid Modeling

An attempt in this study has been made to perform DWC of airborne gravity and determination of residual geoid simultaneously. Compared to the indirect method mentioned in 6.2.3, this method is a direct geoid determination method. In this study, the corresponding equation for LSC computation is given by

$$N_{res} = \begin{pmatrix} C_{ng^{sur}} & C_{ng^{air}} \end{pmatrix} \begin{pmatrix} C_{\Delta g^{sur}} + D_{\Delta g^{sur}} & C_{\Delta g^{sur}\Delta g^{air}} \\ C_{\Delta g^{air}\Delta g^{sur}} & C_{\Delta g^{air}} + D_{\Delta g^{air}} \end{pmatrix}^{-1} \begin{pmatrix} \Delta g_{res}^{sur} \\ \Delta g_{res}^{air} \end{pmatrix} \tag{6-6}$$

where $C_{n\Delta g^{sur}}$, $C_{\Delta g^{sur}}$, $C_{n\Delta g^{air}}$, $C_{\Delta g^{air}\Delta g^{sur}}$, $C_{\Delta g^{sur}\Delta g^{air}}$, and $C_{\Delta g^{air}}$ are the covariance matrices for geoid–surface gravity anomaly, surface gravity anomaly–surface gravity anomaly, geoid–airborne gravity anomaly, airborne gravity anomaly–surface gravity anomaly, surface gravity anomaly–airborne gravity anomaly, and airborne gravity anomaly–airborne gravity anomaly, respectively. $D_{\Delta g^{sur}}$ and $D_{\Delta g^{air}}$ are the variances of the noises of the input surface and airborne gravity data.

The direct use for geoid modeling is a more efficient process. However, the disadvantage of this method is that the downward-continued gravity data cannot be first evaluated by surface gravity data and the outliers cannot be removed before geoid computation.

6.4 Design of Experiments

An interesting point to note is that a free-air or Bouguer anomaly field performs better in DWC by FFT and agrees better in geoid modeling. Hwang et al. (2007b) used free-air gravity anomalies for this application. In this study, we use Bouguer anomalies in order to reduce the influence of the topographic effect. A comparison of the two results for geoid modeling is discussed in section 6.6.

The computation of the Bouguer correction for the airborne data is also based on the Gaussian quadrature mentioned in chapter 4. After performing DWC on the airborne Bouguer anomalies, we must restore the topographic effect in order to acquire the free-air anomalies, and then remove the long- and short-wavelength effects to obtain the residual gravity anomalies. After that, the data are combined with the surface and altimeter-derived residual gravity anomalies to calculate the residual geoid by LSC.

Downward-continued gravity anomalies are stored in a $2' \times 2'$ grid, both for the FFT and LSC processes, which is the same as that with the KMS02 gravity data. In order to avoid data points located in the same grid, the grids of the KMS02 and downward-continued gravity data are staggered in 1-min spaces. Fig 6-1(a) shows the entire gravity data set used in this geoid modeling. This data set includes land (black), shipborne (black), altimetry (blue), and downward-continued airborne gravity (red) data. Fig 6-1(b) shows a zoomed-in view of the black rectangular area in Fig 6-1(a). There is no data overlaying due to the staggered regular grids of the altimeter-derived and downward-continued airborne gravity data.

DWC by LSC is also based on the combination of the EIGEN-GL04C geopotential model and Tscherning-Rapp degree variance model 4. The covariances used in this study are shown in Fig 6-2. However, this anomaly degree model is for free-air anomalies not Bouguer anomalies. Therefore, we use free-air anomalies for the LSC DWC. Furthermore, the noises for different data types have to be determined both in indirect and direct geoid determination by LSC. We assign 0.1, 1.0, 5.0, and 3.0 mgal data noise to land, shipborne, altimeter-derived, and airborne gravity anomalies, respectively.

The procedure for geoid modeling in this study is shown in Fig 6-3. The discrepancy between the geoid models of the five cases is solely governed by the DWC methods of the airborne gravity data. In case A, there are no airborne data used for the geoid computation. The DWCs in cases B and C are performed by FFT with Gaussian and Wiener low-pass filters, respectively. In cases D and E, airborne gravity data are processed by LSC DWC. Airborne gravity data of cases D is continued downward to sea level first. However, cases E performs DWC of airborne gravity data and determination of the geoid simultaneously. Cases D and E belong to the types of indirect and direct geoid determination, respectively.
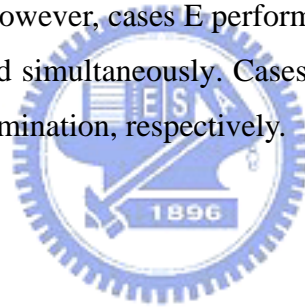
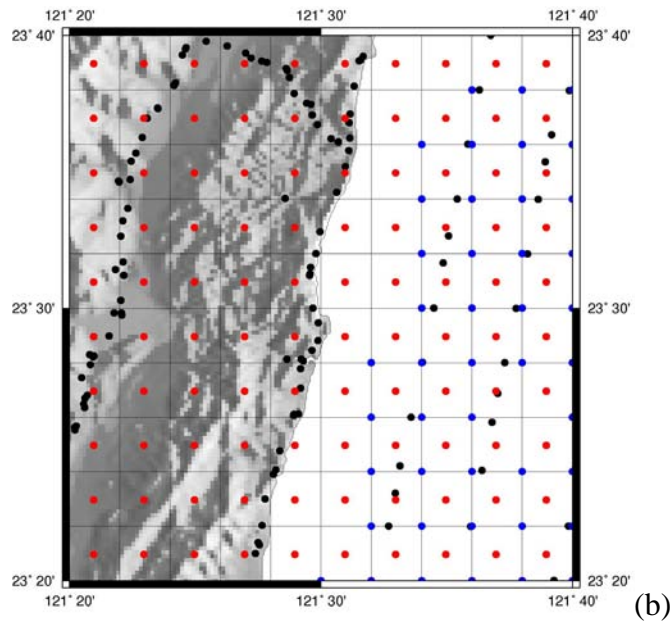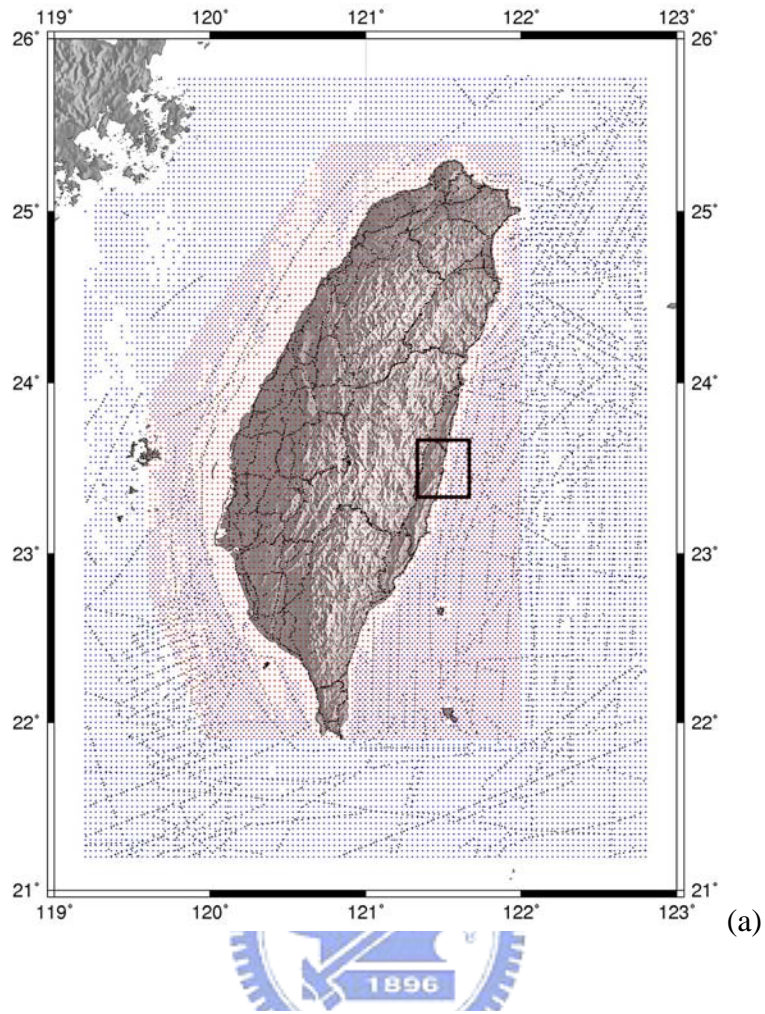**Fig. 6-1** (a) All the input gravity data for geoid computation. (b) Zoomed-in view of the black rectangular area in (a). Black, blue, and red points denote land\shipborne, altimeter-derived and downward-continued airborne data, respectively.
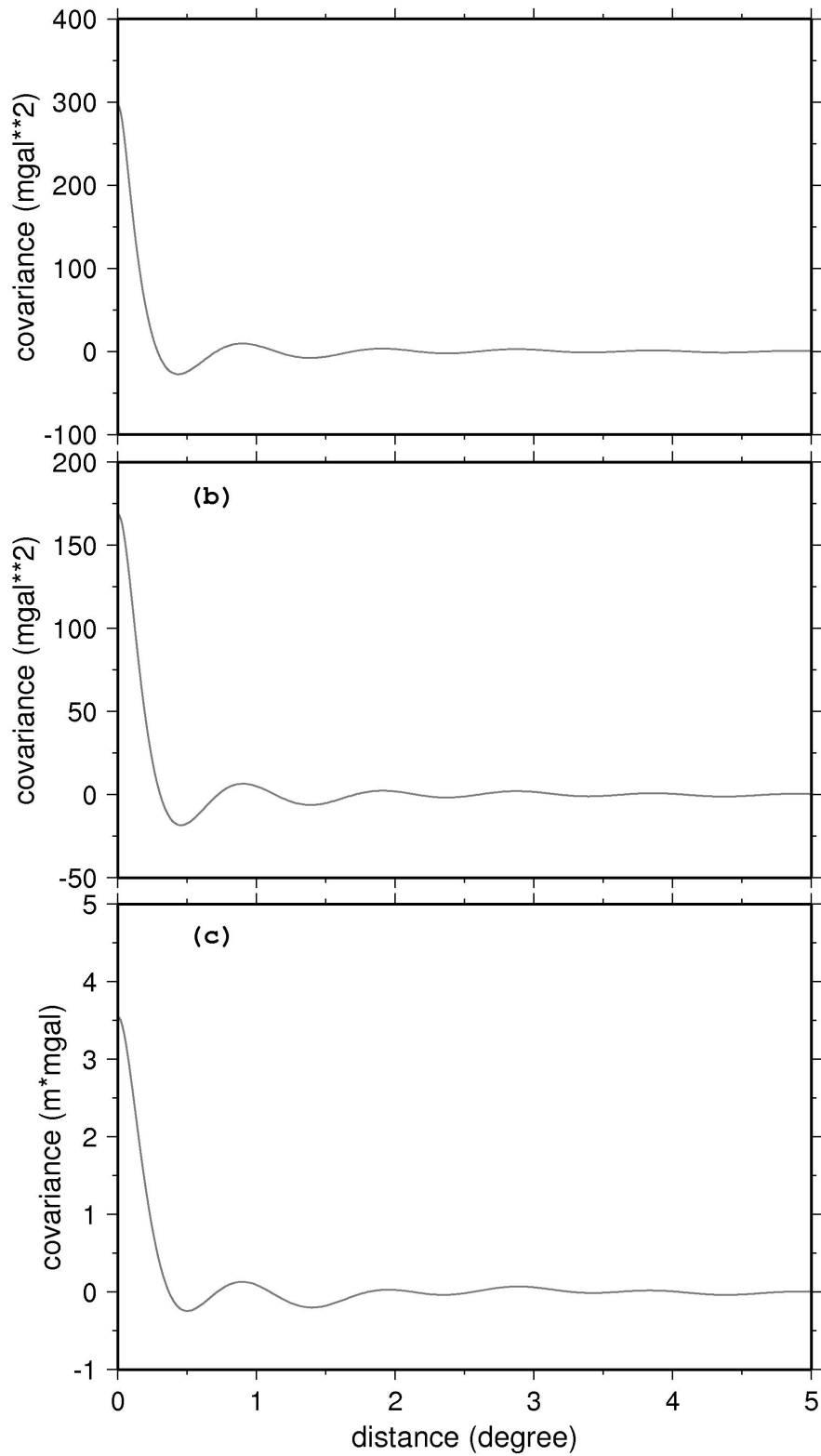
Fig. 6-2 Covariances: (a) Surface gravity–airborne gravity covariance matrix. (b) Airborne gravity–airborne gravity covariance matrix. (c) Airborne gravity–geoid covariance matrix.
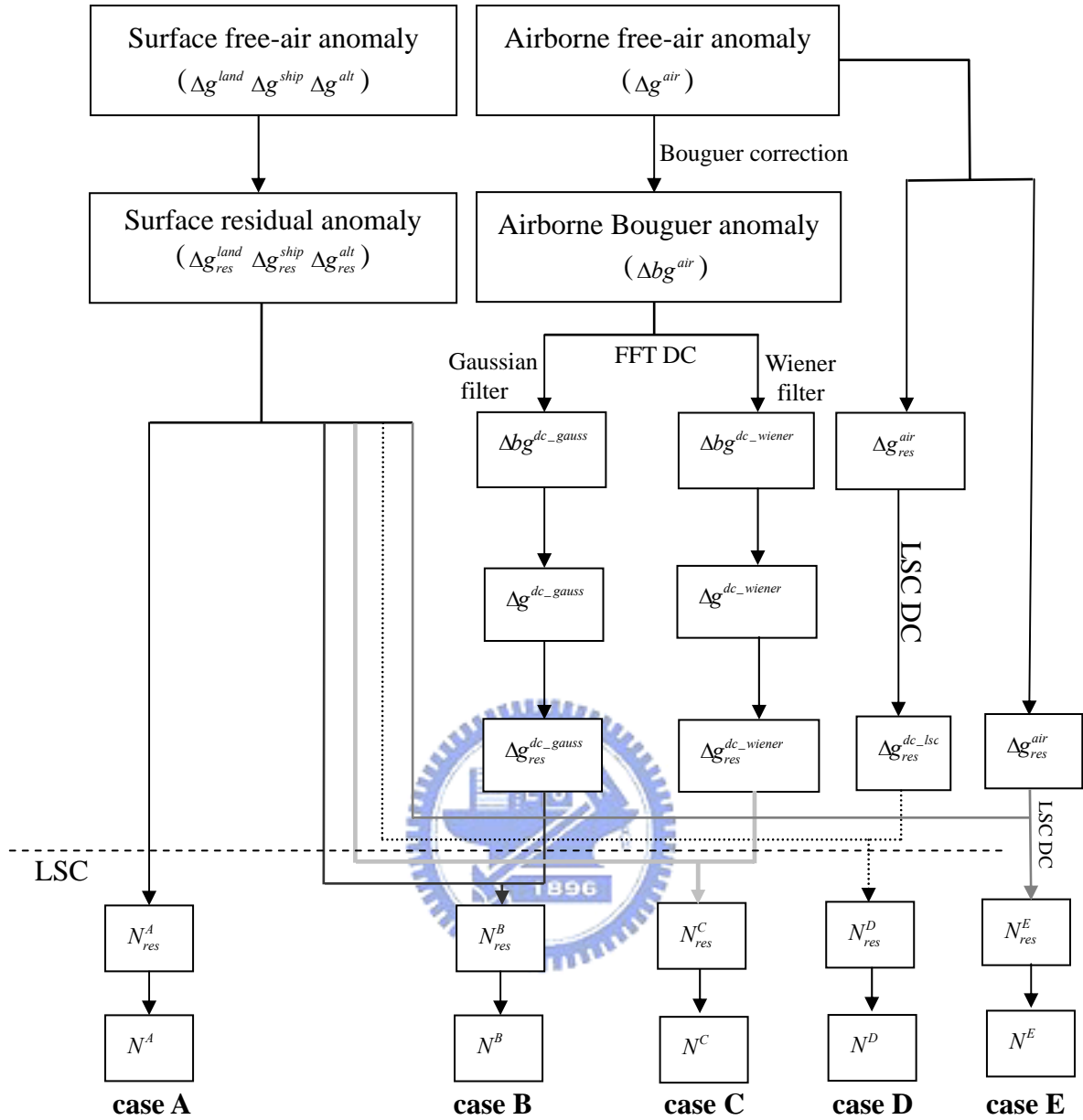
Fig. 6-3 Flow chart of geoid modeling. Case A excludes airborne data. The downward-continuation methods of cases B and C are based on FFT by Gaussian and Wiener filters, respectively. Cases D and E use LSC DWCs of the indirect and direct types, respectively, for geoid determination. Δbg^{dc_gauss}, Δg^{dc_gauss}, and $\Delta g_{res}^{dc\_gauss}$ denote downward-continued Bouguer, free-air, and residual anomalies smoothed by the Gaussian filter. Δbg^{dc_wiener}, Δg^{dc_wiener}, and $\Delta g_{res}^{dc\_wiener}$ denote those smoothed by the Wiener filter. $\Delta g_{res}^{dc\_lsc}$ represents the downward-continued residual anomalies by LSC. "FFT DC" and "LSC DC" mean FFT and LSC DWCs, respectively.

6.5 Evaluating Downward-Continued Airborne Gravity Data

6.5.1 Results of DWC by FFT

Fig 6-4 shows the spectrum of the DWC. Compared to UWC (Fig 5-7), the spectrum response of the DWC increases rapidly with increasing frequency. For the DWCs in cases B and C, the ideal values for parameter k must be estimated first. We use k = 5, 10, 15, 20, 25, and 30 in this work and attempt to identify the suitable k value. Figs 6-5 and 6-6 present 1D and 2D frequency responses of the Gaussian filter at k = 5, 10, 15, 20, 25, and 30. Those of the Wiener filter at k = 5, 10, 15, 20, 25, and 30 are shown in Figs 6-9 and 6-10. If parameter k becomes larger, the responses decay faster. The decreasing trend of the frequency responses of the two low-pass filters can diminish the increasing responses of the DWC (Fig 6-4). Figs 6-7 and 6-11 present the downward-continued Bouguer anomalies by the Gaussian and Wiener filters, respectively, for the conditions of k = 5, 10, 15, 20, 25, and 30. As k increases, the downward-continued Bouguer anomalies become smoother.

In order to determine which value of k is the best choice, some selected surface gravity data with highly accurate Bouguer anomalies are used. Figs 6-8 and 6-12 show the Bouguer anomaly differences between the surface and downward-continued data by the Gaussian and Wiener filters individually. The statistics of the differences are summarized in Table 6-1. In the result by the Gaussian filter, the standard deviations of the differences are 11.4, 8.5, 8.7, 9.3, 10.2, and 11.1 mgal at k = 5, 10, 15, 20, 25, and 30, respectively. It is obvious that k = 10 provides the best result because it has the smallest standard deviation. For k > 10, the standard deviations become increasingly larger as k increases. Besides the standard deviation, k = 10 also exhibits excellent maximum, minimum, and mean values, as compared to the other k values. In the result by the Wiener filter, the standard deviations of the differences are 13.5, 8.5, 8.3, 8.6, 9.1, and 9.8 mgal at k = 5, 10, 15, 20, 25, and 30, respectively. Obviously, k = 15 is the best selection, again, due to the smallest standard deviation. The differences in the cases of both the Gaussian and Wiener filters are not correlated with topography in this study.

In brief, k = 10 for the Gaussian filter and 15 for the Wiener filter are the ideal values in order to obtain more accurate results from DWC. Thus, a Gaussian filter with k = 10 and a Wiener filter with k =15 are the best choices of all.

6.5.2 Results of DWC by LSC

Fig 6-13 shows some results of the airborne data by LSC DWC, which is an indirect-use type method of geoid determination. Fig 6-13(a) presents the free-air anomalies at 5156 m. The RTM-derived anomalies at 5156 m performed by Gaussian quadrature are shown in Fig 6-13(b). Fig 6-13(c) expresses the residual gravity anomalies at 5156 m from which the EIGEEN-GL04C-derived and RTM-derived anomalies have been removed. Fig 6-13(d) indicates the downward-continued residual gravity anomalies. The differences between the residual gravity anomalies of the selected surface and downward-continued data are shown in Fig 6-14. The statistics of the differences are summarized in Table 6-2. In Fig 6-14, some large differences are found over the Central Range, reaching approximately 70 mgal, but most of the differences, even over this highly mountainous area, are not large. The standard deviation of these differences is 16.0 mgal.

Table 6-1 Statistics of the differences between surface gravity anomalies and DWC (FFT) gravity anomalies.

Filter	K parameter	Max	Min	Mean	Std dev
Gaussian filter	5	131.0	–116.2	-0.4	11.4
	10	50.5	–35.8	-0.3	8.5
	15	55.6	–39.3	-0.1	8.7
	20	62.5	–43.9	0.1	9.3
	25	69.4	–48.9	0.3	10.2
	30	75.8	–53.7	0.4	11.1
Wiener filter	5	177.2	–159.1	-0.4	13.5
	10	50.3	–34.1	-0.4	8.5
	15	50.9	–33.7	-0.3	8.3
	20	53.3	–36.7	-0.1	8.6
	25	59.9	–41.4	0.2	9.1
	30	66.2	–47.1	0.4	9.8

Table 6-2 Statistics of the differences between surface gravity anomalies and DWC (LSC) gravity anomalies.

Max	Min	Mean	Std dev
68.6	–67.2	–0.1	16.0

6.6 Results of Geoid Modeling

Fig 6-15 presents the geoid models of cases A to E. Fig 6-16 shows the differences between the geoid models of cases A and B, cases A and C, cases A and D, and cases A and E. The largest differences are located over mountainous and offshore areas and reach approximately ±40 cm. The reason why such large differences occur over high mountains is the contribution of airborne gravity data. By comparing Figs 6-16(a) and (b), it is apparent that the geoid surfaces of cases A and B are very similar. This implies that for geoid modeling, the distinction between the use of Gaussian or Wieners filters in FFT DWC is small. In Fig 6-16(c), there are two obvious local lows, as in (a) and (b), over central and south Taiwan. However, the geoid surface still has a difference of 20 cm as compared to (a) and (b) over some areas. The differences in Fig 6-16(d) are considerably distinct from those in (a), (b), and (c). The differences between the geoid surfaces of case E and those of the other cases reach 40 cm over some areas. This implies that there is some doubt regarding whether direct geoid determination by LSC is feasible.

In order to evaluate the external accuracy of the five geoid models, four GPS/leveling routes are used. Fig 6-17 presents the differences between the observed and modeled geoidal heights (cases A~E) along the four GPS/leveling routes. The statistics of the differences are summarized in Table 6-3. Compared to case A, the geoid accuracies in cases B~D have obvious improvements along the south route, but lesser improvements along the center route. On the contrary, the geoid accuracy in case E improves along the center route, but is degraded along the south route instead. On the other hand, although the geoid surface of case E greatly differs from those of the other cases, the standard deviation in Table 6-3 still indicates a good geoid accuracy in case E, especially along the center route.

Besides the five cases, the geoid developed by Hwang (2005) is also evaluated along the four GPS/leveling routes, and the statistics are also summarized in Table 6-3.

The airborne data used in this geoid model are downward continued by FFT and using free-air gravity anomalies. The chosen filter is a Gaussian filter in the space domain with a 15-km filter width realized by using the GMT package. This filter width was proven to be the best in Hwang (2005). Compared to cases B and C, which use Bouguer anomalies for DWC, the geoid accuracy of Hwang (2005) is worse than that of the two cases. According to the comparison, Bouguer anomalies of the gravity type are recommended for FFT DWC.

The standard errors in the geoid models can be determined by Eq (2-13). Such errors represent the internal accuracies of the geoid models. However, the external accuracy, which is evaluated by four GPS/leveling routes, does not agree with the internal accuracy. The internal errors should be adjusted to the external errors. According to Table 6-3, the external accuracy of the geoid models in the east route is quite uniform (range: 5~8 cm), having an average standard deviation 6 cm. Thus, the estimated standard errors in the geoid models can be adjusted to fit the external geoid accuracy at the east GPS/leveling points. Table 6-4 shows the average standard geoid errors by Eq (2-13) in the east GPS/leveling points. The standard errors of the five geoid models are 0.084, 0.128, 0.108, 0.171, 0.054 m, respectively. Compared to external accuracy, they are obviously different. Therefore, we use GMT package to adjust the geoid errors to about 6 cm at the east GPS/leveling points. After the adjustment, the absolute geoid errors are changed but the relative errors remain the same. Fig 6-18 shows the adjusted geoid errors. In Fig 6-18, it is obvious that the geoid models using airborne gravity data (case B~E) have smaller errors than the case of not using such data (case A). In Fig 6-18(a), the geoid errors can reach 20 cm over high mountains. However, most errors in Fig 6-18(b)~(e) are reduced and are below 10 cm.

Table 6-3 Statistics of differences (in meter) between the observed and modeled geoidal heights at four leveling routes

Case	Leveling route	Max	Min	Mean	Std dev
Case A	north	–0.036	–0.159	–0.096	0.040
	east	–0.229	–0.404	–0.316	0.065
	center	–0.193	–0.604	–0.353	0.154
	south	–0.244	–0.504	–0.348	0.073
Case B	north	–0.065	–0.152	–0.116	0.028
	east	–0.192	–0.379	–0.276	0.054
	center	–0.124	–0.545	–0.280	0.166
	south	–0.280	–0.370	–0.333	0.034
Case C	north	–0.064	–0.152	–0.116	0.028
	east	–0.193	–0.388	–0.281	0.056
	center	–0.123	–0.545	–0.279	0.167
	south	–0.279	–0.369	–0.331	0.034
Case D	north	–0.047	–0.282	–0.159	0.078
	east	–0.084	–0.314	–0.254	0.069
	center	–0.110	–0.389	–0.299	0.081
	south	–0.105	–0.592	–0.440	0.144
Case E	north	0.006	–0.072	–0.037	0.022
	east	0.059	–0.193	–0.029	0.084
	center	0.105	–0.249	0.131	0.114
	south	0.011	–0.401	–0.254	0.143
Hwang (2005)	north	0.138	–0.230	–0.063	0.134
	east	–0.235	–0.533	–0.397	0.079
	center	–0.297	–0.786	–0.559	0.158
	south	–0.036	–0.455	–0.234	0.159

Table 6-4 The original average geoid errors (in meter) in the east route.

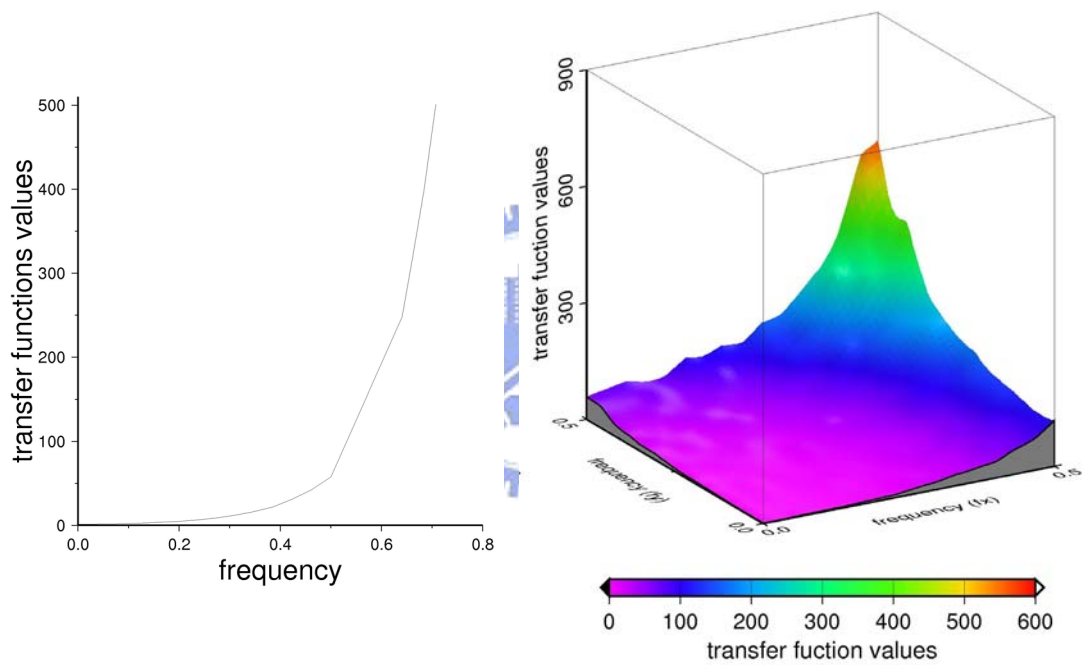| Case	The average geoid errors
Case A	0.084
Case B	0.128
Case C	0.108
Case D	0.171
Case E	0.054

Fig. 6-4 Transfer functions for 1-D (left-hand-side) and 2-D cases of DWC; $f_r = \sqrt{f_x^2 + f_y^2}$. The unit of frequency along the x and y directions is the same as that shown in Fig 5-6.
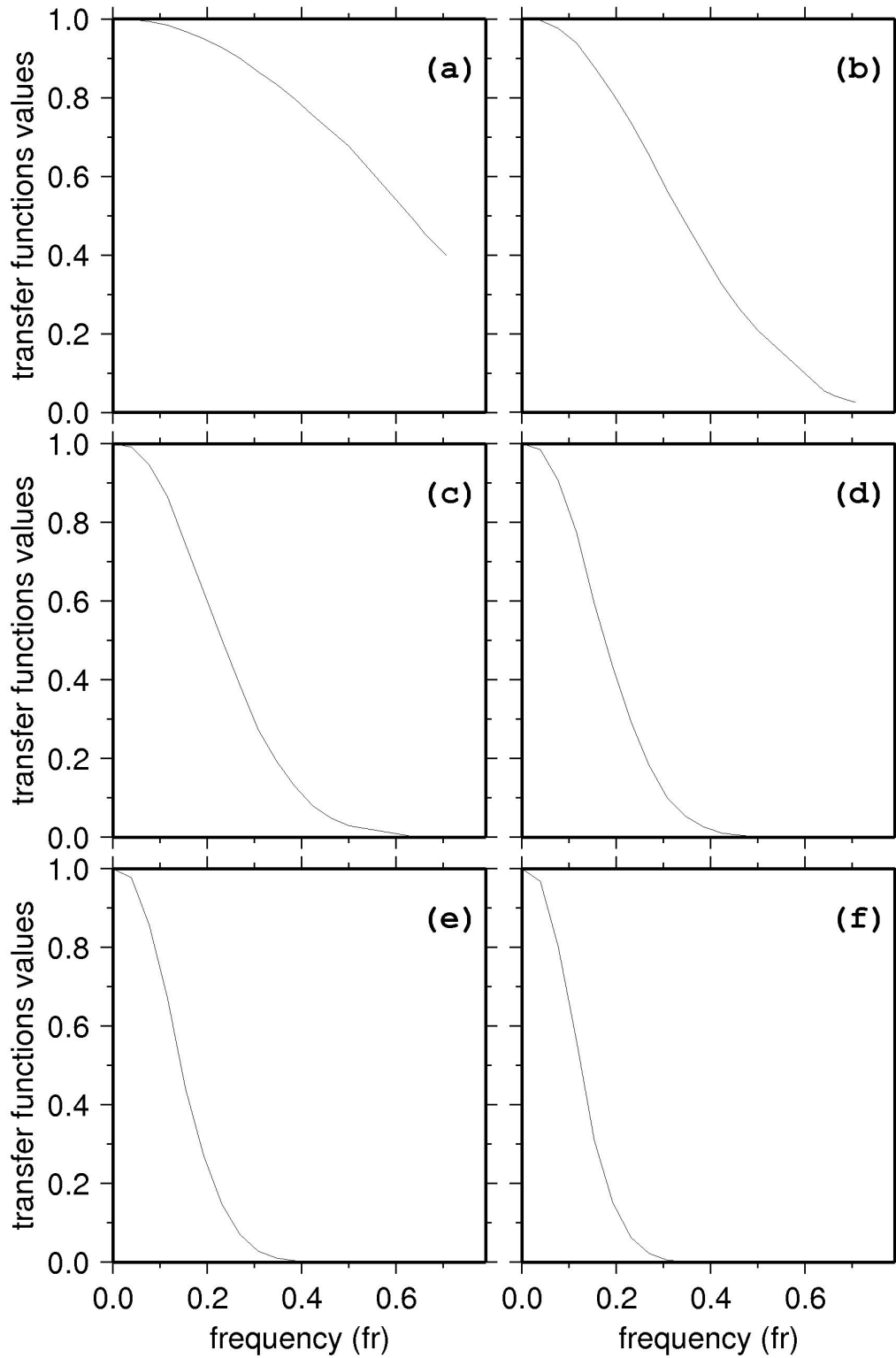
Fig. 6-5 1D frequency response of Gaussian filter. (a) $k = 5$ (b) $k = 10$ (c) $k = 15$ (d) $k = 20$ (e) $k = 25$ (f) $k = 30$.
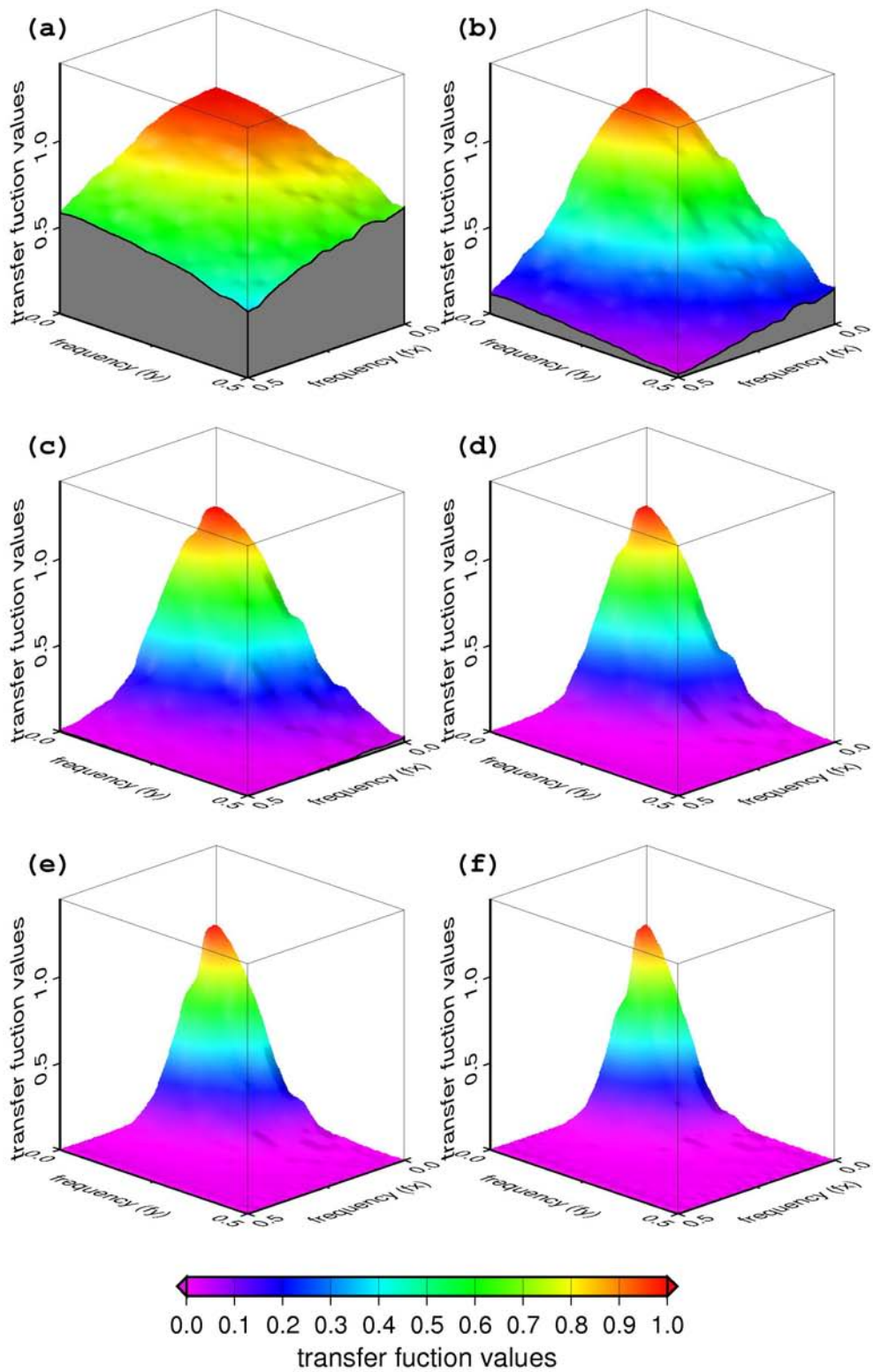
Fig. 6-6 2D frequency response of Gaussian filter. (a) $k = 5$ (b) $k = 10$ (c) $k = 15$ (d) $k = 20$ (e) $k = 25$ (f) $k = 30$.

Fig. 6-7 Downward-continued Bouguer anomalies by Gaussian filter. (a) $k = 5$ (b) $k = 10$ (c) $k = 15$ (d) $k = 20$ (e) $k = 25$ (f) $k = 30$.

Fig. 6-8 Differences between the Bouguer anomalies of the surface and downward-continued airborne data by Gaussian filter. (a) $k = 5$ (b) $k = 10$ (c) $k = 15$ (d) $k = 20$ (e) $k = 25$ (f) $k = 30$.
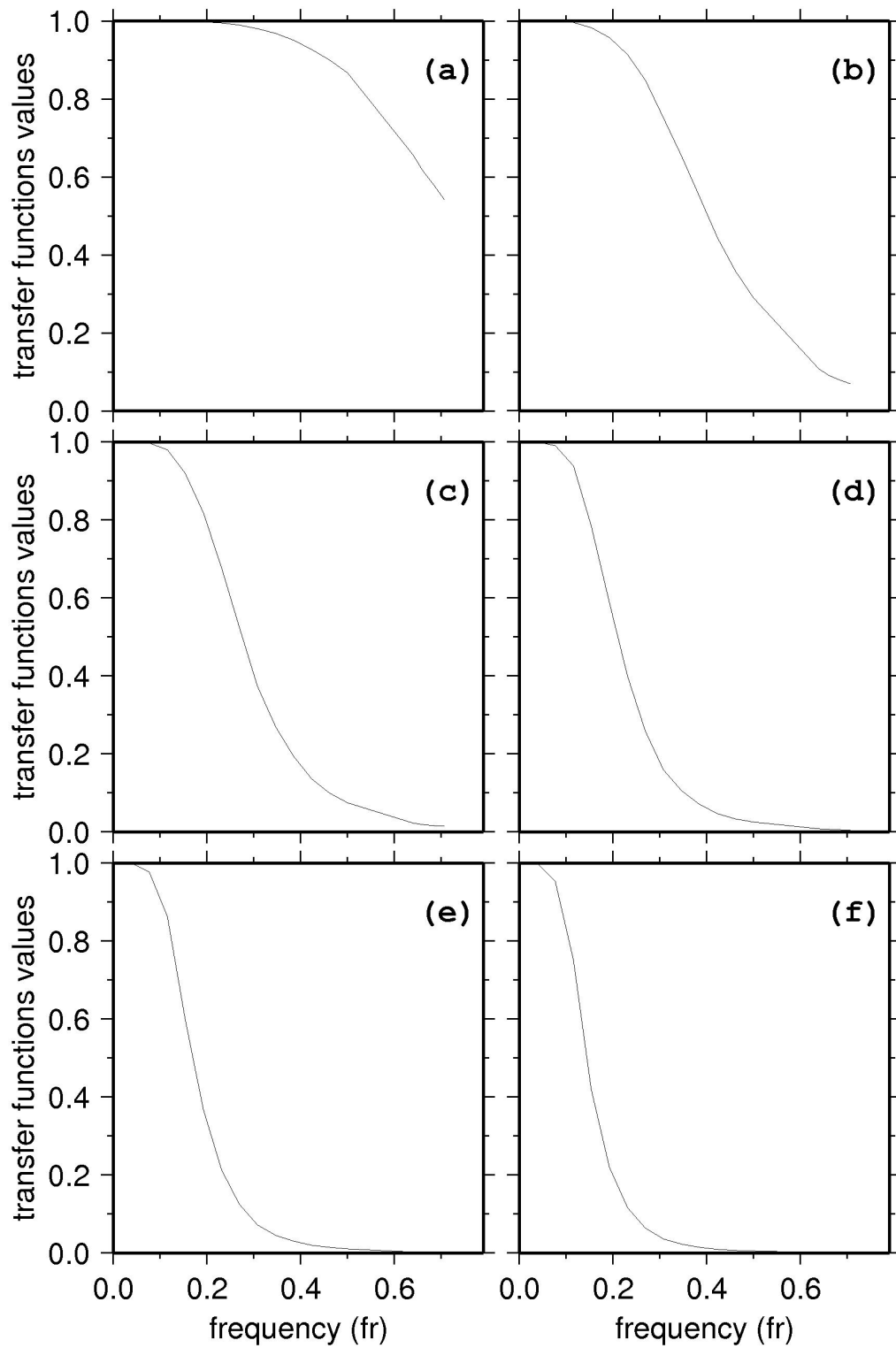
Fig. 6-9 1D frequency response of Wiener filter. (a) $k = 5$ (b) $k = 10$ (c) $k = 15$ (d) $k = 20$ (e) $k = 25$ (f) $k = 30$.
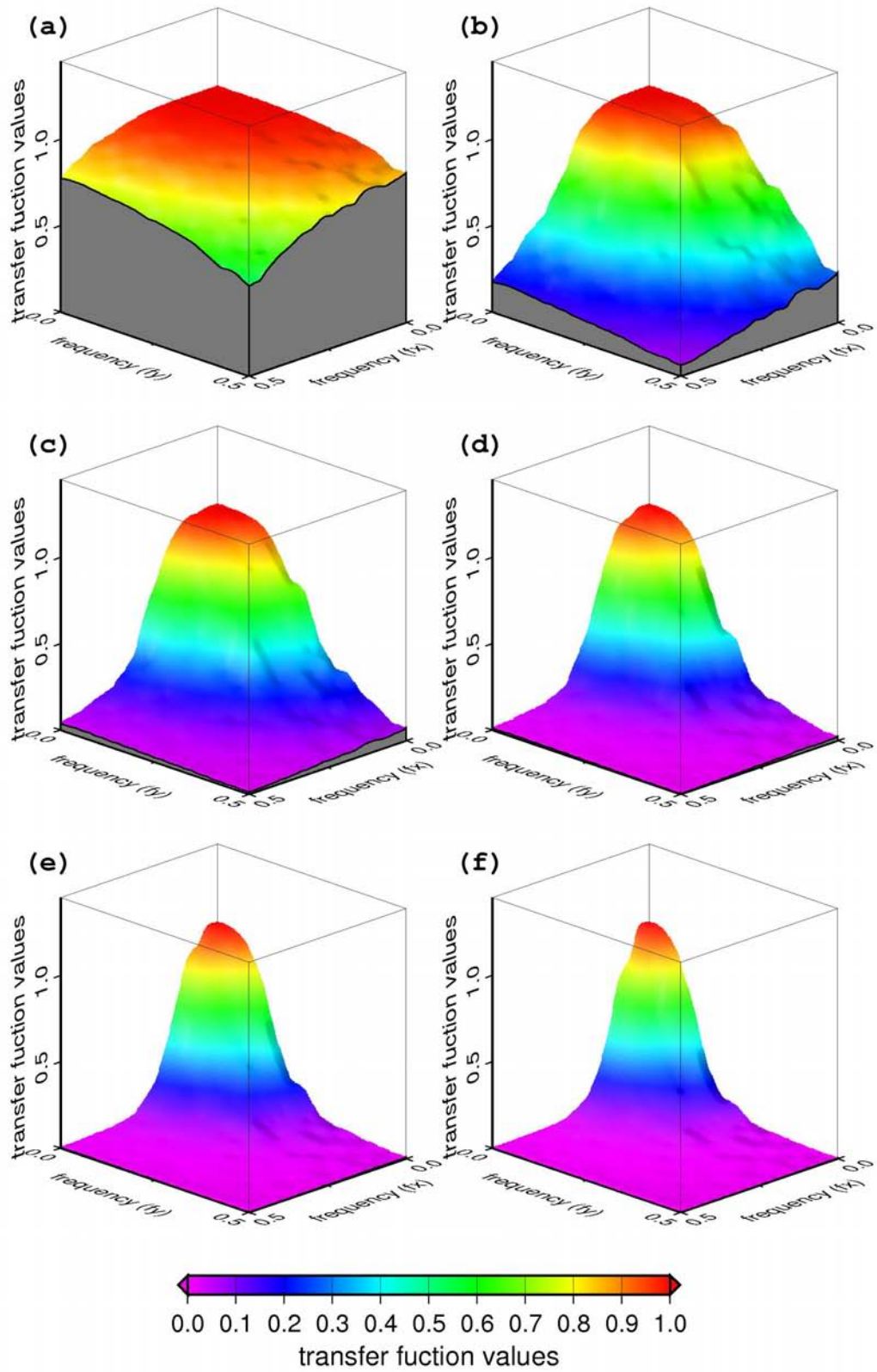
Fig. 6-10 2D frequency response of Wiener filter. (a) $k = 5$ (b) $k = 10$ (c) $k = 15$ (d) $k = 20$ (e) $k = 25$ (f) $k = 30$.
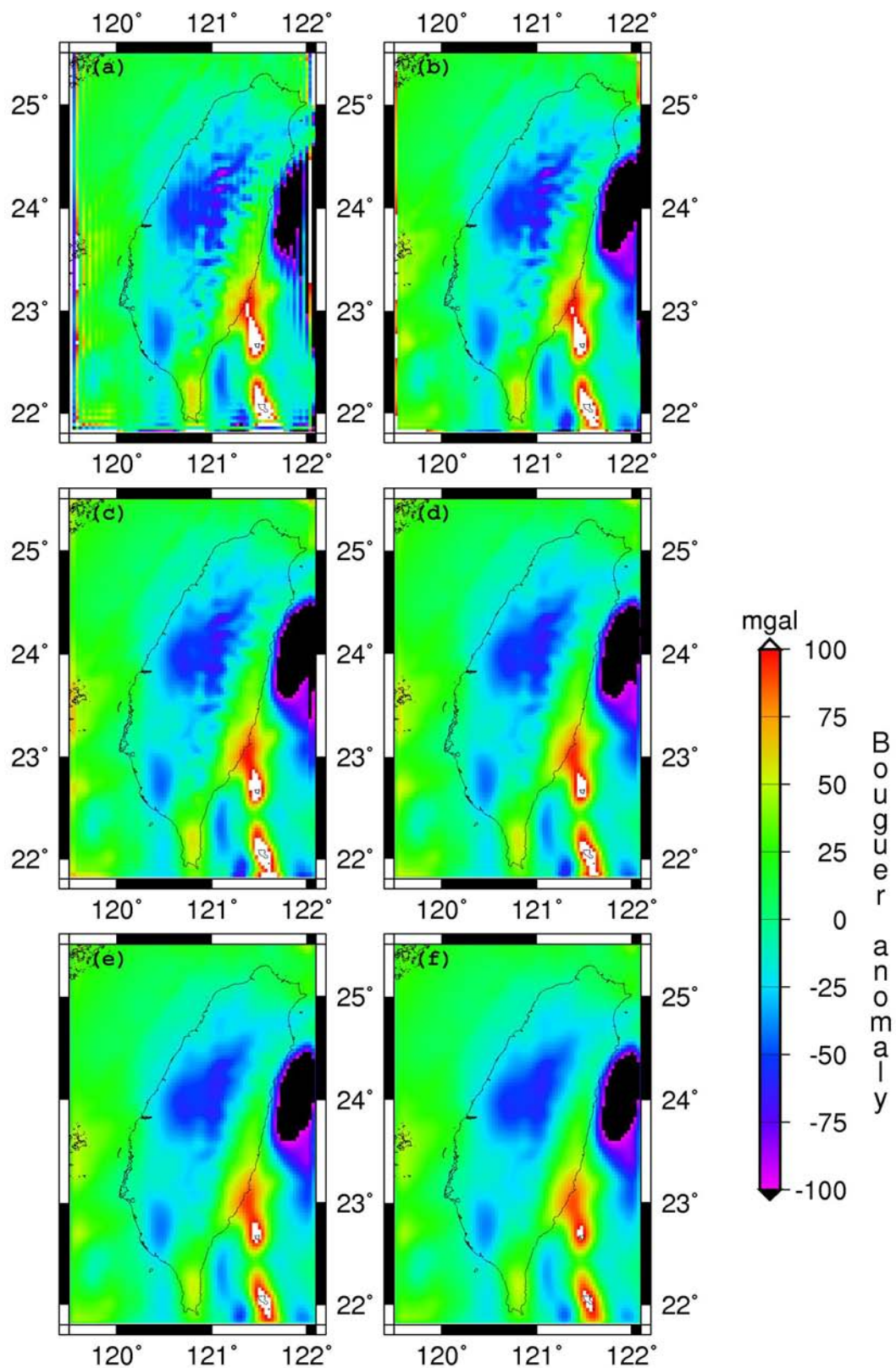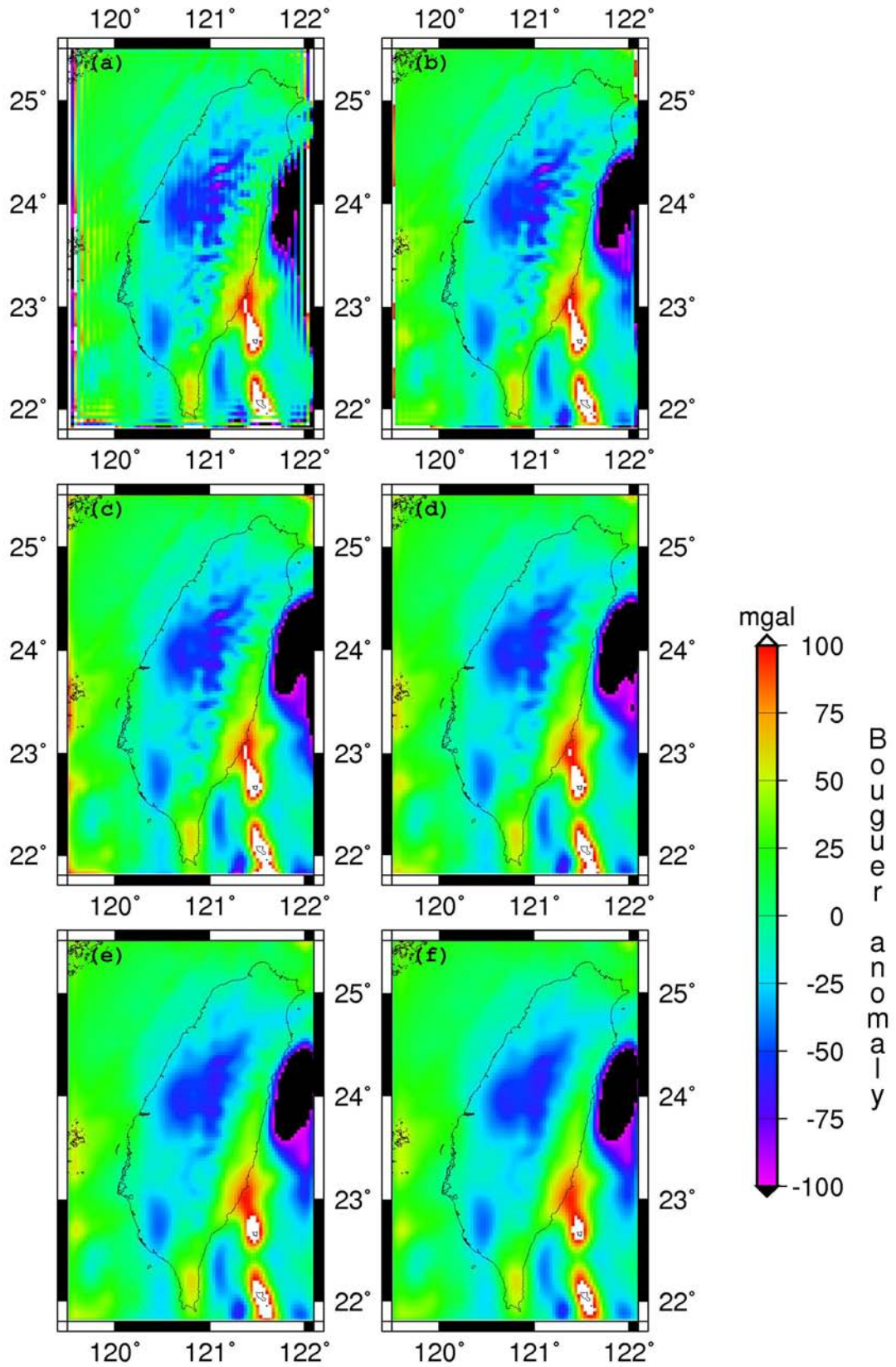
Fig. 6-11 Downward-continued Bouguer anomalies by Wiener filter. (a) $k = 5$ (b) $k = 10$ (c) $k = 15$ (d) $k = 20$ (e) $k = 25$ (f) $k = 30$.
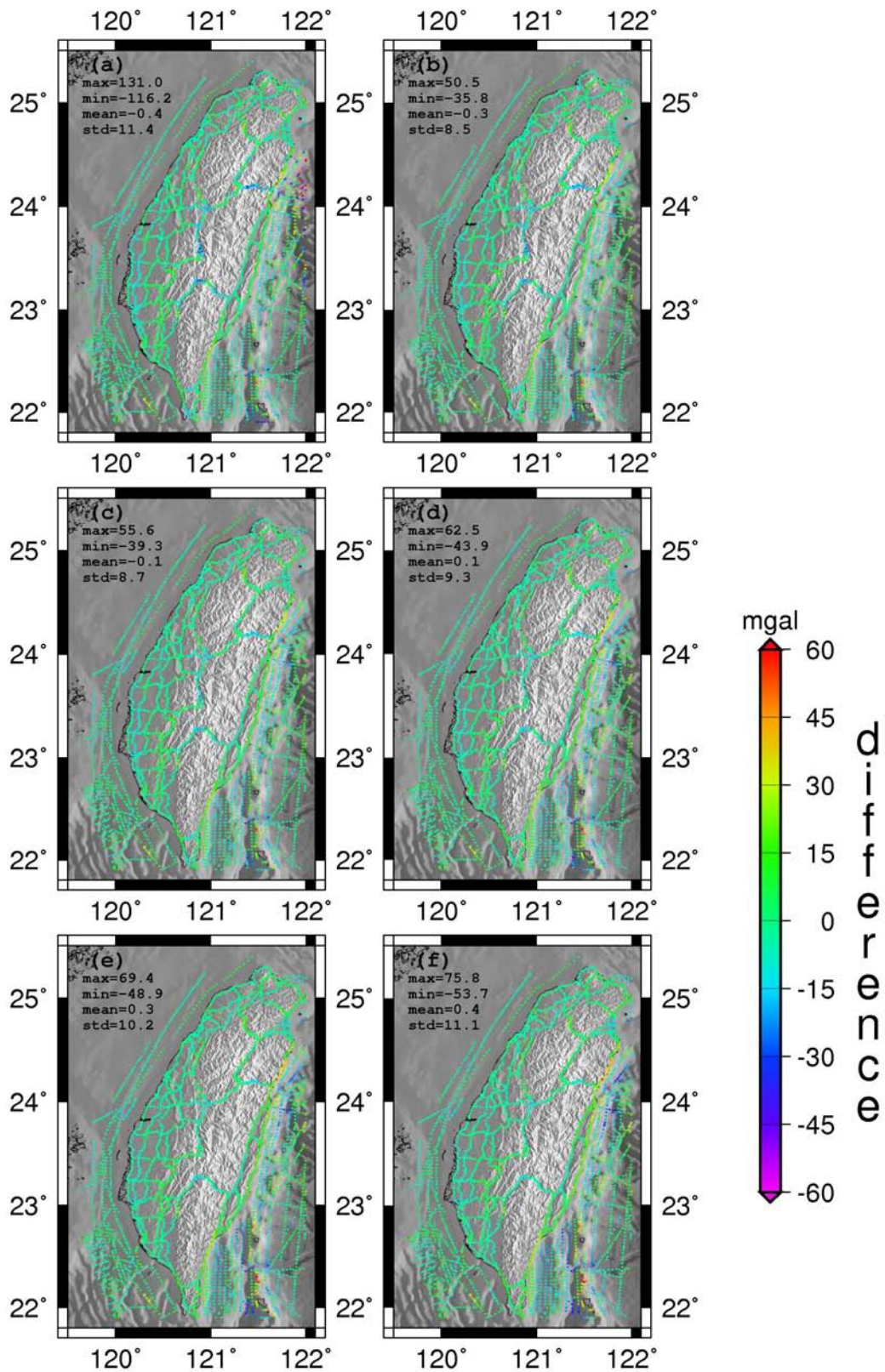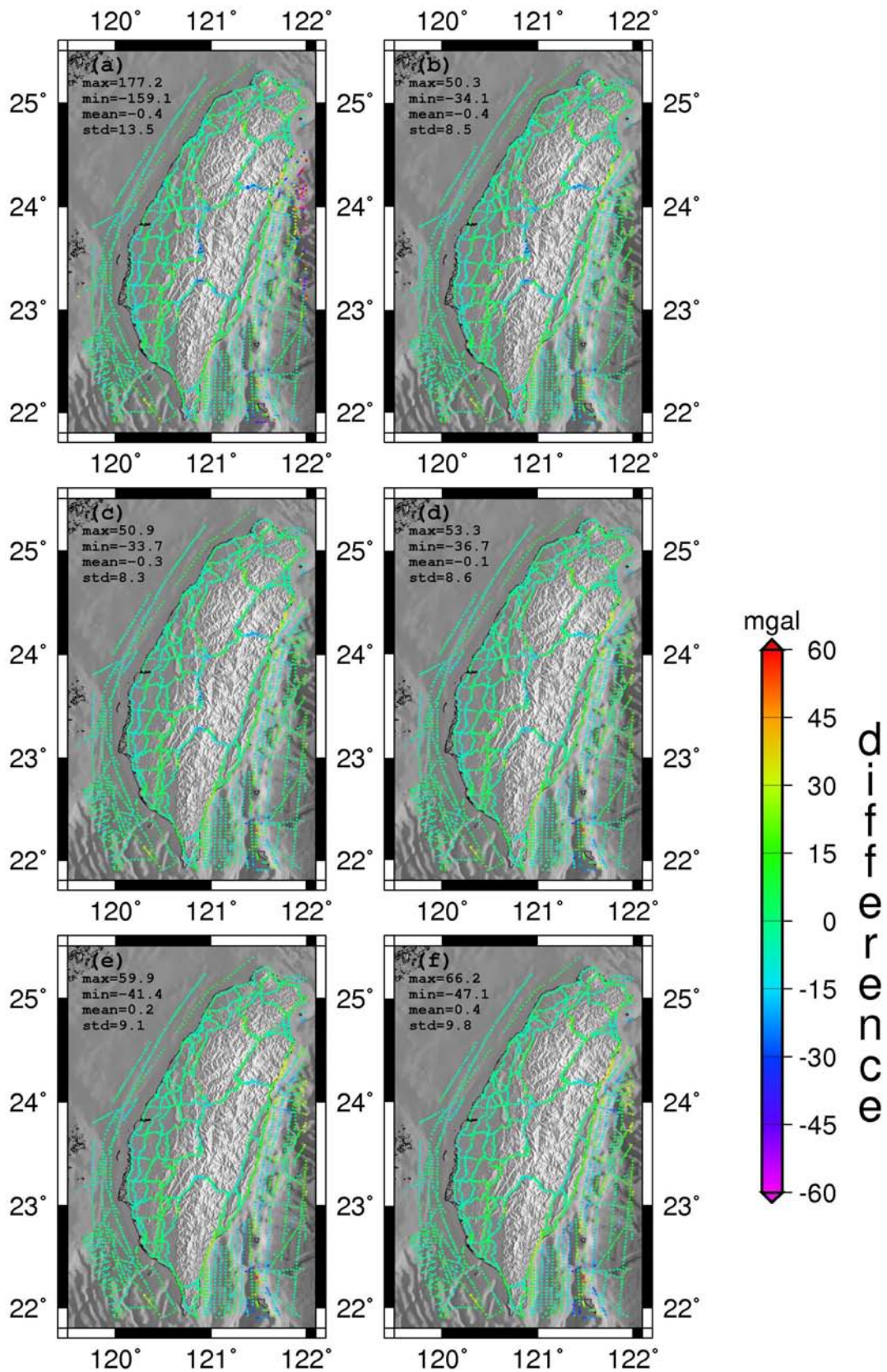
Fig. 6-12 Differences between the Bouguer anomalies of surface and downward-continued airborne data by Wiener filter. (a) $k = 5$ (b) $k = 10$ (c) $k = 15$ (d) $k = 20$ (e) $k = 25$ (f) $k = 30$.
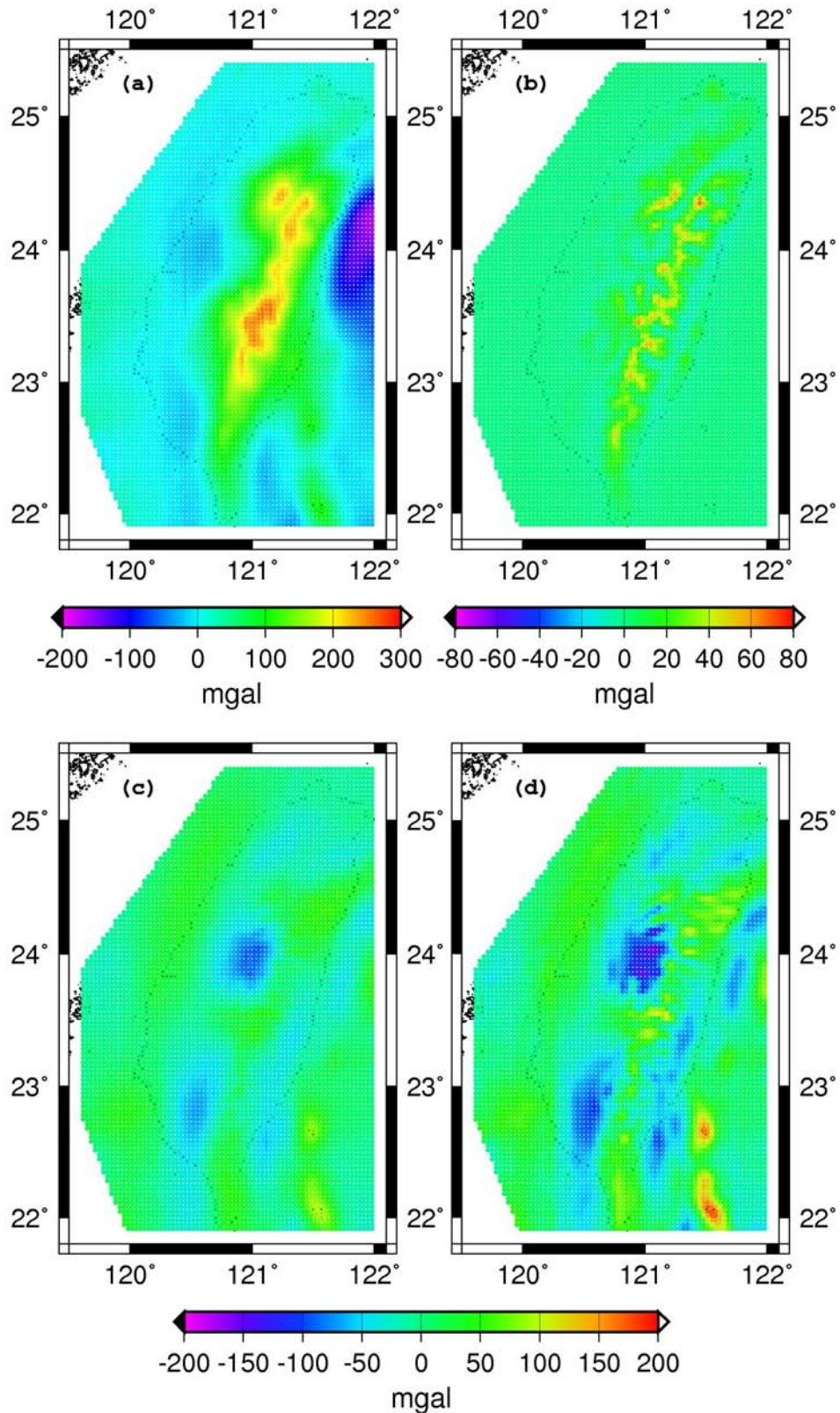
Fig. 6-13 (a)Free-air anomalies of airborne data at 5156 m. (b) RTM-derived effects of airborne data at 5156 m. (c)Residual gravity anomalies of airborne data at 5156 m. (d) Downward-continued residual gravity anomalies by LSC method.
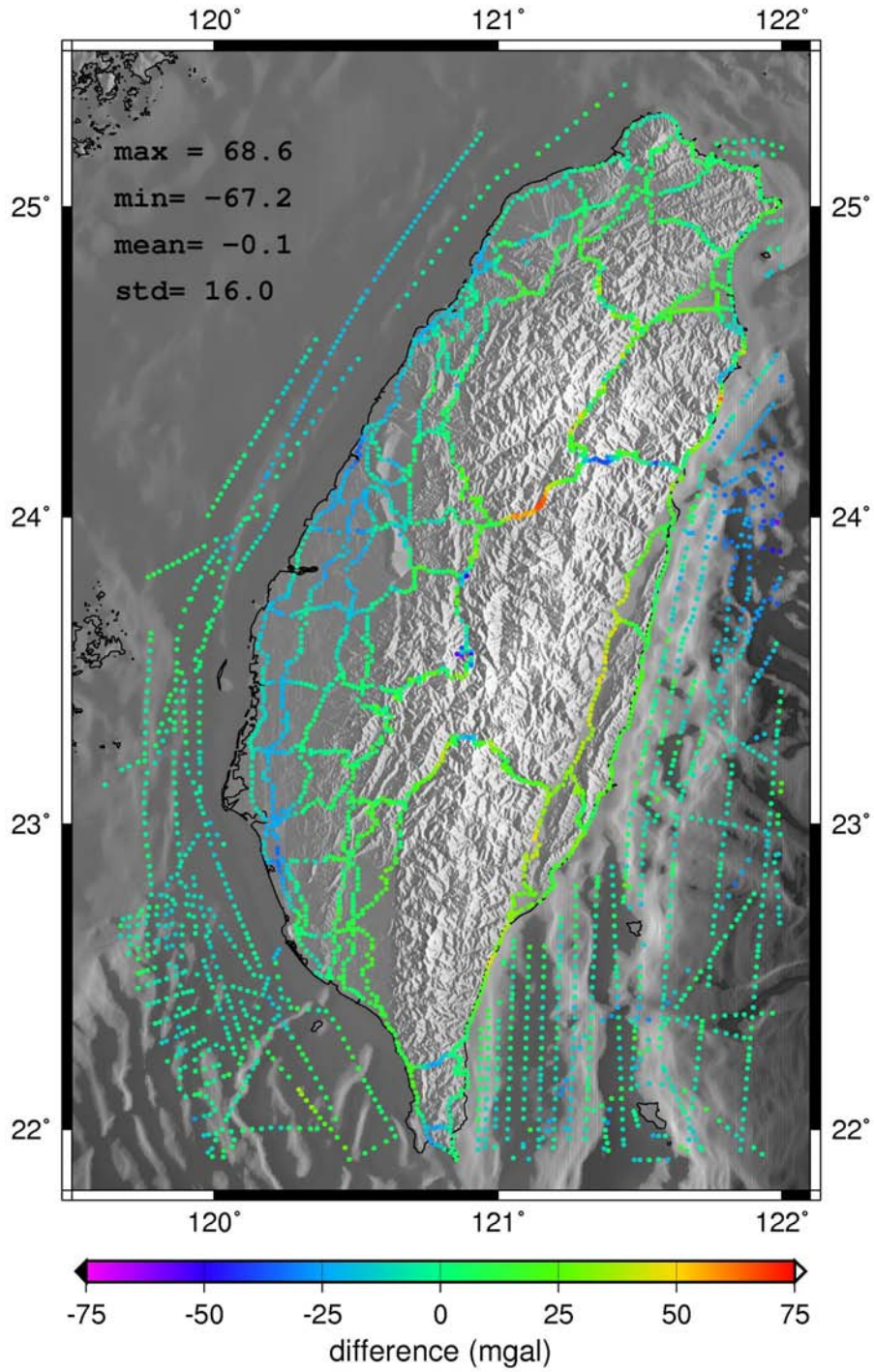
Fig. 6-14 Differences between the residual gravity anomalies of surface and downward-continued data by LSC method.
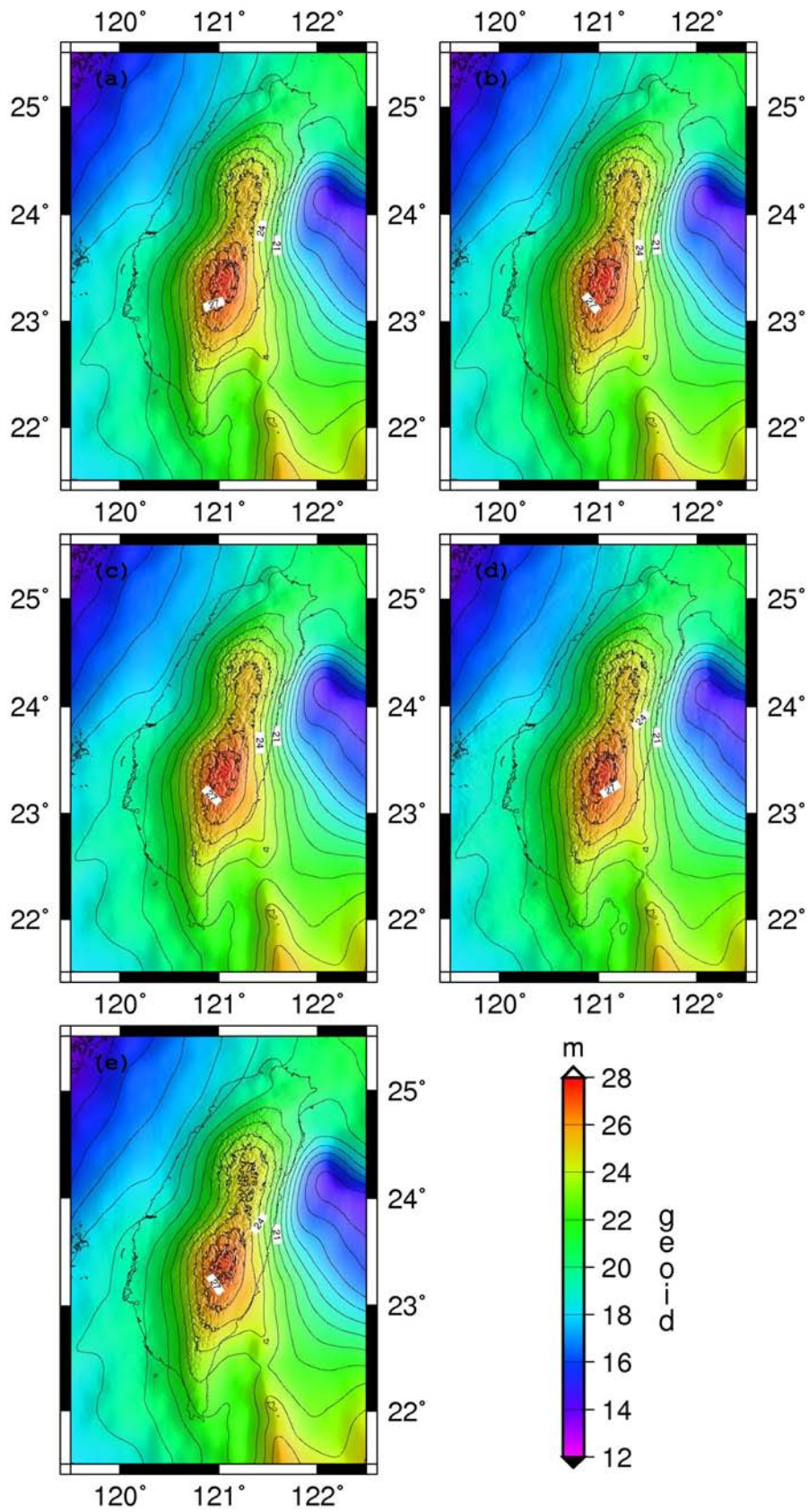
Fig. 6-15 The geoid models. (a) case A. (b) case B. (c) cases C. (d) case D (e) case E.
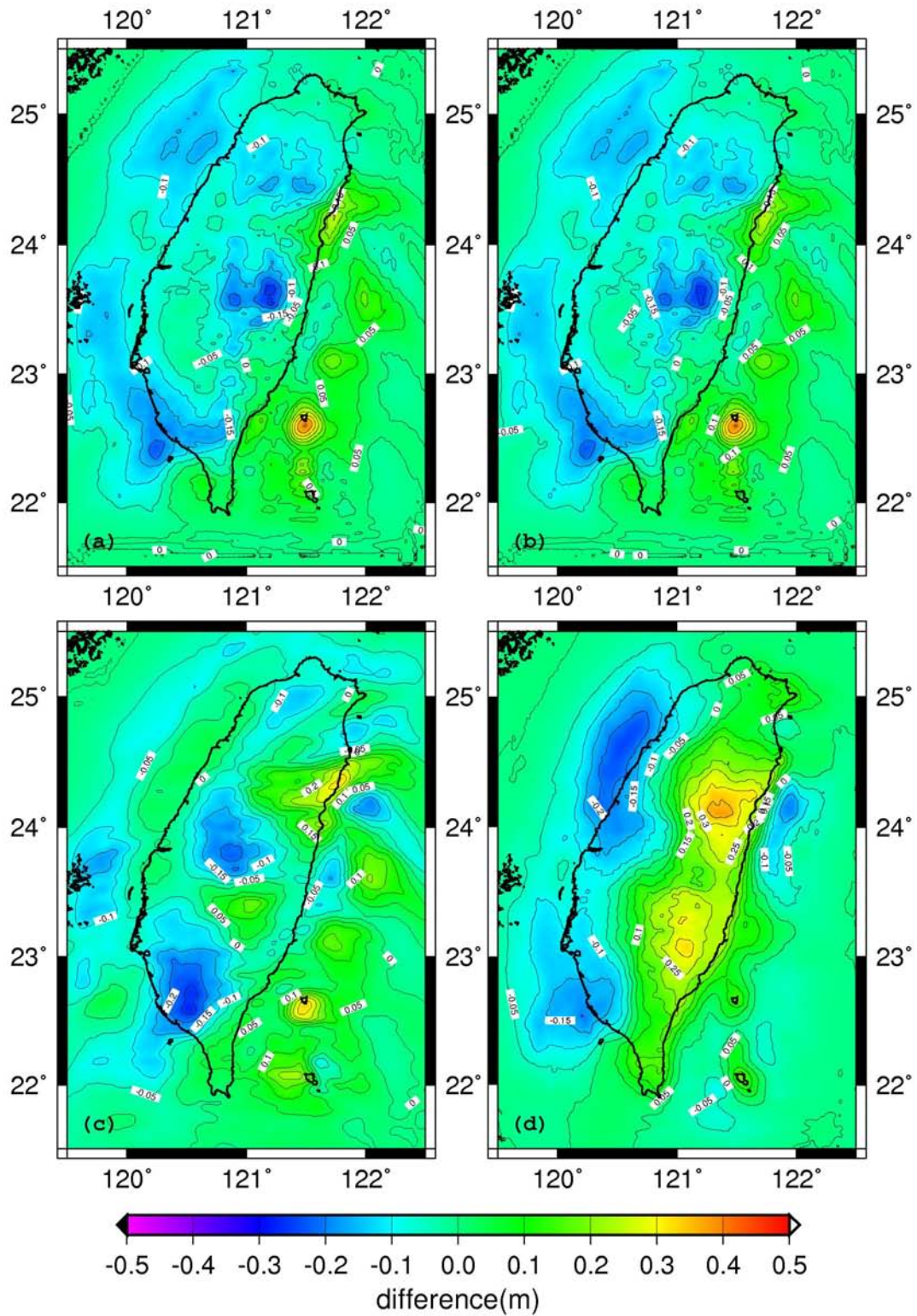
Fig. 6-16 Differences between all the geoid models. (a) Between cases A and B. (b) Between cases A and C. (c) Between cases A and D. (d) Between cases A and E.
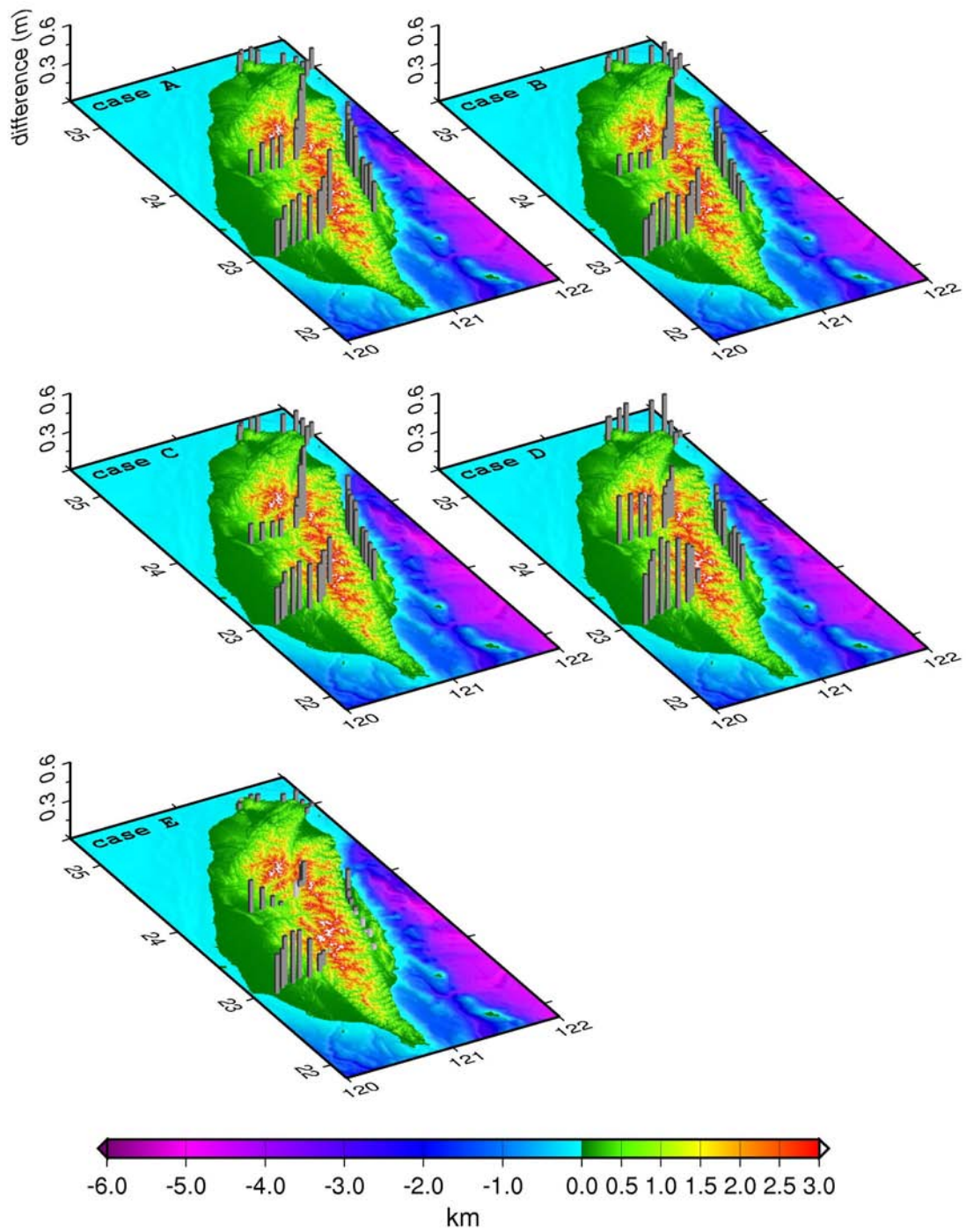
Fig. 6-17 Differences (in m) between the observed and modeled geoidal heights (cases A~E) along four leveling routes. Dark-gray and light-gray bars indicate positive and negative differences, respectively. The colors denote topography.
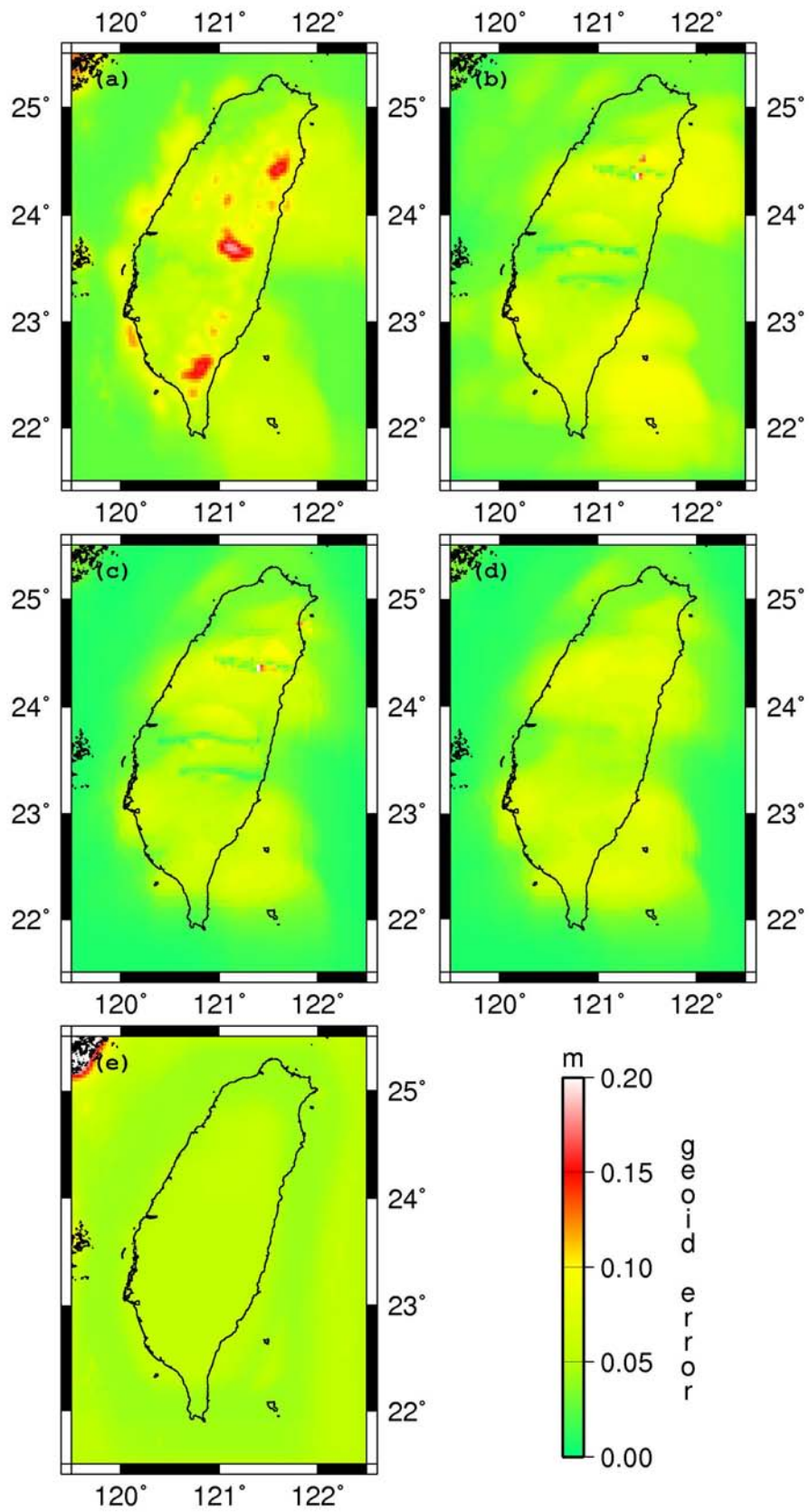
Fig. 6-18 The adjusted geoid errors for (a) case A. (b) case B. (c) cases C. (d) case D
(e) case E.

Chapter 7

Summary, Conclusions, and Recommendations

7.1 Summary

In the study described in this dissertation, we investigated the best computational method for obtaining RTM-derived effects and the most ideal DWC technique used in airborne gravity data. The purpose of this study is to model the best geoid over Taiwan and the surrounding seas.

In chapter 2, we presented detailed methodologies for geoid modeling and UW/DWCs. The strategy of the geoid modeling was based on the RCR procedure. The long-wavelength part was based on a geopotential model and the short-wavelength part was obtained using the principle of RTM. The residual geoid was determined by LSC. UW/DWCs were performed by using the FFT and LSC. For the FFT, a smoothing filter was considered.

The data used for the geoid modeling in this study were introduced in chapter 3 (excluding airborne gravity data). The data include surface gravity and altimeter-derived data for the residual geoid, the GGM for long-wavelength gravity and geoid computation, the DEM and a density model for short-wavelength gravity and geoid computation, and some GPS/leveling points for assessing the geoid accuracy. The surface gravity data comprise land and shipborne gravity data. Altimeter-derived data and GGM used in this study are from KMS02 and EIGEN-GL04C models. The DEMs involve three resolutions—9 s, 90 s, and 6 min.

In chapter 4, three computation methods for determining the RTM-derived effects were applied to the investigations of short-wavelength gravity and geoid computations. These methods were the FFT, prism, and Gaussian quadrature techniques. The topographic density variation was also considered in this study. The result shows that if the FFT is used to compute the RTM-derived effects, it provides the best geoid accuracy through the evaluation of the GPS/leveling points. Moreover, if the density variation is considered in geoid modeling, the maximum difference between the new and original geoid surfaces is 4 cm.

The principle of airborne gravimetry and the airborne gravity survey of Taiwan were introduced in chapter 5. The airborne gravity signals possess information pertaining to the *Etövös* effect, tilt correction, and vertical acceleration of the

aircraft. The airborne gravity survey of Taiwan was sponsored by the MOI and implemented in 2004~2005 to fill the gaps in the existing ground gravity coverage In comparison to UWC. The survey work and software development for this project were performed by NCTU and KMS together. In the repeatability analysis, the filter width of 150 s used in the raw airborne gravity observations is a compromise between noise reduction and gravity signal preservation. In the crossover analysis, most differences vary from 7 to –7 mgal and have a standard deviation of 2.88 mgal after bias and drift corrections. In comparison to UWC, most Bouguer anomaly differences between the surface and the airborne data are small; however, some large differences over high mountains can reach approximately 50 mgal.

In the investigations in chapter 6, one of the main topics was the application of DWC to airborne data and the other was geoid determination by combining the surface and downward-continued data. Two DWC methods, the FFT and LSC, were applied to process the data from the airborne gravity survey of Taiwan. In the FFT, Gaussian and Wiener filters were used to eliminate noises due to the ill-posed problem. From a comparison with ground Bouguer anomalies, the Gaussian and Wiener filters were found to provide the best DWC results when the parameter k was equal to 10 and 15, respectively. On the other hand, LSC is divided into direct and indirect geoid determinations. Downward-continued data combining land, shipborne, and altimeter-derived gravity data were used for the geoid modeling; the short-wavelength part of the model was computed using the FFT method. The geoid models in the five cases showed an apparent improvement in the geoid accuracies over some areas with high mountains. A relative geoid accuracy under 10 cm could be achieved over these rough terrains. However, the geoid that was directly determined using airborne gravity data was considerably different from that obtained from the data that was downward-continued to the sea level. The difference between the geoid models of the two determinations could reach 30~40 cm.

7.2 Conclusions

The primary contribution of the research described in this dissertation is with regard to the enhancement in the geoid accuracy over Taiwan, particularly over areas with high mountains. The major contribution is from airborne gravity.

Among the three computation methods for the RTM-derived effects, FFT provides the best result through the evaluation of GPS/leveling points. One major reason is that the RTM-derived gravity and geoid data computed using FFT are stored on 9-s grids and those computed using prism and Gaussian quadrature are stored on 1-min grids. Both the prism and Gaussian quadrature methods are pointwise methods and are impracticable for high-resolution computational tasks. The DEM of Taiwan has been developed to very high resolutions. Therefore, FFT is the best choice for the computation of the RTM-derived effects. Furthermore, even if the difference of standard deviations is small, the consideration of density variation in the geoid modeling is still important since the resulting change in the geoid model compared to the use of a constant density is not small.

The overall accuracy of the airborne gravity survey of Taiwan is approximately 2 to 3 mgal based on the analyses of crossover and repeatability differences. The level of accuracy conforms to that of other airborne gravity surveys around the world. In addition, over most areas, the airborne gravity anomalies agree well with the existing surface gravity data that are upward continued to the flight altitude. Although some large differences still occur between the airborne and the surface data over high mountains due to the sparse coverage of the surface gravity data, the airborne gravity data can fill the gaps in the surface gravity data.

In the five cases considering different downward-continuation methods, although four GPS/leveling routes agree well with the improvements in these geoid accuracies, some large differences among the geoids in these models still occur; this is particularly true in the case of the geoid model involving the direct determination of the geoid using LSC. The reason is that the covariance model used in this study may be not suitable for airborne and surface data for directly computing the geoid. In addition, Bouguer anomalies used in the FFT DWC are better than free-air anomalies in geoid modeling.

The best geoid model obtained in this study is expected to aid in GPS leveling, ocean circulation determination, and linking Taiwan's height datum to the world height datum. However, an improved geoid can be obtained after the gravimetrically determined geoid has been corrected a bias and tilt hiding in the long-wavelength geoid by using well-distributed GPS/leveling points.

7.3 Recommendations for Future Work

To further improve the geoid accuracy, there are several topics that need to be investigated in future work.

(1) New data for geoid modeling

The data used for the geoid computation has been increasing in recent years. With regard to the local gravity data, more land, shipborne, and airborne gravity data measured over Taiwan and the surrounding seas will be acquired soon. We can further improve the geoid accuracy using these data. Besides the local gravity data, a high-resolution GGM, such as EGM06 coefficients, has been developed to degree 2190. It represents the earth potential more explicitly and provides more precise long-wavelength effects for geoid modeling. On the other hand, a 5-m resolution of the DEM over Taiwan is to be achieved by photogrammetry and LIDAR. This DEM is useful to refine the accuracy of the short-wavelength effects.

(2) 2D density model used in FFT and Gaussian quadrature

In chapter 4, a 2D density model was used only in the prism method. Its use in the FFT and Gaussian quadrature methods should be investigated.

(3) 3D density data

We considered only a 2D density when computing the RTM-derived effects. Three-dimensional density data should fit in with the real topographic density variation

(4) Investigation of a more suitable covariance model

In this study, the Tscherning-Rapp degree variance model may not be suitable for the DWC of the direct geoid determination method. Other methods for constructing new covariance models should be investigated.

(5) Use of band-limited covariance function

The gravity data used in this study are from variety of sources. Unlike land gravity anomalies, most of the high-frequency gravity anomalies were removed from the original sources. Therefore, these gravity data are of limited spatial resolutions.

Therefore, a more rigorous method of geoid modeling than the method used in this study is to use band-limited covariance functions in LSC or band-limited kernel functions in the Stokes integral (Novak and Heck, 2002).

Reference

Andersen, O.B., P. Knudsen, S. Kenyon, and R. Trimmer (2003). KMS2002 global marine gravity field, bathy-metry and mean sea surface, *Poster*, *IUGG2003*, Sapporo, Japan, June30-July11, 2003.

Angelier, J., H.T. Chu, and J.C. Lee (1997). Shear concentration in a collision zone: kinematics of the active Chihshang Fault, Longitudinal Valley, eastern Taiwan, *Tectonophysics*, **274**, pp. 117-144.

Attila, M. (1984). Digital Filtering: Applications in Geophysical Exploration for Oil, *Akademiai Kiado*, Budapest.

Bastos, L., R. Forsberg, A. Gidskehaug, K. Hehl, and U. Meyer (1998). An airborne geoid mapping system for regional sea-surface topography: application to the Skagerrak and Azores areas, Geodesy on the Move, *IAG Symposia*, **119**, pp.30-36, Springer-Verlag.

Bayoud, F.A., and M.G. Sideris (2003). Two different methodologies for geoid determination from ground and airborne gravity data, *Geophys. J. Int.*, **155**, pp. 914-922.

Bell, R.E., V.A. Childers, R.A. Arko, D.D. Blankeship, and J.M. Brozena (1999). Airborne gravity and precise positioning for geologic applications, *J. Geophys. Res.*, **104**, pp.15281-15292.

Beutler, G., H. Bock, E. Brockmann, R. Dach, P. Fridez, W. Gurtner, H. Habrich, U. Hugentobler, D. Ineichen, M. Meindl, L. Mervart, M. Rothacher, S. Schaer, T. Springer, U. Urschl, and R. Weber (2004). Bernese GPS software version 5.0 Draft, *Astronomical Institute*, University of Bern, Bern, Switzerland.

Blakely, R.J. (1995). Potential Theory in Gravity and Magnetic Applications, *Cambrige University Press*, UK.

Bouziane, M. (1996). The new Algerian quasi-geoid 96 computed using spherical FFT, *IGeS Bulletin no 5*, pp. 40-56.

Brozena, J.M. and M.F. Peters (1988). An airborne gravity study in eastern North Carolina, *Geophysics*, **53**, pp.245-253.

Brozena, J. (1992). The Greenland aerogeophyscis experiment, Airborne Gravity, Topographic and Magnetic Mapping of an entire Continent. In: Colombo (ed.): From Mars to Greenland: Charting Gravity with Space and Airborne Instruments. *IAG Symposia*, **110**, pp. 203-214, Springer Verlag.

Buttkus, B. (2000). Spectral Analysis and Filter Theory, *Springer*, Berlin.

Chen, C.S. (2003). Gravity survey mission on first-order second-level benchmarks, *Reports of Ministry of Interior*, Taiwan.(in Chinese)

Childers, V.A., R.E. Bell, and J.M. Brozena (1999). Airborne gravimetry: an investigation of filtering, *Geophysics*, **64**, pp. 61-69.

Childers, V.A., D.C. McAdoo, J.M. Brozena, and S.W. Laxon (2001). New gravity data in the Artic Ocean: comparison of airborne and ERS gravity, *J. Geophys. Res.*, **106**, pp. 8871-8886.

Chiou, Y.H. (1997). The generation and application of the digital density model of Taiwan area, *MSD theses of department of civil engineering*, National Chiao Tung University, Hsinchu, Taiwan.(in Chinese)

Denker, H. and H.G. Wenzel (1987). Local geoid determination and comparison with GPS results, *B. Geod.*, **61**, pp. 349-366.

Denker, H., D. Behrend, and W. Torge (1997). The European gravimetric quasigeoid EGG96, *Gravity, Geoid and Marine Geodesy, IAG Symp*, **117**, pp. 532-539, Segawa, Japan.

Flury, J. (2006) Short-wavelength spectral properties of the gravity field from a range of regional data sets, *J. Geod.*, **79**, pp. 624–640.

Forsberg, R. (1984). A study of terrain reductions, density anomalies and geophysical inversion methods in gravity field modelling, *Reports of department of geodetic Science and Surveying*, **355**, The Ohio State University, Columbus, Ohio.

Forsberg, R. (1985). Gravity field terrain effect computation by FFT, *B. Geod.*, **59**, pp. 342-360.

Forsberg, R. (1987). A new covariance model for inertial gravimetry and gradiometry, *J. Geophys. Res.*, **92**, pp. 1305-1310.

Forsberg, R., and M. G. Sideris (1993), Geoid computations by the multi-band spherical FFT approach, *Manuscr. Geodaet*, **18**, pp. 82-90.

Forsberg, R., D. Solheim, and J. Kaminskis (1996). Geoid of the Nordic and Baltic area from gravimetry and satellite altimetry, *Proc. Int. Symposium on Gravity, Geoid and Marine Geodesy*, Tokyo, pp. 540-548.

Forsberg, R. and C.C. Tscherning (1997). Topographic effects in gravity field modelling for BVP. In: Sans`o F, RummelR(eds) Geodetic boundaryvalue problems in view of the one centimeter geoid, *Lecture notes in earth sciences*, **65**, Springer, Berlin Heidelberg NewYork, pp. 241–272.

Forsberg R., and D. Solheim (2000). Geoid of the Nordic/Baltic region from surface/airborne gravimetry and GPS draping, *Proc. Int. Symposium on Gravity, Geoid and Geodynamics*, Banff, Canada.

Forsberg, R., A.V. Olesen, L. Bastos, A. Gidskehaug, U. Meyer, and L. Timmen (2000). Airborne geoid determination, *Earth. Planets. Space.*, **52**, pp. 863–866.

Forsberg, R., A.V. Olesen, K. Keller, and M. Moller (2003a). Airborne gravity survey of sea areas around Greeland and Svalbard, *Technical reports of National Survey and Cadastre*, **18**, Denmark.

Forsberg, R., K. Keller, S.M. Hvidegaard, and A.V. Olesen (2003b). European airborne gravity and Lidar survey in the Arctic Ocean, *Technical reports of National Survey and Cadastre*, **21**, Denmark.

Forsberg, R. and H. Skourup (2005). Arctic ocean gravity, geoid and sea-ice freeboard heights from ICESat and GRACE, *Geophys. Res. Lett.*, **32**, L21502.

GFZ (2006). The introduction and data source of EIGEN-GL04C coefficients, *http://www.gfz-potsdam.de/pb1/op/grace/results/grav/g005_eigen-gl04c.html*.

Glennie, C. and K.P. Schwarz (1999). A comparison and analysis of airborne gravimetry results from two strapdown inertial/DGPS systems, J Geod, 73, pp. 311-321.

Gerald, C.F. and P.O. Wheatley (1994). Applied Numerical Analysis. 5th ed, *Addison Wesley Pub Co*, New York, 748pp.

Goad, C.C. and M. Yang (1997). A new approach to precision airborne GPS positioning for photogrammetry, *Photogramm. Eng. Rem. S.*, **63**, pp. 1067-1077.

Harlan, R. (1968). Eötvös corrections for airborne gravimetry, *J. Geophys. Res.*, **73**, pp. 4675-4679.

Heiskanen, W.A. and H. Moritz (1967). Physical Geodesy, *W.H. Fredman and company* ,San Francisco and London.

Hsu, SK., CS Liu, CT. Shyu, SY. Liu, JC. Sibuet, S. Lallemand, C. Wang, and D. Reed (1998). New gravity and magnetic anomaly maps in the Taiwan-Luzon region and their preliminary interpretation, *Terr. Atmos. Ocean. Sci.*, **9**, pp.509-532.

Huang J., P. Vanicek, S.D. Pagiatakis, and W. Brink (2001). Effect of topographical density on geoid in the Canadian Rocky Mountains, *J. Geod.*, **74**, pp. 805–815.

Huang, J. (2002). Computational methods for the discrete downward continuation of the Earth gravity and effects of lateral topographical mass density variation on gravity and the geoid, *PHD theses of Department of Geodesy and Geomatics Engineering*, University of New Brunswick, Canada.

Hunegnaw, A. (2001). The effect of lateral density variation on local geoid determination, *Boll. Geod. Sci. Aff.*, **60**, pp.123–145.

Hwang, C (1997). Analysis of some systematic errors affecting altimeter-derived sea surface gradient with application to geoid determination over Taiwan, *J. Geod.*, **71**, pp. 113-130.

Hwang, C. (2001). Gravity survey mission on first-order first-level benchmarks, *Reports of Ministry of Interior*, Taiwan.(in Chinese)

Hwang, C., C.G. Wang, and L.H. Lee (2002). Adjustment of relative gravity measurements using weighted and datum-free constraints, *Comput. Geosci.*, **28**, pp. 1005-1015.

Hwang, C. (2003) The estimation of accuracy of Taiwan geoid model, *Reports of Ministry of Interior*, Taiwan.(in Chinese)

Hwang, C. and Y.S. Hsiao (2003), Orthometric correction from leveling, gravity, density and elevation data: a case study in Taiwan, *J. Geod.*, **77**, pp. 279-291.

Hwang, C., Y.S. Hsiao, and T.L. Lin (2003a). A digital elevation model of Taiwan and

accuracy assessment, *Cadastre Survey*, **22 (2)**, pp.1-19. (in Chinese)

Hwang, C., C.G. Wang, and YS Hsiao (2003b). Terrain correction computation using Gaussian quadrature: effect of innermost zone, *Comput. Geosci.*, **29**, pp. 1259-1268.

Hwang, C. (2005). Airborne gravimetry research, *Reports of Ministry of Interior*, Taiwan.(in Chinese)

Hwang, C., A. Ellmann, and YS. Hsiao (2006a). Toward a one-cm geoid in Taiwan: contribution of airborne gravity data and high-resolution DEM, *International Workshop on Height Systems, Geoid and Gravity of the Asia-Pacific*, Ulaanbaatar, Mongolia, June 6 - June 9.

Hwang, C., Y.S. Hsiao, and H.C. Shih. (2006b) Data reduction in scalar airborne gravimetry: Theory, computer package and case study in Taiwan, *Comput. Geosci.*, **32**, pp. 1573-1584.

Hwang, C., Y.S. Hsiao, C.C Lu, W.S. Wu, and Y.H. Tseng (2007a). Determination of height of northeast Asia's highest peak (Mt. Jade) by direct leveling, *Surv. Rev.*, **39 (303)**.

Hwang, C., Y.S. Hsiao, H.C. Shih, M. Yang, K.H., Chen, R. Forsberg, and A.V. Olesen (2007b). Geodetic and geophysical results from a Taiwan airborne gravity survey: Data reduction and accuracy assessment, *J. Geophys. Res.*, **112(B10)**, DOI:10.1029/2005JB004220.

Jekeli, C. and J. Kwon (2002). Geoid profile determination by direct integration of GPS/INS vector gravimetry, *J. Geophys. Res.*, **107(B10)**, DOI: 10.1029/2001 JBod626.

Kearsley, A.H.W., R. Forsberg, A. Olesen, L. Bastos, K. Hehl, U. Meyer, and A. Gidskehaug (1998). Airborne gravimetry used in precise geoid computations by ring integration, *J. Geod.*, **72**, pp. 600-605.

Kennedy, S.L. (2002). Acceleration estimation from GPS carrier phases for airborne gravimetry, *UCGE Reports*, **20160**, Department of Geomatics Engineering, University of Calgary, Canada.

Kern, M., K.P. Schwarz, and N. Sneeuw (2003). A study on the combination of satellite, airborne and terrestrial gravity data, *J. Geod.*, **77**, pp. 217-225.

Kuhn, M. (2003). Geoid determination with density hypotheses from isostatic models and geological information, *J. Geod.*, **77**, pp.50–65.

Kunn, P.J. (1972). Application of Wiener filters to transformations of gravity and magnetic fields, *Geophys. Prospect.*, **20**, pp. 860-871.

LCR (2002). Graviton-EG user's manual, *Lacoste &Romberg Inc*, Austin, Texas.

LCR (2003). Model "S" air-sea dynamic gravity meter system Ⅱ, *LaCoste & Romberg instruction manual*, Austin, Texas.

LCR (1997) Instruction manul for Lacoste & Romberg model G land gravity meter, *Lacoste &Romberg Inc.*, Austin, Texas.

Li, Y.C. (2000). Airborne gravimetry for geoid determination, *UCGE reports*, **20141**, Department of Geomatics Engineering, University of Calgary, Calgary.

Martinec, Z. (1998). Boundary-value problems for gravimetric determination of a precise geoid, *Lecture Notes in Earth Sciences*, **73**, Berlin Heidelberg New York.

Micro-g (1999). Operator's manual of FG5 absolutely gravimeter, *Micro-g Inc.,* USA.

Mittal, P. (1984). Algorithm for error adjustment of potentiel-field data along a survey network, *Geophysics*, **49**, pp. 467–469.

Moritz, H. (1980). Advanced Physical Geodesy, *Wichmann,* Karlsruhe.

Nahavandchi, H. and L.E. Sjoberg (2001). Two different views of topographical and downward-continuation corrections in the Stokes-Helmert approach to geoid computation, *J. Geod.*, **74**, pp. 816-822.

Novak, P. (2003). Optimal model for geoid determination from airborne gravity, *Stud. Geophys. Geod.*, **47**, pp.1−36.

Novak, P. and B. Heck (2002). Downward continuation and geoid determination based on band-limited airborne gravity data, *J. Geod.*, **76**, pp. 269-278.

Novak, P., M. Kern, K.P. Schwarz, M.G. Sideris, B. Heck, S. Ferguson, Y. Hammada, and M. Wei (2003). On geoid determination from airborne gravity, *J. Geod.*, **76**, pp. 510–522.

Olesen, A.V., R. Rorsberg, K. Keller, and A. Gidskehaug (2000). Airborne gravity survey of Lincoln Sea and Wandel Sea, North Greenland, *Phys. Chem. Earth. Pt. A.*, **25**, pp. 25-29.

Olesen, A.V., O.B. Anderson, and C.C. Tscherning (2002). Merging airborne gravity and gravity derived from satellite altimetry: test cases along the coast of Greenland, *Stud. Geophs. Geod.*, **46**, pp.387-394.

Olesen, A.V. (2003). Improved airborne scalar gravimetry for regional gravity field mapping and geoid determination, *Technical reports of National Survey and Cadastre*, **24**, Denmark.

Omang, O.C.D. and R. Forsberg (2000). How to handle topography in practical geoid determination: three examples, *J. Geod.*, **74**, pp. 458-466.

Pagiatakis, S.D., D. Fraser, K. Mcewen, A.K. Goodacre, and M. Veronneau (1999). Topographic mass density and gravimetric geoid modeling, *Boll. Geofis. Teor. Appl.*, **40**, pp. 189-194.

Press, W. H., B.P. Flannery, S.A. Teukolsky, and W.T. Vetterling (1989). Numerical Recipes, *Cambridge University Press*, New York, 874pp.

Schwarz, K.P., M.G. Sideris, and R. Forsberg (1990). The use of FFT techniques in physical geodesy, *Geophys. J. Int.*, **100**, pp. 485-514.

Schwarz, K.P. and Y.C. Li (1996). What can airborne gravimetry contribute to geoid determination?, *J. Geophys. Res.*, **101**, pp. 17873-17881.

Seeber, G. (1993). Satellite Geodesy: Foundations, Methods, and Application,*Walter

de Gruyter, Berlin, New York, 531pp.

Serpas, J.G. (2003). Local and regional geoid determination from airborne vector gravimetry, *Reports of Department of Civil and Environmental Engineering and Geodetic Science*, **468**, Ohio State University, Columbus.

Serpas, J.G. and C. Jekeli (2005). Local geoid determination from airborne vector gravimetry, *J. Geod.*, **78**, pp.577–587.

Sevilla, M. (1997). A high-resolution gravimetric geoid in the Strait of Gibraltar, *J. Geod.*, **71**, pp. 402-410.

Shih, H.C. (2004). Measurement system of airborne gravity, *MSD theses of Department of Civil Engineering*, National Chiao Tung University, Hsinchu, Taiwan. (in Chinese)

Sideris, M.G.. (1995). On the use of heterogeneous noisy data in spectral field modelling methods, *J. Geod.*, **70**, pp. 2 -12.

Sjoberg, L.E. (2000). Topographic effects by the Stokes-Helmert method of geoid and quasi-geoid determinations, *J. Geod.*, **74**, pp.255-268.

Sjoberg, L.E. (2004). The effect on the geoid of lateral topographic density variation, *J. Geod.*, **78**, pp. 34-39.

Smith, D.A. and D.G. Milbert (1999). The GEOID96 high resolution geoid height model for the United States, *J. Geod.*, **73**, pp. 219-236.

Smith, D.A. (2002). Computing components of the gravity field induced by distant topographic masses and condensed masses over the entire Earth using the 1-D FFT approach, *J. Geod.*, **76**, pp. 150–168.

Schwarz, K.P. and Z. Li (1997). Introduction to airborne gravimetry and its boundary value problems, in "Geodestic Bounday Value Problems in view of the one Centimeter Geoid, F Sanso and R Rummel (eds), *Lecture Notes in Earth Sciences*, **65**, Springer, Berlin. 588 pp.

Thompson, L. and L. LaCoste(1960) Aerial Gravity Measurements, *J. Geophys. Res.*, **65**, pp. 305-322.

Tsuei, G.C. (1995). The investigation of digital geoid model over Taiwan, *PHD Theses of Department of Earth Sciences and Institude of Geophysics,* National Central University, Taiwan. (in Chinese)

Torge, W. (1989). Gravimetry, *de Gruyter*, Berlin.

Torge, W. (1991). Geodesy, *de Gruyter*, Berlin.

Tscherning, C.C. and R.H. Rapp (1974). Closed covariance expressions for gravity anomalies, geoid undulations, and the deflections of the vertical implied by anomaly Degree-variance models, *Reports of the Department of Geodetic Science*, **208**, Ohio State University, Columbus.

Tscherning C.C., A. Radwan, A.A. Tealeb, S.M. Mahmoud, A.E. Mohamed, R. Hassan, E.S. Issawy, and K. Saker (2001). Local geoid determination combining gravity disturbances and GPS/levelling: A case study in the Lake Naser area,

Aswan, Egypt, *J. Geod.*, **75**, pp. 343-348.

Vanicek, P., J. Huang, P. Novak, S.D. Pagiatakis, M. Veronneau, Z. Martinec, and W.E. Featherstone (1999). Determination of the boundary values for the Stokes-Helmert problem, *J. Geod.*, **73**, pp. 180-192.

Verdun, J., E.E. Klingele, R. Bayer, M. Cocard, A. Geiger, and H.G. Kahle (2003). The alpine Swiss-French airborne gravity survey, *Geophys. J. Int.*, **152**, pp. 8-19.

Wessel, P. (1989). Xover: a crossover error detector for track data, *Comput. Geosci.,* **15**, pp. 333–346.

Wessel, P and W.H.F. Smith (1999). The generic mapping tools (GMT), *Technical Reference and Cookbook,* Univ. of Hawaii, USA.

Wei, M and K.P. Schwarz (1998). Flight test results from a strapdown airborne gravity system, *J. Geod.*, **72**, pp.323-332.

Wiener, N. (1949). Extrapolation, interpretation and smoothing of stationary time series, *John Wiley and Sons*, New York.

Yen, HY., YH. Yeh, CH. Lin, GK. Yu, and YB. Tsai (1990). Free-air gravity map of Taiwan and its applications, *Terr. Atmos. Ocean. Sci.*, **1**, pp.143-156.

Yen, HY., YH. Yeh, CH. Lin, KJ. Chen, and YB. Tsai (1995). Gravity survey of Taiwan, *J. Phys. Earth.*, **43**, pp.685-696.

Yu, S.B., H.Y. Chen, and L.C. Kuo (1997). Velocity field of GPS stations in the Taiwan area, *Tectonophysics*, **271**, pp. 41-59.

Zhdanov, M.S. (2002). Geophysical Inverse Theory and Regularization Problems, *Eesevier Science B. V.*, Amsterdam, The Netherlands.

Curriculum Vitae

Position:

Department of Civil Engineering

National Chiao Tung University

1001 Ta Hsueh Road, Hsinchu 300

Taiwan

Phone: +886-3-5712121 ext 54990

Fax: +886-3-5716257

Email: hys@geodesy.cv.nctu.edu.tw

WWW: http://space.cv.nctu.edu.tw
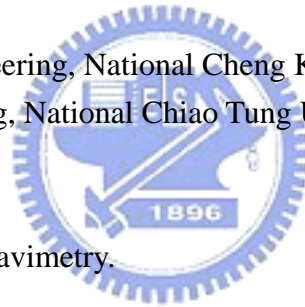
Date of Birth: December 20, 1977.

Place of birth: Tainan city, Taiwan.

Education:

BS, Dept of Surveying Engineering, National Cheng Kung University, June 2000.

MS, Dept of Civil Engineering, National Chiao Tung University, June 2002.

Major field of research:

Physical geodesy, Airborne gravimetry.

Publications:

Refereed journal papers

Hwang, C., C.S. Chen, J.T. Lee, C.G. Wang, L.H. Lee, Y.S. Hsiao, C.S. Cheng, and F.S. Ning (2002). Gravity survey on first-order benchmarks, Cadastre Survey, 21(1), pp.1-27. (in Chinese)

Hwang, C. and Y.S. Hsiao (2003). Orthometric correction from leveling, gravity, density and elevation data: a case study in Taiwan, Journal of Geodesy, 77, pp. 279-291.

Hwang, C., C.G. Wang, and Y.S. Hsiao (2003). Terrain correction computation using Gaussian quadrature: effect of innermost zone, Computers and Geosciences, 29 (10), pp. 1259-1268.

Hwang, C., Y.S. Hsiao, and T.L. Lin (2003). A digital elevation model of Taiwan and accuracy assessment, Cadastre Survey, 22 (2), pp.1-19. (in Chinese)

Hwang, C., Y.S. Hsiao, and H.C. Shih (2006) Data reduction in scalar airborne gravimetry: Theory, computer package and case study in Taiwan, Computers and Geosciences, 32, pp. 1573-1584.

Hwang, C., Y.S. Hsiao, C.C Lu, W.S. Wu, and Y.H. Tseng, (2007). Determination of Height of Northeast Asia's Highest Peak (Mt. Jade) by direct leveling, Survey Review, 39 (303).

Hwang, C., Y.S. Hsiao, H.C. Shih, M. Yang, K.H., Chen, R. Forsberg, and A.V. Olesen (2007b). Geodetic and geophysical results from a Taiwan airborne gravity survey: Data reduction and accuracy assessment, Journal of Geophysical Research, 112(B10), DOI:10.1029/2005JB004220.

Conference papers

Hwang, C., C.G. Wang, Y.S. Hsiao, T.C. Cheng, H.H. Wei, C.W. Lee, H.C. Yu, R. Forsberg, and A.V. Olesen (2004). Absolute gravimetry and airborne gravimetry in Taiwan. Gravity, Geoid and Space Missions – GGSM2004, Porto, Portugal, August 30 – Sept. 3.

Hwang, C., C.G. Wang , Y.S. Hsiao, H.C. Shih, R. Forsberg, and A.V. Olesen (2005). Results of airborne gravity survey in Taiwan, European Geosciences Union, General Assembly 2005, Vienna, Austria, 24 - 29 April.

Hwang, C., Y.S. Hsiao, H.C. Shih, C.G. Wang, R. Forsberg, and A.V. Olesen (2005). Geodetic and geophysical results from a Taiwan airborne gravity survey, Dynamic Planet 2005, Cairns, Australia, 22-26 August.

Hsiao, Y.S., C. Hwang, and H.C. Shih (2006). Geoid modeling results over Taiwan using two different types of altimetry data, Western Pacific Geophysics Meeting, Beijing, China, 24-27 July.